University of Reading

Investigating the moisture transport associated with extratropical cyclones and the mechanisms that lead to precipitation over the UK

A thesis submitted for the degree of Doctor of Philosophy

School of Mathematical, Physical and Computational Sciences

Sophie Cuckow

September 2023

ABSTRACT

Both atmospheric rivers and the warm conveyor belts of extratropical cyclones have been linked to heavy precipitation and flooding in the UK. A low-level cyclone-relative moist airflow called the feeder airstream has been shown to transport moisture from the environment ahead of an intense cyclone to the base of the warm conveyor belt where it rises to form precipitation and enhances the poleward transport of moisture in an atmospheric river.

In this study, the presence of a feeder airstream is investigated using a case study and a climatology of 1000 storms. The likelihood of a feeder airstream occurring, and the strength of the feeder airstream in relation to cyclone intensity, propagation velocity and life-cycle stage is determined. In the case study, a feeder-airstream is identified during the developing stage of the storm. The feeder airstream is also identified in the majority of the cyclones in the climatology. However, the strength of the moisture flux associated with the feeder airstream decreases with a decrease in maximum intensity, propagation velocity and, in the latter stages of the cyclone life-cycle.

To quantify the contribution of synoptic scale and micro-scale processes leading to the precipitation associated with the case study, the proportion of rainfall attributed to cyclone ascent, orographic ascent and the seeder-feeder mechanism is calculated when the extratropical cyclone with a feeder airstream and an atmospheric river passes over the UK. Modifications to the height of the orography and

the accretion and riming micro-physical processes are made in the Met Office Unified Model. It is found that the majority of the precipitation is produced by cyclone ascent and the accretion and riming related to the seeder-feeder mechanism. This suggests that heavy precipitation is formed by a combination of cyclone precipitation and low-level cloud formation associated with the feeder airstream.

DECLARATION

I confirm that this is my own work and the use of all material from other sources has been properly and fully acknowledged.

Signed: Sophie Cuckow

Date: 22 September 2023

ACKNOWLEDGEMENTS

First and foremost I would like express my gratitude towards my supervisors Professor Helen Dacre and Dr Oscar Martínez-Alvarado for their support and patience during my PhD. Without them, I would not have the knowledge and skills that I have today. Secondly, thank you to my monitoring committee, Professor Richard Allan and Professor Danny Feltham for their insightful comments and suggestions. Finally, I would like to thank my friends and family for supporting and believing in me throughout my PhD. I will be eternally grateful for your kind words and encouragement.

CONTENTS

CHAPTER

ONE

INTRODUCTION AND LITERATURE REVIEW

1.1 Extratropical cyclones

An extratropical cyclone is a synoptic scale low pressure frontal system that is found in the mid-latitudes (between approximately 30° N and 60° N in the northern hemisphere). A comma shaped cloud head, a cloud free band, a cold frontal cloud band, and a warm frontal cloud band are common features of these cyclones that can be identified in satellite imagery (Figure 1.1). To understand the cloud structure that is seen in the satellite imagery, a variety of tools and techniques are used to describe the position of the fronts, position of the low pressure centre, the ascent and descent of airflows along the fronts and the path of air-parcels associated with these storms.

1.1.1 Conceptual models and vertical structure

Conceptual models describe the position of the fronts and the low pressure centre associated with the cyclone. The most notable of these models are the Norwegian (Bjerknes, 1919) and Shapiro-Keyser (Shapiro and Keyser, 1990) models. The Norwegian model, developed by Bjerknes (1919), describes a cyclone developing from a stationary front into a frontal wave. Perturbations cause a warm front to move

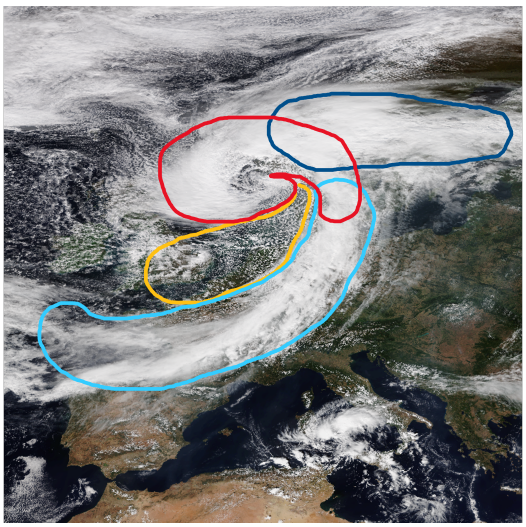

Figure 1.1: A satellite image of storm Bronagh on 21 September 2018, showing the typical cloud structure associated with extratropical cyclones. The red selection shows the cloud head, the light blue the cold frontal cloud band, the dark blue the warm frontal cloud band and the yellow a cloud free band. Adapted from images taken by the VIIRS (Visible Infrared Imaging Radiometer Suite) instrument on the NOAA-20 satellite (NOAA, 2023).

northwards and a cold front to push southwards in a counter-clockwise circulation (in the northern hemisphere) (Figures 1.2 I and II). This motion results in the formation of a warm sector between the cold and warm fronts, which contains warm, moist air, and a cold sector poleward of the warm and cold fronts which contains cooler, dryer air. At the centre of this circulation, there is convergence and ascent which decreases the pressure (shown in Figure 1.2 III by the increasing number of isobars around the low pressure centre L). When the cold front catches up to and overtakes the warm front, an occluded front forms, lifting warm air from the surface (due to the higher density of the cold air) (Figure 1.2 IV). This results in the separation between the warm sector and the low pressure centre, and occurs as the cyclone reaches maximum intensity.

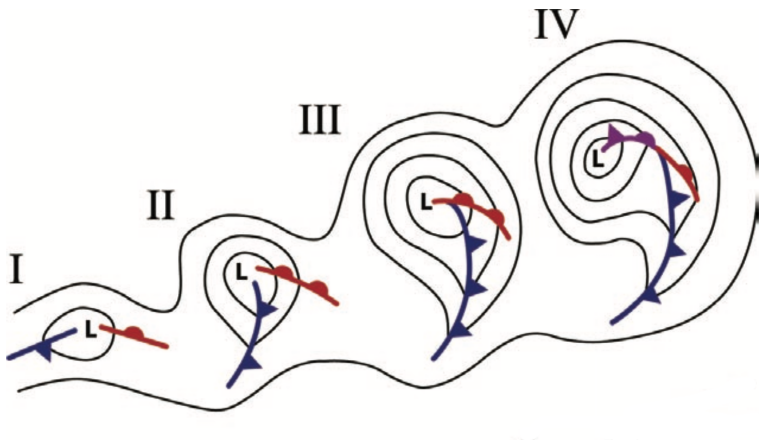

Figure 1.2: The Norwegian conceptual model showing the position of the warm and cold fronts, isobars and occluded front during cyclogenesis. Time increases from left to right so I is the earliest stage in a cyclone's evolution. Adapted from Schultz and Vaughan (2011). © American Meteorological Society. Used with permission.

Instead of an occluded front forming as the cyclone reaches maximum intensity, the Shapiro-Keyser model describes frontal fracture and warm seclusion. Frontal fracture occurs when the warm and cold fronts separate, resulting in the perpendicular motion of the cold front relative to the warm front (Figure 1.3 II). This allows

the warm front to wrap around the cyclone centre to form a bent back warm front and a warm seclusion (Figures 1.3 III and IV) (Shapiro and Keyser, 1990). The warm core of the cyclone is cut off from surrounding colder air. Much like the occlusion process in the Norwegian model, frontal fracture and movement of the cold front acts to separate the warm sector from the low pressure centre (Schultz and Vaughan, 2011).

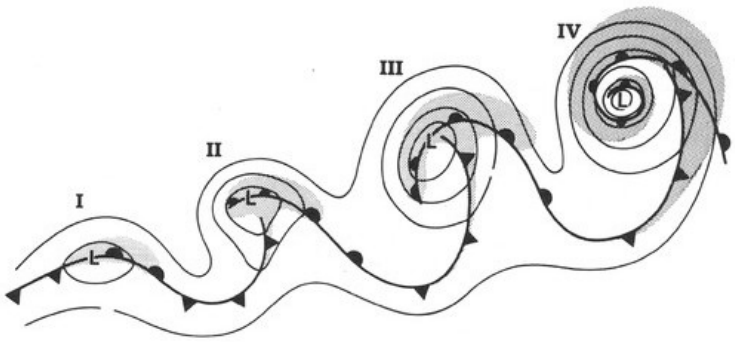

Figure 1.3: The Shapiro-Keyser conceptual model showing the position of the warm and cold fronts, isobars the cloud head and a bent back warm front during cyclogenesis. Time increases from left to right so I is the earliest stage in a cyclone's evolution. Adapted from Shapiro and Keyser (1990). © American Meteorological Society. Used with permission.

Whilst these conceptual models are useful for describing the position of the fronts during a cyclone's life-cycle, they do not describe the upper-level features associated with extratropical cyclones. Cyclones develop as a result of the interaction between upper and lower-level features through a process called mutual intensification (Figure 1.4). When a low pressure centre at the surface is ahead (to the east) of an upper-level trough, the downstream divergence at upper-level deepens the low pressure at the surface, which in turn intensifies the convergence at the surface and thus intensifies the upper-level divergence. Therefore, extratropical cyclones tend to have a westwards tilt in the vertical (Palmén, 1931).

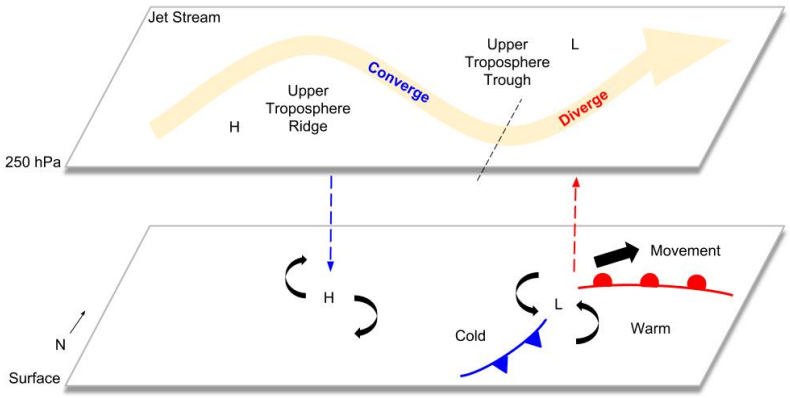

Figure 1.4: Diagram of the mutual intensification of a cyclone and an upper-level trough (including an anticyclone and ridge). A trough, created by the jet stream (yellow arrow on the 250 hPa surface) lies to the west of the surface low (L). The trough axis is shown by the black dashed line on the 250 hPa surface. Ascent is represented by the red dashed arrow, and descent by the blue. Cyclonic and anticyclonic motion (northern hemisphere) are shown by the curved black arrow and the propagation of the cyclone is shown by the straight black arrow (Nugent et al., 2019). (Note: the work of Nugent et al. (2019) is licensed under a Creative Commons Attribution 4.0 International License. Atmospheric Science: A Companion Text for ATMO 200 by the University of Hawai'i at Mānoa Atmospheric Sciences Department.)

1.1.2 Cyclone-relative airflows

Since the 1970's, cyclone-relative airflows on isentropic surfaces have been used to describe the formation of cloud and precipitation by extratropical cyclones in the conveyor belt model (Browning and Harrold, 1970). Isentropic surfaces, or isentropes, are surfaces of constant potential temperature. In regions of constant horizontal temperature, these surfaces are parallel to the ground and the potential temperature increases with height. When the temperature is colder, for example at the poles, these surfaces will remain parallel to the ground but will also be colder.

However, where there is a strong horizontal temperature gradient, for example in the vicinity of a front, the isentropes slope downwards towards warm air. To conserve potential temperature, dry air parcels will ascend and descend along these isentropes. Therefore, isentropic flow describes the ascent and descent (of dry air parcels) along the fronts. However, if a cyclone is moving through the atmosphere, isentropic flow analysis will not describe flows that are travelling rearwards relative to the cyclone propagation because the flows are analysed in an Earth-relative frame of reference. Therefore, to describe these rearward travelling flows, the propagating cyclone is taken as the frame of reference. To make the transition from an Earth-relative framework to a cyclone-relative one, the cyclone propagation velocity is subtracted from the Earth-relative wind fields, resulting in the cyclone-relative wind field. This results in the three-dimensional cyclone-relative airflows called conveyor belts (Carlson, 1980). These are described in Figure 1.5 in relation to the surface fronts and the low pressure centre.

The warm conveyor belt (red arrow in Figure 1.5) is a moist airflow that ascends from the warm sector ahead of the cold front. It ascends to the upper-troposphere where one branch turns cyclonically to form the upper portion of the comma shaped cloud head (Browning, 1971). The cold conveyor belt (blue arrow in Figure 1.5) transports cool, moist air north of the warm front to the west of the low pressure centre. The cold conveyor belt sits below the warm conveyor belt and creates the lower portion of the cloud head and precipitation (Carlson, 1980). The dry intrusion (yellow arrow in Figure 1.5) is a dry airflow that descends behind the cold front bringing dry air from the lower stratosphere and upper troposphere. It assumes a hammer-head shape behind the cold front (not shown in Figure 1.5) as it descends and creates a cloud free band between the cloud head and the cold frontal cloud band (Young et al., 1987).

Cyclone-relative airflows, in particular the warm conveyor belt, can also be char-

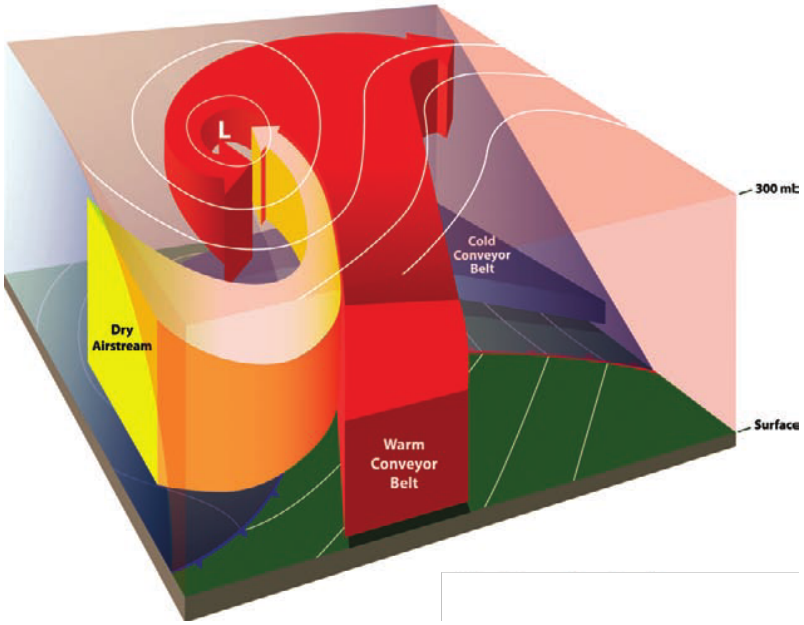

Figure 1.5: A three-dimensional schematic of the warm conveyor belt, cold conveyor belt and the dry airstream (also known as the dry intrusion) in relation to the location of the low pressure centre of an extratropical cyclone and the surface fronts. The extratropical cyclone is propagating towards the top left hand corner of this Figure. The blue line represents the cold front, the red the warm front and the white lines represent isobars. Cold air is shaded blue and warm shaded red (Schultz and Vaughan, 2011). © American Meteorological Society. Used with permission.

acterised using cyclone-relative Lagrangian trajectories. This technique involves tracking air-parcels as they are advected by three-dimensional wind fields through the atmosphere. The trajectories of these air parcels can be clustered depending on their characteristics to identify cyclone-relative airflows. Trajectories with ascent greater than 600 hPa from the lowermost troposphere (for example, if a trajectory is ascends from 1000 hPa, which is in the lower troposphere, to 450 hPa, which is in the upper troposphere) within 2 days is often used to characterise the warm conveyor belt (Wernli, 1997; Martínez-Alvarado et al., 2014; Madonna et al., 2014). Whilst cyclone-relative Lagrangian trajectories and isentropic flow analysis both give insight into the structure of extratropical cyclones, Lagrangian trajectories are

computationally expensive. This is due to the fact that Lagrangian trajectories analyse the path of air parcels over time, whereas isentropic flow analysis captures a snapshot of the field in time. Nevertheless, streamlines along isentropic surfaces will, over a short distance, provide an estimate of the pathways that are followed by air parcels, as described by the Lagrangian trajectories.

1.1.3 Cyclone intensity, propagation velocity and tracking

Due to their structure and evolution, the intensity of a cyclone can be measured using the central mean sea level pressure or using relative vorticity. The deeper the low pressure centre (or the larger the relative vorticity), the more intense the cyclone is. Both relative vorticity and mean sea level pressure can be also used to identify the three stages of an extratropical cyclone's life-cycle (intensification, maximum intensity or decay). A cyclone is developing or deepening when the mean sea level pressure centre is decreasing (or the relative vorticity maximum is increasing). A cyclone is at maximum intensity when either the mean sea level pressure is at its minimum or the relative vorticity is at its maximum. Once the cyclone starts to decay the mean sea level pressure starts to increase again (and the relative vorticity starts to decrease). Mean sea level pressure or relative vorticity can also be used to find the path that a cyclone takes, called a cyclone track. This technique is used in a variety of feature tracking algorithms, where the feature is either the low pressure centre or maximum in relative vorticity (Walker et al., 2020). As the position of the cyclone is known at each time-step, the propagation velocity of the cyclone as it moves through the atmosphere can be found using, for example, a centered difference approach.

1.2 Atmospheric rivers

The atmospheric river conceptual model was first introduced in the 1990's by Newell et al. (1992) and Zhu and Newell (1994). Atmospheric rivers (AR) are long, narrow transient corridors of strong horizontal vapour transport that are typically located ahead of the cold front of an extratropical cyclone and are associated with a pre-cold frontal low-level jet (LLJ) (Ralph et al., 2004; Ralph and Dettinger, 2011; Ralph et al., 2018). The pre-cold frontal low-level associated with extratropical cyclones and atmospheric rivers is typically found in the lower 2–3 km of the atmosphere. It forms as a result of the large temperature gradient (and pressure gradient) across the cold front (AMS, 2023b). Much like the warm conveyor belt, atmospheric rivers also describe moisture transport in the midlatitudes and are characterised using thresholds in total column water vapour (TCWV) or integrated vapour transport (IVT). TCWV (otherwise known as vertically integrated water vapor (IWV) (AMS, 2023a)) is the total amount of water vapour in a vertical column of air. It is calculated using equation 1.1 where q is specific humidity, p is the pressure and g is the acceleration due to gravity.

$$TCWV = -\frac{1}{g}\int q\,dp \tag{1.1}$$

IVT is the vertically integrated water vapor transport and describes the flux of moisture that is advected by the Earth-relative wind field. It is calculated using equation 1.2 where $\vec{V}$ is the Earth-relative wind velocity.

$$IVT = -\frac{1}{g}\int \vec{V}\,q\,dp \tag{1.2}$$

A schematic of an atmospheric river is shown in Figures 1.6 and 1.7. An atmospheric river typically has a centroid (i.e. a maxima) in IVT close to the centre of a cyclone in the cyclone's warm sector. The direction of water vapour transport is parallel to the cold front and towards the warm front (Figure 1.6). The centroid of an atmospheric river coincides with a maximum in a LLJ, therefore, an atmospheric

river can be thought of as a moisture-weighted LLJ (Figure 1.7). Therefore, similarly to a LLJ, atmospheric rivers are also low-level features that are typically 3 km deep. The strength of an atmospheric river is dependent on the amount of moisture available and the strength of the LLJ. Therefore, a filament of high IVT does not necessarily mean that there will also be a filament of high TCWV. This is because TCWV is only dependant on the specific humidity, rather than on the Earth-relative wind speed and specific humidity as described by the IVT (equations 1.1 and 1.2).

As the intensity of an atmospheric river is linked to the intensity of a LLJ, it is also linked to the intensity of a cold front and a cyclone. The stronger that the low-level horizontal temperature gradient is, the stronger the cyclone, front and the stronger the LLJ. This is supported by the work of Guo et al. (2020) who found that an atmospheric river centroid is located in the strong pressure gradient created between a cyclone located polewards and westwards, and an anticyclone located equatorward and eastward. This study also found that cyclones without a paired anticyclone are found not to have an associated atmospheric river. The relationship between atmospheric river and cyclone intensity is further supported by the work of Wang et al. (2022), who found that landfalling atmospheric rivers associated with weaker and less developed cyclones are shorter, thinner and have reduced IVT in comparison to those that develop from well-developed cyclones.

Atmospheric rivers are a global phenomena that have a wide variety of impacts. They can lead to heavy flooding when they are landfalling (e.g. Lavers et al. (2011)), can influence extreme ablation and snowfall events (e.g. Little et al. (2019)), can induce surface melting of ice sheets resulting in the loss of mass (Oltmanns et al., 2019; Mattingly et al., 2018; Wille et al., 2024) and can effect changes in terrestrial water storage (Adusumilli et al., 2019). The impacts of heavy rainfall and flooding relating to atmospheric rivers and extratropical cyclones are discussed in more detail in section 1.4.1.

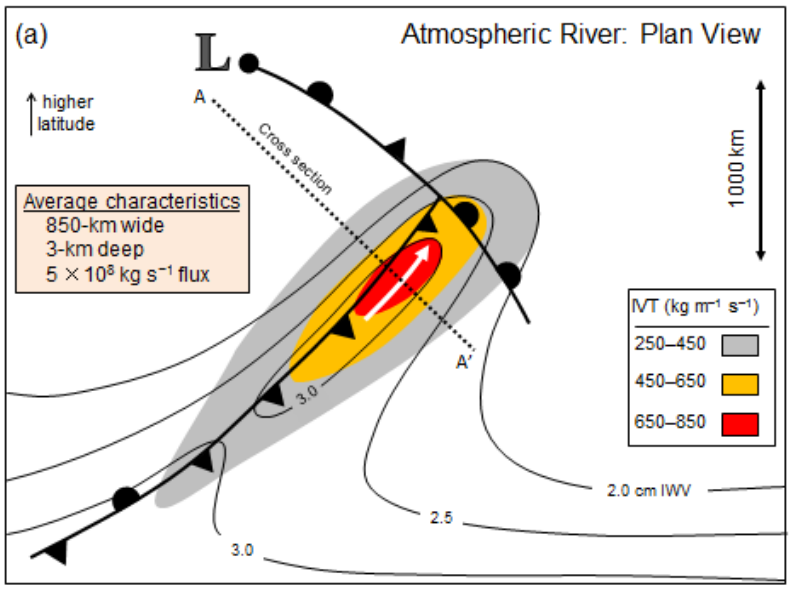

Figure 1.6: A plan view of an atmospheric river in relation to the fronts and low pressure centre of an extratropical cyclone (L). The IVT is shown by the filled contours and uses a lateral boundary condition of 250 kg m^{-1} s^{-1}. The IWV is shown by the black contours. The dotted line depicts the location of the cross section shown in Figure 1.7. This Figure is taken from Ralph et al. (2017) and shown in the AMS glossary for atmospheric rivers (AMS, 2023a). © American Meteorological Society. Used with permission.

A plethora of atmospheric river detection algorithms are used to identify atmospheric rivers. These algorithms can use feature tracking (Reid et al., 2022), use absolute (Ralph et al., 2004) or relative thresholds (Lavers et al., 2012; Guan and Waliser, 2015, 2019) for atmospheric moisture, winds, TCWV and IVT, use geometric thresholds such as width and length, and can use temporal thresholds. These algorithms can also be suitable for use either globally or in specific regions (Shields et al., 2018; Collow et al., 2022). One of the more commonly used thresholds, is an absolute threshold of 250 kg m^{-1} s^{-1} in IVT (Moore et al., 2012; Rutz et al., 2014; Ralph et al., 2017; Rutz et al., 2019). However, this threshold may not be suitable for use in global studies (Reid et al., 2020; Guan et al., 2023). Atmospheric rivers

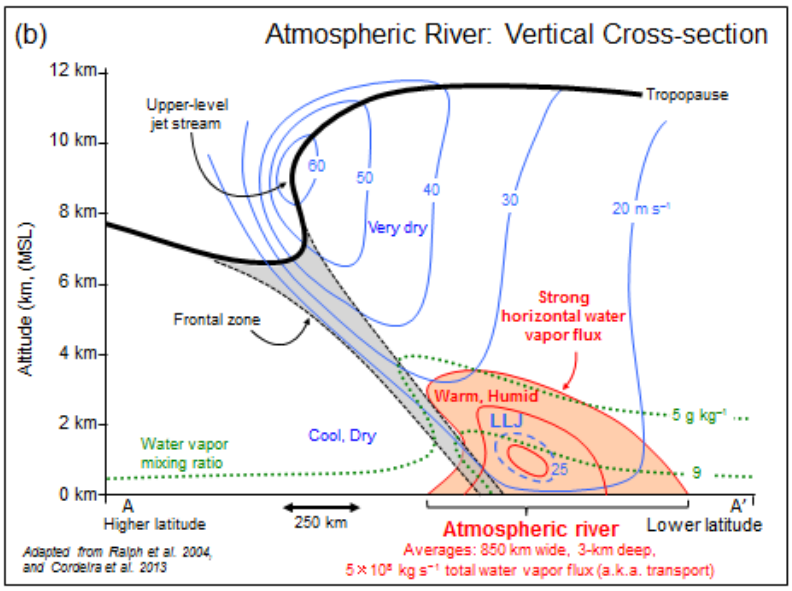

Figure 1.7: A vertical cross section of an atmospheric river, front and tropopause. The altitude above mean sea level is on the y-axis and the distance between A and A' (shown in Figure 1.6) on the x-axis. The atmospheric river is shown by the red shading, the Earth-relative wind speed by the solid blue lines, the cross-section-normal isotachs by the dashed blue lines, the water vapor mixing ratio by the green dotted lines, the frontal zone by the grey shading and the tropopause by the thick black line. The atmospheric river is characterised by strong horizontal vapour flux related to a low-level jet (LLJ). This Figure is taken from Ralph et al. (2017) and shown in the AMS glossary for atmospheric rivers (AMS, 2023a). © American Meteorological Society. Used with permission.

can also be described using Lagrangian trajectories in an Earth-relative framework (Pérez-Muñuzuri et al., 2018; Sodemann et al., 2020).

1.3 Linking the direction of moisture transport in atmospheric rivers and extratropical cyclones

Even though atmospheric rivers and warm conveyor belts both describe moisture transport at mid-latitudes, there is often a debate in the literature about the di-

rection that moisture is transported to the base of the warm conveyor belt (where it rises to form precipitation). This arises from the fact atmospheric rivers and cyclone-relative airflows, such as the warm conveyor belt, are identified using different frameworks (Earth-relative and cyclone-relative) regardless of whether Eulerian or Lagrangian fields are used.

As we live in an Earth-relative framework, the atmospheric river conceptual model provides a useful tool to help understand the impacts of low-level moisture transport in the atmosphere. However, in this framework, the direction of moisture transport (IVT) suggests that moisture is transported long distances along the cold front by an atmospheric river to the base of a warm conveyor belt. This can not be the case if the cyclone is propagating faster than the moisture transport in the atmospheric river. Cyclone's tend to propagate quicker during their developing stages (Hoskins and Hodges, 2002), therefore, it is more likely that a cyclone is propagating faster than the moisture transport in an atmospheric river during this time. Furthermore, cyclones linked to extreme precipitation and winds have been shown to have a larger intensity and a faster mean speed than those that are not (Owen et al., 2021). This suggests that more intense cyclones tend to have a larger propagation velocity than weaker cyclones. Therefore, intense cyclones are also more likely to be travelling faster than the moisture transport in an atmospheric river than weak cyclones.

It has been shown (in the ERICA IOP 4 case study) that evaporation in the cold sector of a preceding cyclone and in the cyclone–anticyclone interaction zone ahead of a preceding cyclones are key for the formation of precipitation during a cyclone's intensification phase. This moisture (moisture in the pre-cyclone environment) can also lead to the rapid intensification of a cyclone via latent head release in a cyclones' warm conveyor belt (e.g. Reed et al. (1992), Ludwig et al. (2014)). Therefore, it is important that the dynamical processes behind moisture transport in extratropical

cyclones and atmospheric rivers is investigated further so that they are fully understood. The knowledge gained from doing so can be used to further understand the resulting impacts and how these could change as the climate changes. This is particularly important as the intensity of rainfall associated with extratropical cyclones and the intensity of atmospheric river events are expected to increase as the climate changes and there is an increase in atmospheric moisture (Allan et al., 2020).

To understand the direction of moisture transport in extratropical cyclones and atmospheric rivers, Dacre et al. (2015) and Dacre et al. (2019) analysed a climatology of 200 intense winter extratropical cyclones in a cyclone-relative framework. These storms had a maximum intensity in the north Atlantic (70 to 10°W, 30 to 90°N) and occurred between 1989 to 2009. In the study of Dacre et al. (2015), the water vapour budget, the local mass convergence and advection of moisture gradient terms associated with each cyclone was calculated. It was found that the band of high TCWV associated with atmospheric rivers is formed as a result of the motion of the cold front relative to the cyclone. As the cold front moves through the atmosphere, there is moisture flux convergence ahead of the front and therefore, it sweeps up moisture as it moves. This is supported by Sodemann and Stohl (2013) who found that the formation and maintenance of high TCWV at the leading edge of atmospheric rivers is modulated by individual cyclones through moisture flux convergence ahead of their cold fronts. Therefore, moisture in the pre-cyclone environment is not only important in the production of precipitation and the intensification of the cyclone, it is also related to the formation and maintenance of the atmospheric river.

To further investigate the moisture flux convergence ahead of a cold front and to directly link atmospheric rivers and the warm conveyor belt, Dacre et al. (2019) analysed the airflows of the 200-cyclone climatology in a cyclone-relative framework. It was found that a low-level airflow called the feeder airstream (Figure 1.8) is responsible for supplying moisture to the base of the warm conveyor belt and the

enhancement of the poleward transport of moisture through moisture flux convergence. This airstream travels rearwards relative to the cyclone propagation and slows down as it approaches the cold front resulting in the convergence of moisture. It then splits into two branches, one which accelerates towards the cyclone centre along the cold front, feeding moisture to the base of the warm conveyor belt where it rises to form cyclone precipitation. The other branch also runs parallel to the cold front but decelerates relative to the cyclone propagation. The moisture in this branch is left behind by the cyclone as it propagates and therefore, marks the track of the cyclone. The feeder airstream splits an atmospheric river into two regions. The active region which feeds moisture to the warm conveyor belt, and the passive region which is left behind by the cyclone. The presence of a feeder airstream suggests that moisture is transported to the base of the warm conveyor belt from the environment ahead of the cyclone.

Even though the feeder airstream itself is a relatively new concept, references to a rearward travelling cyclone-relative flow and moisture flux convergence ahead of the cold front have been made throughout literature dating back to the 1970's. Houze et al. (1976), Hoskins and West (1979), Carlson (1980), and Mcbean and Stewart (1991) found that the warm conveyor belt originates to the east of the cyclone centre. Boutle et al. (2011), using the unified model in an idealised mode, found that moisture was transported to the base of the warm conveyor belt from the boundary layer ahead of the cyclone centre.

More recently, a study into the the moisture sources of precipitation falling within 500 km from the cyclone center has been investigated by Papritz et al. (2021). This study analysed 676 deep North Atlantic cyclones occurring in the extended winter period (October to March) from 1979 – 2018. It was found that a flow from the north east, consistent with the feeder airstream, transports moisture into the warm sector of the cyclones during their intensification stage. This occurs until 12 hours

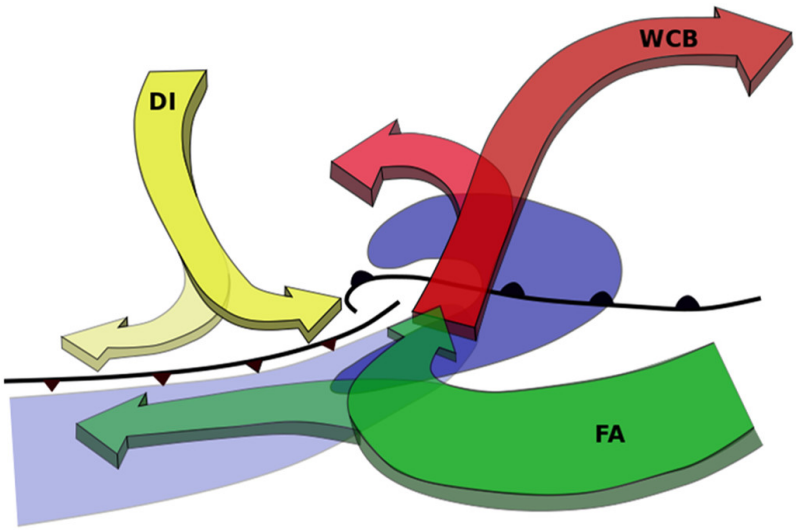

Figure 1.8: Cyclone-relative airflows within an extratropical cyclone. The warm conveyor belt (WCB, red), dry intrusion (DI, yellow) and feeder airstream (FA, green) are depicted by the coloured arrows. The surface fronts are shown in black, high integrated vapour transport (light blue shading) and the precipitation associated with the cyclone (dark blue shading) (Dacre et al., 2019). © American Meteorological Society. Used with permission.

prior to maximum intensity. At this time, the cyclone propagation velocity becomes much weaker and the dominant moisture source becomes the cyclone's own cold sector.

The studies of Dacre et al. (2019) and Papritz et al. (2021) both reach similar conclusions regarding the presence of the feeder airstream despite using different methodologies (cyclone-relative isentropic analysis and cyclone-relative Lagrangian trajectories). However, these studies only focus on intense North Atlantic extratropical cyclones. Therefore, more work is needed to understand the presence of the feeder airstream in weaker cyclones that occur in different geographic locations.

1.3.1 The presence of the feeder airstream in extratropical cyclones

To advance our understanding of the feeder airstream and the direction of moisture transport in extratropical cyclones, this thesis builds upon the work of Dacre et al. (2019) and Papritz et al. (2021). Instead of focusing on intense North Atlantic extratropical cyclones, as done in Dacre et al. (2019) and Papritz et al. (2021), this thesis uses a plethora of cyclones with varying intensities that occur anywhere over the midlatitude northern hemisphere. This is done using cyclone-relative isentropic analysis to allow a large number of cyclones to be analysed.

More specifically, this thesis investigates the likelihood of an extratropical cyclone having a feeder airstream and its dependence on the intensity, propagation velocity and the life-cycle of the storm. It is hypothesised that there is a link between the presence of the feeder airstream (i.e. the direction of moisture transport in an atmospheric river) and the intensity, propagation velocity and the evolution of the associated cyclone. If the cyclone is moving quicker than the flow in an atmospheric river, then moisture flux convergence via the feeder airstream could play an important role in the formation of precipitation via the warm conveyor belt. However, if the cyclone is propagating slower than the flow in an atmospheric river, moisture that is transported long distances along an atmospheric river could play more of a role.

To investigate the presence of the feeder airstream in extratropical cyclones, an identification algorithm is developed using cyclone-relative isentropic analysis and nonlinear systems theory. This algorithm identifies regions associated with the saddle points created by the feeder airstream and the dry intrusion in the cyclone-relative moisture flux field at the cold front. This is done using a case study, storm Bronagh, and is introduced in chapter 2. The direction of moisture transport throughout this storm's evolution is also discussed in this chapter.

In chapter 3, the presence of the feeder airstream and the link to cyclone in-

tensity, propagation velocity and life-cycle is investigated using composite data and the identification algorithm. The investigation is carried out using 1000 randomly sampled storms occurring from 1979 to 2019 and by creating data-sets of cyclones with descending intensity or propagation velocity. By doing so, the feeder airstream is investigated in a plethora of different extratropical cyclones rather than just in intense north Atlantic ones as done in Dacre et al. (2019) and Papritz et al. (2021).

1.4 Linking the synoptic scale and micro-scale mechanisms that lead to heavy precipitation in the UK

1.4.1 The synoptic scale and heavy precipitation

Extratropical cyclones contribute to over 50 % of precipitation in the northern hemisphere (Hawcroft et al., 2012) and contribute to a high percentage of precipitation extremes globally (Pfahl and Wernli, 2012). Warm conveyor belts specifically are relevant to extreme precipitation in many parts of the extratropics (Pfahl et al., 2014). Landfalling atmospheric rivers that coincide with orography can also produce a large amount of precipitation (Gimeno-Sotelo and Gimeno, 2023), particularly along exposed mountain ranges located along west coasts. This link between atmospheric rivers and orographic precipitation has been shown in many studies that focus on the west coast of North America (Ralph et al., 2004, 2006; Neiman et al., 2011; Rutz et al., 2014; Lamjiri et al., 2017), west coasts in Europe (Lavers et al., 2011, 2013; Allan et al., 2016; Champion et al., 2015; Ramos et al., 2015; Michel et al., 2021) and the west coast of of New Zealand (Kingston et al., 2016; Reid et al., 2021). Whilst these studies discuss the link between extratropical cyclones, atmospheric rivers and orographic rainfall (precipitation formed by the influence of orography), they do not ascertain the link between the synoptic scale flows and the micro-scale mechanisms that lead to precipitation.

1.4.2 The micro-scale production of orographic rainfall

The simplest form of orographic precipitation is that formed by orographic ascent. Orographic ascent is the forced lifting of air over topography. If this air contains moisture, orographic ascent can lead to the saturation of air parcels with water vapour, condensation and in some cases, precipitation. This process alone is unlikely to produce large amounts of precipitation over the UK due to the moderate size of the hills which do not have a wide enough horizontal extent. The cloud droplets are unable to grow large enough in the short amount of time it takes the air-parcels to cross these hills (Dore et al., 1992). This suggests that there is another mechanism that leads to the formation of heavy precipitation in the UK. Even though orographic ascent alone might not be enough to produce heavy rainfall in the UK, it can result in the enhancement of precipitation falling from preexisting storms (Browning et al., 1974; Lean and Browning, 2013). This enhancement of precipitation typically occurs via two mechanisms: via the seeder-feeder mechanism or via the release of potential instability through convection.

The seeder-feeder mechanism is the primary enhancer of precipitation in the UK and typically occurs when the warm sector of an extratropical cyclone coincides with orography (Bader and Roach, 1977; Browning and Mason, 1980). Rainfall from an upper-level seeder cloud (cloud produced by the cyclone) falls through a lower-level feeder cloud (Figure 1.9). Droplets from the seeder cloud collide and coalesce with cloud droplets in the feeder cloud via a process called accretion. The lower-level feeder cloud is formed via the orographic ascent (orographic uplift in Figure 1.9) of a low-level moist airflow (Hill et al., 1981), such as an atmospheric river. This is often called cap cloud or orographic cloud. The enhancement of rainfall often lies on the windward side (upstream) of the mountain leaving a rain shadow (area of no rain) on the lee-side (downstream). This is because moisture in the air is either precipitated or 'squeezed' out resulting in dry air or, because descending air on the

leeward side warms and dries, suppressing precipitation (AMS, 2023c).

The degree of rainfall enhancement within the feeder cloud depends largely on the strength of the low-level winds, the humidity and temperature of the low-level air and, the intensity of precipitation falling from the seeder cloud (Hill et al., 1981; Smith et al., 2010; Lean and Browning, 2013). It was found by Hill et al. (1981) that the largest enhancement of rainfall coincides with high winds and relative humidity below 2 km and that 80 percent of the enhancement occurs in the lowest 1.5 km over the hills. Furthermore, moist air masses below 1 km have been shown to be important in the production of orographic precipitation over the western US and UK (Smith et al., 2010; Neiman et al., 2011). This low-level moist flow is consistent with an atmospheric river which typically lies below 3 km. The low-level winds can also be responsible for the horizontal drift of raindrops (up to 8 km) as they fall through the feeder cloud (Lean and Browning, 2013).

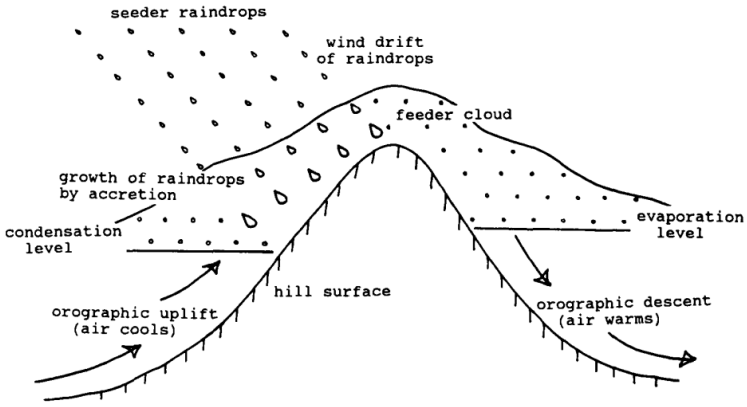

Figure 1.9: A schematic of the seeder-feeder mechanism as shown in Dore et al. (1992). Reprinted from Atmospheric Environment. Part A. General Topics, Volume 26 / Issue 3, A.J. Dore, T.W. Choularton, R. Brown, R.M. Blackall, Orographic rainfall enhancement in the mountains of the Lake District and Snowdonia, Pages 357-371., Copyright (1992), with permission from Elsevier.

Whilst the schematic shown in Figure 1.9 is a useful tool for visualising the processes that occur during the enhancement of rainfall, it is important to note

that this is a simplistic version of reality. In reality, the seeder and feeder cloud may not be separate and could overlap vertically. The seeded rainfall can also be enhanced via convection triggered by orographic ascent depending on the stability of the atmospheric and the strength of the flow over the orography (Browning et al., 1974; Smith, 1979) (however, in the UK such convection is weak in most orographic situations (Lean and Browning, 2013)). Furthermore, if the melting level is low, ice particles falling from above the melting level can grow by colliding with cloud droplets via a process called riming (Bader and Roach, 1977). Accretion and riming can also happen independently of low-level orographic cloud (Browning et al., 1974).

1.4.3 Linking synoptic scale and micro-scale mechanisms

There are many studies that connect atmospheric rivers, extratropical cyclones or the seeder-feeder mechanism to heavy rainfall (e.g. Ralph et al. (2004); Lavers et al. (2011); Pfahl and Wernli (2012); Lean and Browning (2013)). However, there are much fewer studies that look at both the synoptic scale flows of atmospheric rivers and extratropical cyclones (including the feeder airstream), and the micro-scale mechanisms (such as the seeder-feeder mechanism) in relation to the production of heavy precipitation. Only one study (Kropač et al., 2021) has made the connection between atmospheric rivers, extratropical cyclones and the seeder-feeder mechanism directly (to the authors knowledge). In this study, it was found that heavy precipitation was triggered by the passage of an atmospheric river and an extratropical cyclone over the Southern Alps of New Zealand as a result of the seeder-feeder mechanism.

Therefore, this thesis also aims to quantify the relative contributions of the synoptic scale mechanisms and the micro-scale mechanisms that lead to the production of precipitation in the UK. By modifying the orography and the micro-scale processes in the Met office unified model (MetUM), the proportion of the observed

rainfall that is attributed to cyclone related precipitation, the forced ascent of air and the seeder-feeder mechanism is calculated when storm Bronagh (and associated atmospheric river) passes over the UK. If the majority of the precipitation is formed via cyclone ascent and the seeder-feeder mechanism, this indicates the formation of precipitation is due to a combination of cyclone precipitation and the low-level cloud formed by orographic ascent of moisture in an atmospheric river. This work is presented in chapter 4.

1.5 Research objectives and thesis structure

To understand the direction of moisture transport to the base of an extratropical cyclone's warm conveyor belt and to understand the link between synoptic scale flows (for example, an atmospheric river) and micro-scale mechanisms (such as the seeder-feeder mechanism) in the production of heavy orographic rainfall, three research objectives are addressed in this thesis. These are discussed in the following three chapters and are as follows.

1. Can the feeder airstream be objectively identified using an identification algorithm in a case study, storm Bronagh?

2. Which midlatitude northern hemisphere cyclones are more likely to have a feeder airstream and thus transport moisture to the warm conveyor belt from the environment the cyclone is propagating into? Does the likelihood of a feeder airstream occurring depend on the intensity, propagation velocity or the life-cyclone stage of the cyclone?

3. What proportion of the rainfall associated with the aforementioned case study is produced by the cyclone, the forced ascent of air over orography or via the seeder-feeder mechanism when the case study passes over the UK?

In chapter 2, the case study storm Bronagh is introduced, the development of

the identification algorithm using this case study is discussed and the direction of moisture transport throughout the storm's evolution is analysed. In chapter 3, the investigation into the direction of moisture transport throughout a storm's evolution is expanded to encompass extended winter northern hemisphere cyclones rather than a single case study. The presence of the feeder airstream, and therefore direction of moisture transport, and it's link to the intensity, propagation velocity and the life-cycle stage of a cyclone is investigated. Composite fields of intense, moderately intense, moderately weak and weak storms are investigated to see whether the feeder airstream can be seen in composite fields. This is repeated for fast moving, moderately fast moving, moderately slow moving and slow moving storms. As the compositing technique requires taking and average over the available fields, it is difficult to ascertain how likely a feeder airstream is to occur in the composite data-sets. To overcome this, the identification algorithm is applied to each storm. Using these results, the likelihood of a feeder airstream occurring in cyclones with different intensities and propagation velocities at different stages of their life-cycle can be inferred.

In chapter 4, the contributions of the synoptic scale mechanisms and micro-scale processes that led to the production of precipitation when storm Bronagh passed over the UK is quantified. Three experiments are used to calculate the proportion of the observed rainfall that is attributed to cyclone related precipitation, the forced ascent of air and the seeder-feeder mechanism. To focus on the mechanisms that lead to heavy orographic precipitation, the accumulated rainfall over an area of high topography in Wales is investigated. In the final chapter of this thesis (chapter 5), the results, conclusions and future research questions relating to these research objectives are discussed.

CHAPTER

TWO

MOISTURE TRANSPORT IN A CASE STUDY: STORM BRONAGH

In this chapter, the direction of moisture transport in a case study, storm Bronagh is investigated. This chapter is an adapted form of the article, Cuckow et al. (2022). For this paper, I conducted the data analysis, helped to write the first draft of the manuscript and implemented the contributions of the external examiner under peer review up to final publication.

2.1 Abstract

Analysis of moist airflows associated with a case study, storm Bronagh, is conducted to determine whether moisture contributing to observed precipitation near the cyclone centre is transported from the subtropics or local environment. Reanalysis data is used to identify the warm conveyor belt and dry intrusion, and an algorithm is developed to identify the presence of the feeder airstream during the storm's evolution. We conclude that during the intensification stage, moisture is transported by the feeder airstream from the local environment into which Bronagh is propagating and not from the reservoir of moist air in the subtropics.

2.2 Introduction

The precipitation associated with extratropical cyclones can lead to flooding in the UK. Furthermore, the intensity of cyclone precipitation and associated flooding is expected to increase in the future due to climate change (Allan and Soden, 2008). Therefore, it is important that we understand the mechanisms by which extratropical cyclones generate precipitation so that we can accurately forecast flood events and mitigate risk. Previous studies have shown that a cyclone-relative airflow, known as a warm conveyor belt, can generate precipitation extremes (Pfahl and Wernli, 2012) and additional research has found that features known as atmospheric rivers are associated with precipitation extremes in the UK (Lavers et al., 2011, 2012).

Since the 1970's, the structure and evolution of cloud and precipitation features associated with extratropical cyclones have been described using the conveyor belt model. The conveyor belt model analyses Eulerian wind fields on vertically sloping isentropic surfaces in a cyclone-relative framework (Browning and Harrold, 1970). In regions of weak horizontal temperature gradient, isentropic surfaces are approximately horizontal, and potential temperature increases with height. However, in regions with sharp horizontal temperature gradients isentropic surfaces slope in the vertical. Therefore, in the vicinity of fronts, poleward moving dry air parcels will ascend along sloping isentropic surfaces in order to conserve their potential temperature. Conversely, equatorward moving dry air parcels will descend down sloping isentropic surfaces in order to conserve their potential temperature. This results in three-dimensional airflows associated with fronts (Carlson, 1980). Poleward moving airflows transport moist air from the surface to the upper-troposphere resulting in cloud and precipitation formation. Equatorward moving airflows transport dry air from the upper-troposphere to the lower-troposphere, resulting in cloud free regions. However, isentropic flow alone does not explain the development of some cyclone cloud features which move rearwards relative to the motion of the moving

cyclone. An example is the cloud head which emerges from beneath the frontal cloud band and wraps cyclonically around the cyclone centre as the cyclone develops. In order to explain what is seen in the satellite imagery, the moving cyclone must be taken as the frame of reference. By subtracting the cyclone motion vector from the wind vectors, the transition to a cyclone-relative framework is made and the cyclone-relative airflows, called conveyor belts, which form the conveyor belt model can be identified.

Figure 1.8 describes three cyclone-relative airflows in relation to the surface fronts, precipitation and moisture flux features (Dacre et al., 2015). The poleward moving warm conveyor belt (red arrow labelled WCB in Figure 1.8) is a moist cyclone-relative airflow that ascends from the top of the boundary layer ahead of the cold front along a relatively warm isentropic surface, leading to cloud and precipitation formation (Browning, 1971). Typically, during the developing stages of cyclone evolution, the WCB ascends to the upper-troposphere where it turns anticyclonically to form a cirrus shield. During the mature stage of cyclone evolution, a lower branch of the WCB can turn cyclonically to form the upper portion of the comma shaped cloud head. The dry intrusion (yellow arrow labelled DI in Figure 1.8) is an equatorward moving cyclone-relative airflow that descends behind the cold front bringing dry air from the lower stratosphere and upper troposphere. It assumes a hammer-head shape behind the cold front as it descends and creates a cloud free band between the cloud head and the cold frontal cloud band (Young et al., 1987). The feeder airstream (green arrow labelled FA in Figure 1.8) is a moist cyclone airflow within the boundary layer of the cyclone's warm sector, where horizontal temperature gradients are weak (Dacre et al., 2019). This cyclone airflow transports moist air horizontally towards the cyclone's cold front where moisture flux convergence leads to the formation of a filament of high total column water vapour. Some of this moisture is transported towards the centre of the cyclone, where it supplies

moisture to the base of the warm conveyor belt. The remainder of the filament is transported away from the cyclone centre as it moves polewards.

Cyclone-relative airflows can also be described using Lagrangian trajectories. This technique involves following the path of parcels of air as they are transported in the atmosphere by the 3-dimensional wind fields. These trajectories can be clustered into airflows, such as the warm conveyor belt, based on set criteria (Wernli and Davies, 1997; Wernli, 1997; Hart et al., 2015). The analysis of winds on isentropic surfaces, or isentropic flow analysis, is an alternative technique analogous to Lagrangian trajectories. Both provide an indication of the structure of airstreams within the cyclone (Browning and Roberts, 1994). However, isentropic flow analysis yields a snapshot of the field in time. Therefore, an estimate of pathways that are followed by air parcels for a short period of time (in the order of a few hours) is provided. To compare results from studies that calculate trajectories to those performing isentropic flow analysis, both must be computed in the same frame of reference.

An alternative model for describing moisture transport in the extratropics was developed in the 1990's and is known as the atmospheric river model (Newell et al., 1992). Atmospheric rivers are long, narrow and transient corridors of strong horizontal water vapour transport (Ralph et al., 2018). They are identified by calculating the Eulerian vertically integrated moisture flux from the surface to the upper-troposphere (known as vertically Integrated Vapour Transport, IVT). Typically, they are bounded by a fixed moisture flux threshold of 250 kg $m^{-1}s^{-1}$ although statistically defined thresholds have also been used (Shields et al., 2018). Since they are defined using a vertically integrated measure, atmospheric rivers are two-dimensional features. Atmospheric rivers have also been described using Lagrangian trajectories in an Earth-relative framework, for example in Pérez-Muñuzuri et al. (2018) and Sodemann et al. (2020).

The ascent necessary to convert water vapour within an atmospheric river into precipitation is typically invoked via the atmospheric river's co-location with orography leading to forced ascent, or via co-location with cyclone warm conveyor belts leading to the moist isentropic ascent described above (as shown in the light blue shading in Figure 1.8). However, atmospheric rivers are identified in an Earth-relative framework whereas, the conveyor belt studies of Browning and Harrold (1970) and others are performed relative to moving cyclones. Therefore, it is difficult to directly relate atmospheric river flows to cyclone-relative warm conveyor belt airstreams and thus determine whether the identified moisture flux results in transport towards or away from the moving warm conveyor belt at any given time. Despite these drawbacks, the atmospheric river model has proved to be a popular tool for examining the meridional transport of moisture from the subtropics to the extratropics (Gimeno et al., 2014). The diagnostic to identify atmospheric rivers, IVT, does not require cyclone tracking and is calculated using widely available pressure level model output so is simpler to implement than cyclone-relative isentropic flow.

Significant statistical relationships have been found between atmospheric river strength and flooding events which suggests that the atmospheric river model is a useful indicator of heavy precipitation. Dacre et al. (2019) investigated the relationship between IVT and cyclone precipitation in a climatology of 200 strong North Atlantic cyclones. They found that the moisture supplied to the base of the warm conveyor belt is not transported from where the atmospheric river feature met the reservoir of moist air in the subtropics (hereafter termed non-local moisture), but instead was transported from the local environment through which the cyclone was travelling. Since cyclones typically travel with a velocity similar to the wind velocity at 700 hPa (the steering level), they are moving faster than the moist boundary layer air through which they are travelling. As a result, the cold front sweeps up

boundary layer moisture and the resulting moisture flux convergence creates a filament of high moisture content. The feeder airstream (green arrow in Figure 1.8) partitions this filament of moisture into a branch that accelerates towards the base of the warm conveyor belt and a branch that decelerates relative to the cyclone motion, and hence is 'left behind' by the poleward moving cyclone. High IVT is typically identified in both the accelerating and decelerating branches of the feeder airstream. Thus moisture at the leading edge (within a few hundred kilometres) of an atmospheric river can provide moisture to the warm conveyor belt, but moisture along the main body of the atmospheric river, which can extend several thousands of kilometres, does not. Dacre et al. (2019) conclude that while high IVT is statistically related to cyclone precipitation, it is not correct to infer causation and interpret the correlation as atmospheric rivers transporting moisture from the sub-tropics to the centre of a cyclone.

This conclusion is further supported by Papritz et al. (2021) who performed Lagrangian trajectory analysis in a cyclone-relative framework. Consistent with the cyclone-relative isentropic flow analysis of Dacre et al. (2019), they showed that moisture uptakes are linked to the cyclone's warm conveyor belt via the feeder airstream, a northeasterly cyclone-relative flow that arises due to the cyclone propagation exceeding the advection by the low-level background flow. Additionally, these results are supported by the ERICA IOP4 case study, which shows the importance of moisture in the pre-cyclone environment in the production of precipitation. These studies highlight the importance of understanding the direction of moisture transport in extratropical cyclones and atmospheric rivers. Understanding this transport would give further insight into the resulting impacts (for example, heavy precipitation and flooding) and how the risk associated with them might be mitigated. This is particularly important for predicting how these features change as the climate changes.

The study by Dacre et al. (2019) is based on composites of 200 cyclones. Cyclone compositing is a powerful method which emphasises features that are common to the cyclones while de-emphasising features that are not. However, it is possible that the composite fields do not represent the airflows in the individual cyclones that contribute to the composite. Therefore, the aim of this paper is to objectively identify the feeder airstream in a case study, storm Bronagh. To do so, we develop an identification diagnostic that detects the saddle point[1] created by the feeder airstream and dry intrusion using cyclone-relative isentropic flow. This analysis is performed at each stage in storm Bronagh's evolution to ascertain where moisture is transported from at different stages in the storm's development.

2.3 Dataset and cyclone tracking algorithm

This study uses the ERA5 atmospheric reanalysis dataset (Hersbach et al., 2020) which has a spatial resolution of approximately 31 km. At the surface and on isobaric surfaces, the data is interpolated onto a longitude – latitude grid with 0.25° resolution, and on isentropic surfaces, the data is interpolated on a grid with 1° spatial resolution. This resolution is sufficient given that this study is focused on large scale circulation. 3-hourly temporal resolution is used to determine the moisture flux on pressure and isentropic surfaces.

Several single-level reanalysis fields are also analysed. Total column water vapour (TCWV, kg m^{-2}) is the total amount of water vapour in a column extending from the surface of the Earth to the top of the atmosphere. The vertical integral of eastward and northward water vapour fluxes (kg m^{-1} s^{-1}) represent the horizontal rate of flow of water vapour, in the eastward/northward direction, per metre across the flow, for a column of air extending from the surface of the Earth to the top

[1] a point at which a function of two variables has partial derivatives equal to zero but at which the function has neither a maximum nor a minimum value (Collins English Dictionary, 2005)

of the atmosphere. Positive values indicate a flux from west to east or south to north respectively. The vertical integral of eastward and northward vapour fluxes are the vector components of vertically integrated moisture flux (IVT), which is used to identify atmospheric rivers using a threshold of 250 kg $m^{-1}s^{-1}$ (see e.g., Shields et al., 2018, and references therein). A threshold of 250 kg $m^{-1}s^{-1}$ has been shown to be unsuitable for use in global studies Reid et al. (2020). However, as this study focuses on an isolated case study in the midlatitudes and only requires the location of an atmospheric river, it is deemed suitable.

The track of storm Bronagh in the ERA5 dataset is identified using the tracking algorithm of Hodges (1995). The track of storm Bronagh is identified using 3-hourly 850 hPa relative vorticity, truncated to T42 resolution to emphasize the synoptic scales. The 850 hPa relative vorticity features are filtered to remove stationary or short-lived features that are not associated with extratropical cyclones. The track is used to find the minimum pressure at every time-step by searching for the minimum mean sea level pressure in a 500-km radius around the relative vorticity maximum. The track positions at 3-hourly intervals are also used to compute the cyclone's propagation velocity using a centred finite difference approximation.

2.4 Storm Bronagh

Storm Bronagh was an extratropical cyclone that originated south of Newfoundland on the 19 September 2018. It tracked eastwards across the North Atlantic (red track in Figure 2.1b) deepening from 1008 hPa at 2100 UTC on 19 September 2018 to 985 hPa at 0000 UTC on 21 September 2018 (Figure 2.1a). During this time, storm Bronagh caused localised flooding in parts of England and Wales where daily rainfall totals exceeding 50 mm were recorded in upland areas of Wales, the southern Pennines and North York Moors (Met Office, 2018). The extreme rainfall and winds associated with storm Bronagh led to travel disruptions throughout the

UK. Following this, storm Bronagh continued to track north-eastwards and deepen further. Its minimum mean sea level pressure of 966 hPa (and maximum relative vorticity of 8.97 $\times$ 10^{-5} s^{-1}, not shown) occurred at 1800 UTC on 22 September 2018 over the Norwegian sea (Figure 2.1a).

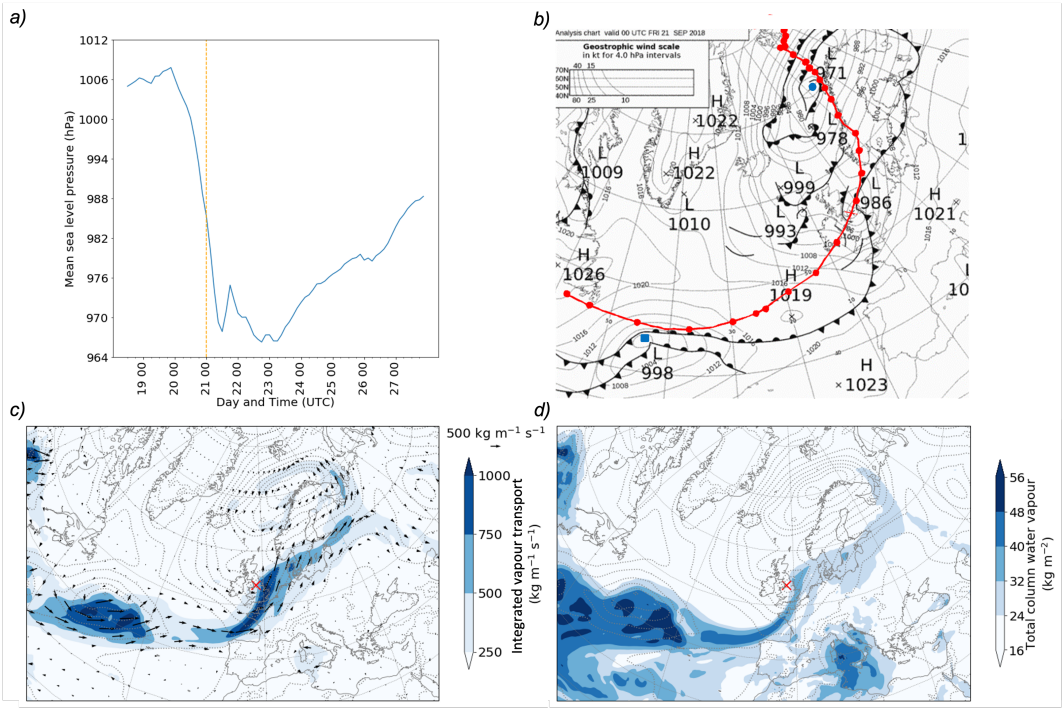

Figure 2.1: (a) Evolution of storm Bronagh's central mean sea level pressure (hPa). The vertical line corresponds to 0000 UTC 21 September 2018. (b) Met Office surface analysis chart at 0000 UTC on 21 September 2018 (©2018 Crown copyright). The red solid line represents storm Bronagh's track. The position of the cyclone's centre at 6-hourly intervals are shown as red circles. The blue circle represents the centre of storm Ali, the red cross represents storm Bronagh's centre and the blue square represents the cyclone centre of storm C at 0000 UTC on 21 September 2018. (c) ERA5 IVT (filled contours and vectors) and (d) ERA5 TCWV (filled contours) at 0000 UTC on 21 September 2018. Panels (c) and (d) are overlaid with ERA5 mean sea level pressure (grey contours).

Storm Bronagh occurred during a period of intense cyclonic activity in the North Atlantic starting with post-tropical cyclone storm Helene, which passed over the UK

on 17 September 2018 (Gentile et al., 2021b). This was followed by storm Ali on 18 September and then storm Bronagh on the 20–21 September. The decaying storm Ali can be seen to the north of storm Bronagh in Figure 2.1b with a central pressure of 971 hPa. A third cyclone in its developing stage with a central pressure of 998 hPa can also be seen in Figure 2.1b in the mid-North Atlantic (43°W, 44°N) (hereafter storm C). Storm Ali, storm Bronagh and storm C form a family of extratropical cyclones with each subsequent cyclone forming on the trailing cold front of the previous cyclone. Associated with storm Ali, storm Bronagh and storm C is a filament of IVT exceeding 250 kg $m^{-1}s^{-1}$ (Figure 2.1c) and a corresponding filament of enhanced TCWV (Figure 2.1d). Thus an atmospheric river of several thousand kilometres length and a few hundred kilometres width can be identified originating at 30°N and extending across the North Atlantic and into north-west Europe (ending around 70°N). The moisture flux within the atmospheric river is higher in the vicinity of storm Ali, storm Bronagh and storm C due to the increased horizontal pressure gradients and hence increased wind speeds associated with each cyclone. Similar analysis has been performed at earlier and later times and at all stages in storm Bronagh's life-cycle an atmospheric river is identified in the vicinity of the storm (not shown).

As described in the introduction, IVT alone cannot be used to determine if moisture originating at the start of the atmospheric river is transported into the centre of storm Bronagh to produce the heavy precipitation associated with the storm. To determine where moisture leading to precipitation is transported from, it is necessary to calculate the moisture flux in the frame of reference of the moving cyclone. In the following section we calculate the cyclone-relative flow and moisture flux on the 300 K isentropic surface.

2.5 Cyclone-relative isentropic flow

Figures 2.2a–d show fields in a domain that is centred on the position of storm Bronagh at 0000 UTC on 21 September (2018) (red cross in Figure 2.2a). Figure 2.2a shows pressure on the 300 K isentropic surface. The 300 K isentropic surface slopes in the vertical from below 800 hPa in the cyclone's warm sector to 300 hPa in the cold sector. The steepest slopes are co-located with the position of the cyclone's cold and warm fronts. Figure 2.2a also shows the specific humidity on the 300 K surface within the domain. As expected, relatively high specific humidity values are found closer to the surface, below 700 hPa.

Moisture flux (wind vectors multiplied by specific humidity) and wind vectors on the 300 K isentropic surface in an Earth-relative framework are shown in Figure 2.2b. Moisture flux on this isentropic surface is highest to the south of the cyclone centre in a band extending along the cyclone's cold front. This is similar to the IVT shown in Figure 2.1c. Assuming a stationary cyclone, in an Earth-relative framework the flow on the 300 K isentropic surface appears to descend behind the surface cold front, cross the cold front boundary and then to ascend over the surface warm front. However, the storm is not stationary but is travelling towards the north-east at about 19 m s^{-1}. Therefore, the cyclone velocity is of a similar magnitude and direction to the wind vectors within the region of high Earth-relative moisture flux.

Moisture flux and wind vectors on the 300 K isentropic surface in a cyclone-relative framework are shown in Figure 2.2c. The cyclone-relative moisture flux and wind vectors are calculated by subtracting the cyclone velocity from the wind vectors. In the cyclone-relative framework the flow on the isentropic surface looks very different. To the west of the cyclone centre air descends from 400 hPa to 700 hPa along the sloping isentropic surface. At this point the airflow splits into two branches. One branch turns cyclonically towards the cyclone centre at 700 hPa. The other branch descends further to 800 hPa and turns anticyclonically away from

the cyclone centre. This dry cyclone-relative airflow is the dry intrusion shown in Figure 1.8. To the east of the cyclone centre air ascends from 800 hPa to 500 hPa where it then turns cyclonically and wraps around the cyclone centre. This moist cyclone-relative airflow is the warm conveyor belt shown in Figure 1.8. To the south-east of the cyclone centre the cyclone-relative airflow on the 300 K isentropic surface is confined to the lower-troposphere, 850–950 hPa. This airflow is directed towards the cold front where it splits into two branches. One branch turns towards the cyclone centre and ascends slightly. The other branch travels parallel to the surface cold front directed away from the cyclone centre. This moist low-level airflow is the feeder airstream shown in Figure 1.8.

At the interface between the dry intrusion and the feeder airstream there is a saddle point in the cyclone-relative flow and therefore, there is a region where the flow becomes stationary. As a result, the isentropic cyclone-relative moisture flux is small in this region. In Figure 2.2c, cyclone-relative moisture fluxes smaller than 30 g kg^{-1} m s^{-1} are observed over north-west France indicating the position of the saddle point. The presence of a saddle point within the identified atmospheric river (as shown in Figure 2.1c) shows that only moisture within the portion of the atmospheric river downstream of the saddle point (i.e. between the saddle point and the cyclone centre) can be transported into the centre of the cyclone. Moisture within the portion of the atmospheric river upstream of the saddle point is not travelling as fast as the cyclone itself so will get further from the cyclone as it travels, effectively being left behind by the poleward moving cyclone.

2.6 Saddle point identification diagnostic

In this section an algorithm for objectively identifying saddle points in lower-tropospheric cyclone-relative airflows that occur in the warm sector of storm Bronagh is described. The algorithm is developed so that it can automatically be applied to many cyclones

in future work. In order to focus on lower-tropospheric airflows, the search is confined to the portion of the isentropic surface that is below 800 hPa (pressure greater than 800 hPa) within 2000 km of the cyclone centre. Within this part of the isentropic surface, regions where the cyclone-relative moisture flux is small, i.e. within the lowest 5% of values are identified using a watershed algorithm (Najman and Schmitt, 1994) (See Text Box A). To differentiate the minima found by the watershed algorithm in the cyclone-relative moisture flux that are associated with low specific humidity from those that are associated with saddle points, locations where the Jacobian determinant of the moisture flux field, det(**J**), is negative (See Text Box B) are identified. This latter criterion comes from nonlinear systems theory for the classification of hyperbolic fixed points (e.g., Figure 6.4 in Drazin, 1992).

The criteria above is applied to storm Bronagh at 0000 UTC on 21 September 2018 is shown in Figure 2.2d. The contour corresponding to the lowest 5% of cyclone-relative moisture flux values on the 300 K isentropic surface (below 800 hPa) is represented by the dashed contours. Low cyclone-relative moisture flux values are found behind the cold front and ahead of the warm front where specific humidity decreases due to the sloping nature of the isentropic surfaces. Low cyclone-relative moisture flux values are also found in a small region ahead of the cold front. Identified cyclone-relative moisture flux minima are shown in black dots. Finally, det(**J**) is calculated and negative values co-located with the minima are searched for, indicating saddle points in the moisture flux field. Only the moisture flux minima to the south of the cyclone centre satisfy all of the criteria so are identified as saddle points. This region is indeed co-located with the region identified in Figure 2.2c at the interface between the feeder airstream and the dry intrusion.

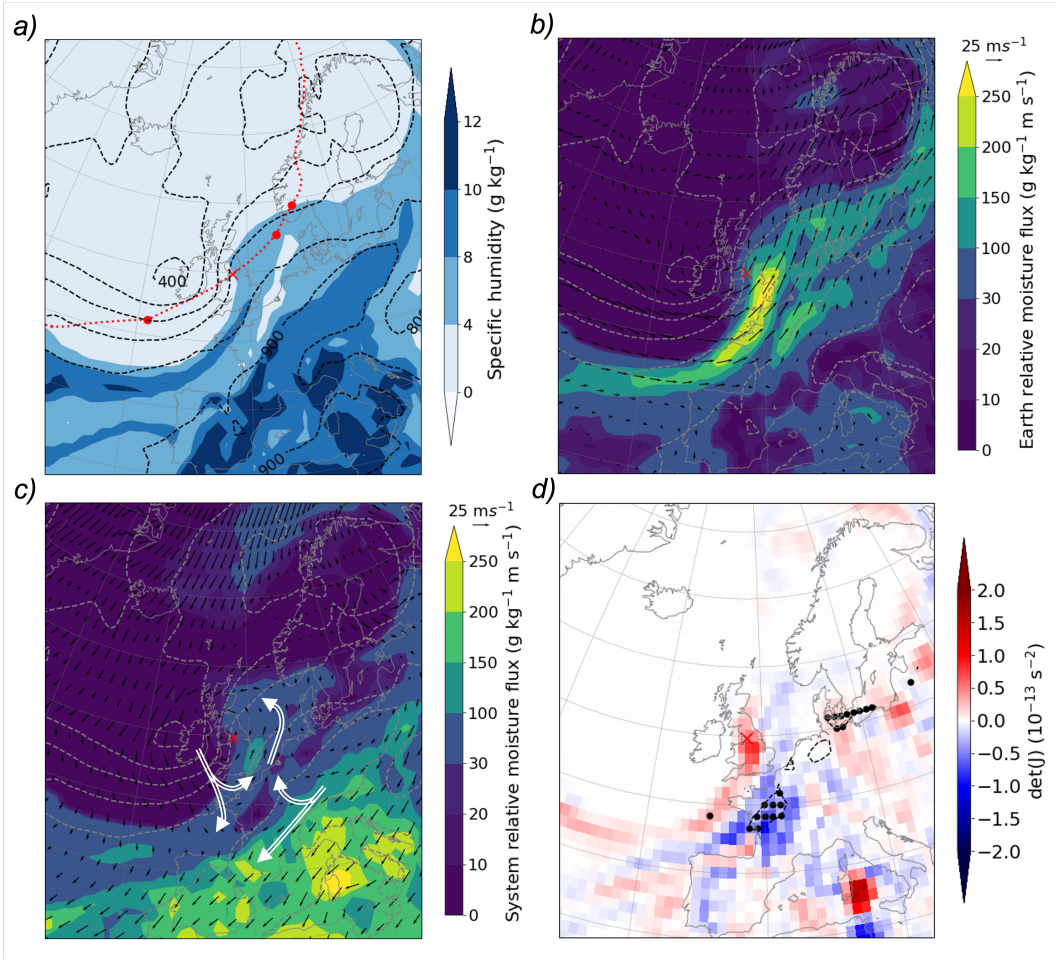

Figure 2.2: Fields on the 300 K isentropic surface (a) Pressure (hPa, dashed contours) and specific humidity (filled contours) overlaid with storm Bronagh's track (red dashed). The cyclone centre at 0000 UTC 21 September 2018 is marked by a red cross. The centre of the storm at 1200 UTC 20 September 2018, 0900 UTC 21 September 2018 and 1500 UTC 21 September 2018 (red dots) are shown from left to right respectively. (b) Earth-relative moisture flux (shaded), pressure (hPa, dashed contours) and Earth-relative horizontal wind (arrows). (c) Cyclone-relative moisture flux (shaded), pressure (hPa, dashed contours) and cyclone-relative horizontal wind (black arrows) overlaid with position of cyclone airflows (white arrows). (d) det($\mathbf{J}$) (shaded) and the 5$^{\text{th}}$ percentile in cyclone-relative moisture flux (dashed line). This panel also includes the minima identified by the watershed algorithm (black dots).

2.7 The feeder airstream in storm Bronagh

Figure 2.3 shows the location of identified saddle points in the 300 K isentropic cyclone-relative moisture flux at various times in the evolution of storm Bronagh. The fields are centred on the cyclone positions shown in Figure 2.2a. At all stages the regions identified as saddle points are located in the cyclone's warm sector ahead of the cold front. In Figure 2.3a the region associated with the saddle point is situated south of the cyclone centre. However, as the storm evolves, the saddle point moves eastwards and the cold front becomes more meridionally oriented as shown in Figure 2.3b, c and d. Furthermore, these saddle points are found at the leading edge of the filament of high TCWV. The cyclone-relative moisture flux in the part of the filament upstream of the saddle point is directed away from the cyclone centre indicating that moisture in this part of the filament is travelling slower than the cyclone. Thus, this moisture cannot feed into the base of the ascending warm conveyor belt and therefore, will remain in the lower atmosphere. Conversely, the cyclone-relative moisture flux downstream of the identified saddle points is directed towards the cyclone centre and will feed into the warm conveyor belt where it will ascend leading to the formation of clouds and precipitation. This is supported by the decrease in TCWV around the saddle point with time. In Figure 2.3a there is greater than 40 kg m^{-2} within the vicinity of the feeder airstream, however by Figure 2.3d this has decreased.

2.8 Conclusions

In this paper, an algorithm for identifying the feeder airstream in a case study, storm Bronagh, is described and the results for the identification of the feeder airstream throughout the storm's evolution is presented. Storm Bronagh was responsible for flooding and strong winds in the UK on the 20–21 September 2018. Using a threshold

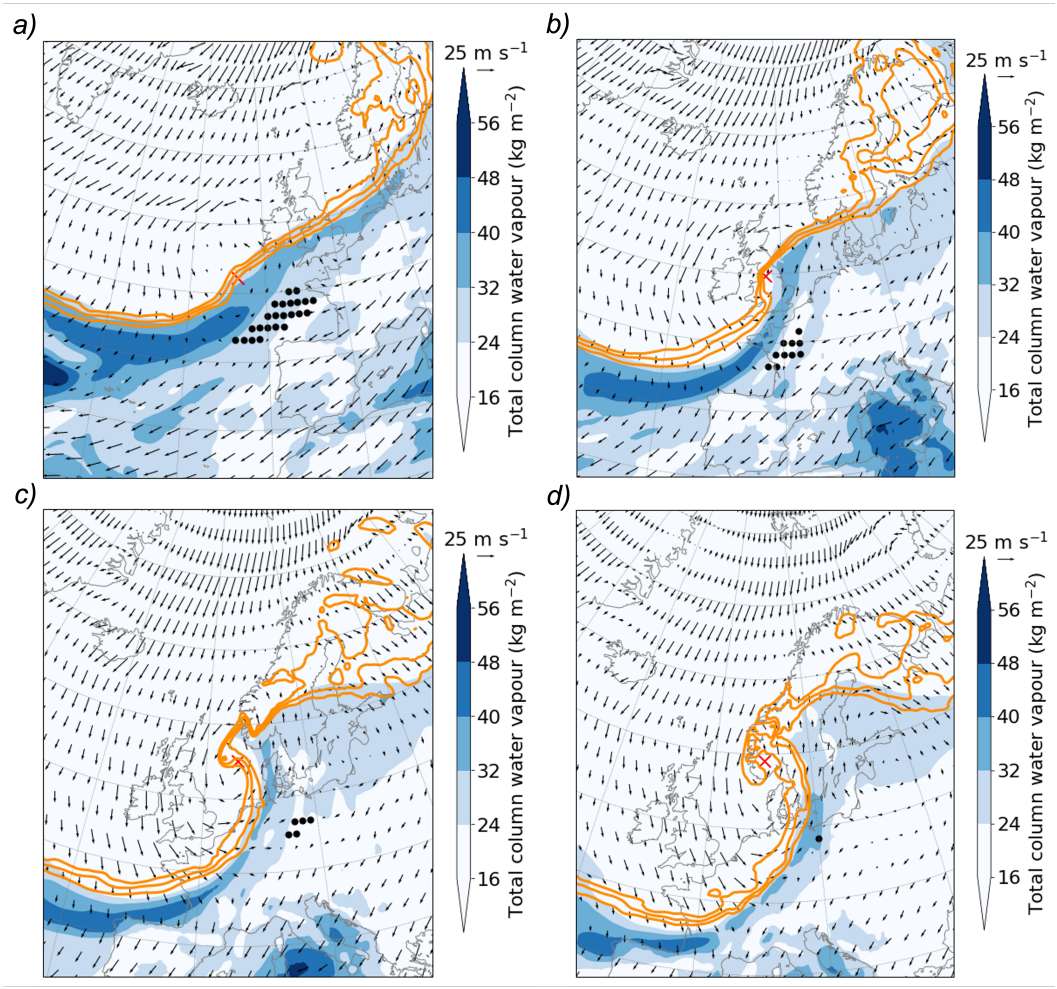

Figure 2.3: TCWV (filled contours), saddle points (black dots) and cyclone-relative wind vectors on the 300 K isentropic surface at (a) 1200 UTC 20 September 2018, (b) 0000 UTC 21 September 2018, (c) 0900 UTC 21 September 2018 and (d) 1500 UTC 21 September 2018. The panels also include the 290, 292 and 294 K potential temperature contours at 850 hPa (orange contours).

of vertically integrated moisture flux, an atmospheric river associated with this storm is identified and the characteristic cyclone airflows (dry intrusion, warm conveyor belt and feeder airstream) are also identified using isentropic cyclone-relative flow. In order to ascertain where the moisture responsible for storm Bronagh's precipitation is transported from, a diagnostic is developed to identify the presence of saddle points in the cyclone-relative moisture flux field. These saddle points occur at the interface of the descending dry intrusion behind the cold front and the low-level

feeder airstream ahead of the cold front. Presence of a saddle point within the identified atmospheric river indicates that moisture upstream of the saddle point cannot contribute to the moisture ascending in the warm conveyor belt. Absence of a saddle point within an atmospheric river indicates that moisture within the atmospheric river can be transported to the base of the warm conveyor belt and thus contributes to large scale precipitation.

Applying the saddle point diagnostic to the evolution of storm Bronagh shows that saddle points are identified within the atmospheric river during its passage over the UK and north-west Europe. The presence of such saddle points indicates that moisture is transported to the warm conveyor belt in storm Bronagh from in the local environment in which Bronagh is developing and not from the start of the atmospheric river, i.e. in the sub-tropics. Future work will include applying this diagnostic to a large set of cyclones to construct a climatology of the feeder airstream. This large set will include cyclones with varying intensity, genesis location and cyclone types to determine systematically when and where a feeder airstream is present.

The diagnostic developed in this paper only determines where the moisture contributing to large scale precipitation is transported from. It is plausible that forced ascent of moist air in the atmospheric river over the hills in the UK may also have led to the formation of orographically generated precipitation. Future work will include simulations of study of storm Bronagh using the UK Met Office 1.5 km resolution numerical weather prediction model to determine the relative contributions of large scale precipitation associated with the warm conveyor belt ascent and locally forced precipitation associated with orographic ascent.

2.9 Appendix

2.9.1 Text Box A: The detection of minima in the moisture flux field

To evaluate the Jacobian determinant of the linearised moisture flux at a fixed point, the fixed points must firstly be identified in an objective manner. To do so, an image segmentation tool called the watershed algorithm is used. This algorithms treats the field of interest like topography such that the minima of interest are depicted as basins. To find different basins, the topography is submerged in a lake so that each basin fills up with water according to their depth. The location in which the water meets, marks the edge of each basin. Therefore, the location and area that the minima span is known. To define how much the topography is submerged, and therefore the area that the identified minima span, a threshold value is used (Najman and Schmitt, 1994).

The input of the watershed algorithm is a two-dimensional array of the field of interest. The output is a two-dimensional array which is the same size as the original field of interest. This array contains clusters of points giving the location each minima. Each cluster of points are given a numerical value according to the minimum they are associated with. For example, if ten grid-points fall within the region associated with one minimum, then there will be ten ones at that location in the array. If five grid-points fall within a region associated with a second minimum, then five twos will be at that location in the array. And so on and so forth. If no minima are identified then the output will be a two-dimensional array of zeros, the same size as the original field of interest.

2.9.2 Text Box B: The detection of saddle points and the feeder airstream

To develop an identification algorithm for the presence of saddle points associated to a feeder airstream at a given time during the evolution of the cyclone, the instantaneous configuration of the cyclone-relative low-level moisture flux is relied upon. If present, the feeder airstream splits into two branches on approach to the system's cold front (Figure 1.8). A branch with a southerly component will then feed moisture into the system's warm conveyor belt. A branch with a northerly component will tend to leave the cyclone's immediate neighbourhood and transport moisture rearwards with respect to the cyclone centre. The moisture flux vector field near the splitting point will constitute a fixed point, i.e a point for which the vector field is zero, and will have a similar configuration to that of a saddle point in the phase space of linearised second-order differential systems (e.g., Figure 6.4 in Drazin, 1992). Therefore, the Jacobian determinant of the isentropic moisture flux is calculated using the classification of fixed points from nonlinear systems theory (see e.g., Drazin, 1992). This determinant is given by:

$$\det(\mathbf{J}) = \frac{\partial(qu)}{\partial x}\frac{\partial(qv)}{\partial y} - \frac{\partial(qu)}{\partial y}\frac{\partial(qv)}{\partial x}, \tag{2.1}$$

where u and v are the eastward and northward components of wind, respectively, x and y are the eastward and northward pointing coordinates, respectively, and q is specific humidity, all on an isentropic surface. According to this method, a saddle point will be characterised by a negative Jacobian determinant of the linearised moisture flux when evaluated at a fixed point. The partial derivatives in the Jacobian determinant on the longitude-latitude grid are calculated using a centred difference approach such that the determinant is calculated over a grid with 200km grid spacing.

CHAPTER

THREE

MOISTURE TRANSPORT AND CYCLONE CHARACTERISTICS IN A CLIMATOLOGY OF CYCLONES

Using a case study, storm Bronagh, it has been shown that moisture is transported to the base of the warm conveyor belt from the environment into which the storm is developing into. This is done using an identification algorithm that identifies a region associated with a low-level flow called the feeder airstream. The presence of this region indicates that moisture is transported to the base of the warm conveyor belt from the environment ahead of the cyclone via the feeder airstream.

To determine whether moisture is transported from ahead of the cyclone centre at other stages in a cyclone life-cycle, in weaker storms or in slower moving storms, the presence of the feeder airstream is investigated in a climatology of storms that occur in the extended winter period from 1979 to 2019 in the midlatitude northern hemisphere. Subsets of storms are created by grouping storms with decreasing maximum intensities at different times in the storms evolution and by grouping storms with decreasing propagation velocities. It is hypothesised that these characteristics will have an effect on the direction of moisture transport. The presence of the feeder airstream in each data-set is tested using two approaches. The first involves creating composite data for each data-set and comparing the fields. The second involves

applying an identification algorithm (based on the algorithm introduced in Cuckow et al. (2022)) to each storm in the data-sets. This gives insight into when and where moisture is likely to be transported to the base of the warm conveyor belt from the environment ahead of cyclone.

3.1 Data

3.1.1 Cyclone tracking and data

Similarly to Cuckow et al. (2022), the tracking algorithm of Hodges (1994, 1995, 1999) is used to identify the tracks of storms. This algorithm uses 3-hourly 850 hPa relative vorticity as the feature tracking variable. The vorticity field is truncated to T-42 resolution to emphasise the synoptic scales and track synoptic scale features. Changes in speed and direction of the feature are limited to produce a smooth track. To eliminate weak features, features with a maximum relative vorticity below 1×10^{-5} s^{-1} are removed. An advantage of using relative vorticity as the feature tracking variable in comparison to mean sea level pressure, is that cyclone tracks are identified earlier in their development, and later in their decay, when isobars may not be closed. Therefore, using the algorithm of Hodges (1999) allows the feeder airstream to be investigated over a larger temporal range. It is useful to note when interpreting results from storms early in cyclogenesis, into their decay, and weaker cyclones in general, that there is less consistency among tracking algorithms (Neu et al., 2013). This is due to the signal from the feature tracking parameter showing distinct values. Therefore, this study uses storms that occur during the extended winter period.

The European Centre for Medium Range Weather Forecasts (ECMWF) ERA5 atmospheric reanalysis data-set is used to investigate surface fields and fields on isentropic surfaces. Reanalysis data is produced by combining historical atmospheric

observations with a comprehensive numerical weather prediction model of the atmosphere using data assimilation, thus providing a single data-set of the global atmosphere, land surface and ocean waves. The ERA5 data-set is created using the Integrated Forecasting System (IFS) from ECMWF. The surface and isentropic fields used in this study have a 1° and a 0.25° horizontal resolution respectively, and a 3 hourly temporal resolution which allows a detailed analysis of weather phenomena, such as cyclones, to be conducted (Hersbach et al., 2020). A comparison between ERA5 data and synoptic data has been made and has shown that ERA5 suitably captures the synoptic scale features of interest in this study.

3.1.2 Extratropical cyclone data-set

To identify the feeder airstream in a wide variety of storms, storms that occur during the extended winter period from 1979 to 2019 (October 1979 - March 2019) with maximum intensity in the extratropical northern hemisphere (30° - 90°N) are used in this study. This is done to use a larger spatial and temporal range of storms than those used in Dacre et al. (2019). In this study, intense storms occurring in winter from 1989 to 2009 (December 1989 - February 2009) with maximum intensity in the North Atlantic (70° - 10°W, 30° - 90°N) are used.

Using the tracking algorithm of Hodges (1999), and removing any short lived or tropical cyclones (done by excluding any track shorter than 48 hours or with a maximum vorticity occurring equatorwards of 30°N) approximately 40,000 cyclones are identified from 1979 to 2019. Applying an identification algorithm to this number of cyclones would be computationally expensive so to reduce the number of storms, 1000 storms are randomly sampled from the 40,000 cyclones. This process is repeated five times to ensure that the random sampling method captures the characteristics of all the tracks identified. It is found that the probability density distributions (of parameters such as relative vorticity and propagation velocity) for all

5 randomly sampled data-sets and the original data-set have similar characteristics and closely resemble each other.

3.1.3 Extracting fields around the cyclone centres

To to identify which storms in the data-set have feeder airstream and the time in the storms evolution this occurs, the required fields (IVT and mean sea level pressure and fields on isentropic surfaces such as pressure, specific humidity and Earth-relative winds) are extracted from ERA5 using the position of each storm along it's track at each time-step as a reference. At each time-step along a storms track, a circular cutout of each field is taken around the centre of the storm using a 20 ° radius. To ensure that the grid size does not vary depending on the latitudinal position of the storm, a polar stereographic projection is used to take the circular cut out. This means that the cyclone centre is moved so that it is centered on the North pole. The cut out around the centre starts to the left of the cyclone centre and is taken anticlockwise. Therefore, the north of the domain is at the top. This process is repeated for each storm so that the fields around the centre of each storm at each time-step during the storms evolution are available for analysis. By taking a circular cut out of these fields, the fields can be composited. This technique involves taking an average of the fields of interest over a range of storms. Therefore, common features of the extratropical cyclones can be examined if their position coincides.

So that a comparison between the stage that each cyclone is in, the time that the data is extracted along each cyclone track is given a value relative to the time of the cyclone's maximum intensity (T+0). Therefore, T-24 hours would refer to 24 hours prior to maximum intensity. The data is extracted from T-60 to T+60 in 6 hourly increments.

To examine the feeder airstream, data is extracted from ERA5 on the 265, 275, 285, 300, 310 and 320 K isentropes. This is because not all isentropic surfaces will

be suitable for analysis of a low-level flow. Whilst a low-level (cooler) isentrope would be used in an ideal scenario, there will be some scenarios where the isentrope will intersect the ground, particularly when a storm is located over a region of high orography. Therefore, a warmer isentrope might be needed. Additionally, potential temperature decreases towards the poles and therefore, to analyse low-level flows at the same height above sea level, a cooler isentrope might be needed.

3.1.4 Sub-sets of data created using intensity and propagation velocity

For the purpose of this investigation, sub-sets of data are created from the 1000 sampled storm tracks to investigate the relationship between the feeder airstream, and the intensity and propagation velocity of the storm. To investigate intensity, the maximum intensity of each storm in terms of 850 hPa relative vorticity (at T-42 resolution) is used. The storm tracks are placed in a descending order using their maximum intensity and are then separated into four data-sets. Storm tracks with a storm number between 1-250, 251-500, 501-750 and 751-1000 are grouped together. The 1-250 data-set has the most intense storm tracks and the 751-1000 data-set has the weakest. These data-sets and their labels are listed in table 3.1 where I_1, I_2, I_3 and I_4 corresponds to the data-sets with storm numbers 1-250, 251-500, 501-750 and 751-1000 respectively.

Due to issues with extracting large amounts of data (related to IDL licensing issues), 70 of the randomly sampled 1000 storm tracks do not have data available, leaving 930 storm tracks. Therefore, the number of storms in each data-set varies. Furthermore, as the track length varies for each storm, not all the tracks will be long enough to have data at each time-step between T-60 to T+60. Therefore, the number of storms with data available at each time will vary. This is demonstrated in figure 3.1 which shows the number of storms in each data-set over time for data-

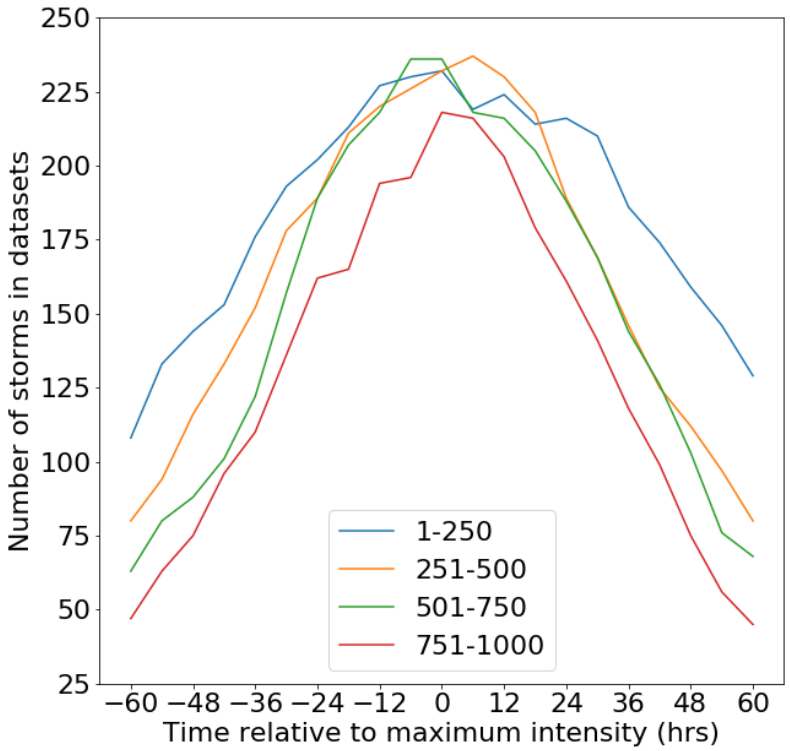

Figure 3.1: The number of storms in data-sets I_1 (1-250), I_2 (251-500), I_3 (501-750) and I_4 (751-1000) over time

sets I_1 to $_4$. For all data-sets, there are the least number of storms at T-60, the number of storms then increases until approximately T+0. The number then begins to decrease again as the time approaches T+60.

The same process used to create data-sets with decreasing propagation velocities. However, instead of using cyclone tracks, the propagation velocity is found at each time-step along each storm track. This is done for times between T-54 to T+54 and is calculated using a centred difference approach. The propagation velocities are then placed in descending order regardless of the storm tracks they are associated with. Therefore, this data-set has 12522 cyclone time-steps in it, rather than 1000 storm tracks. This allows the relationship between propagation velocity and the feeder airstream to be investigated independently from the stage in the cyclone's evolution. Four data-sets are created using quartiles in the number of time-steps available. Therefore, these data-sets contain storm time-steps between 1-3130, 3131-

6260, 6261-9390 and 9391-12522. These data-sets and their labels are listed in table 3.1 where U_1, U_2, U_3 and U_4 corresponds to the data-sets with time-steps 1-3130, 3131-6260, 6261-9390 and 9391-12522 respectively.

Table 3.1: Table outlining the data-sets used for the investigation into the relationship between the feeder airstream, intensity and propagation velocity.

Parameter	**Storm Number**	**Number of Storms**	**Range of Values (10^{-5} s^{-1})**	**Label**
Maximum intensity	1 - 250	232	7.87 - 15.2	I_1
Maximum intensity	251 - 500	235	5.91 - 7.86	I_2
Maximum intensity	501 - 750	237	4.12 - 5.91	I_3
Maximum intensity	751 - 1000	226	1.77 - 4.12	I_4
Parameter	**Storm time-steps**	**Number of time-steps**	**Range of Values (m s^{-1})**	**Label**
Propagation velocity	1 - 3130	2895	14.9 - 35.5	U_1
Propagation velocity	3131 - 6260	2903	10.2 - 14.9	U_2
Propagation velocity	6261 - 9390	2904	6.29 - 10.2	U_3
Propagation velocity	9391 - 12522	2925	0.166 - 6.29	U_4

To understand how the propagation velocity in data-sets I_1 to I_4 evolve, the mean propagation velocity of each data-set is analysed as a function of time. This is shown in Figure 3.2. For each data-set, the propagation velocity increases until it reaches a maximum during the storms developing stages. The storms then slow down as they continue to develop, reach maximum intensity and enter their decay phase. The more intense storms, on average, move quicker during their intensification stage and reach their fastest propagation velocity earlier in their evolution in comparison to

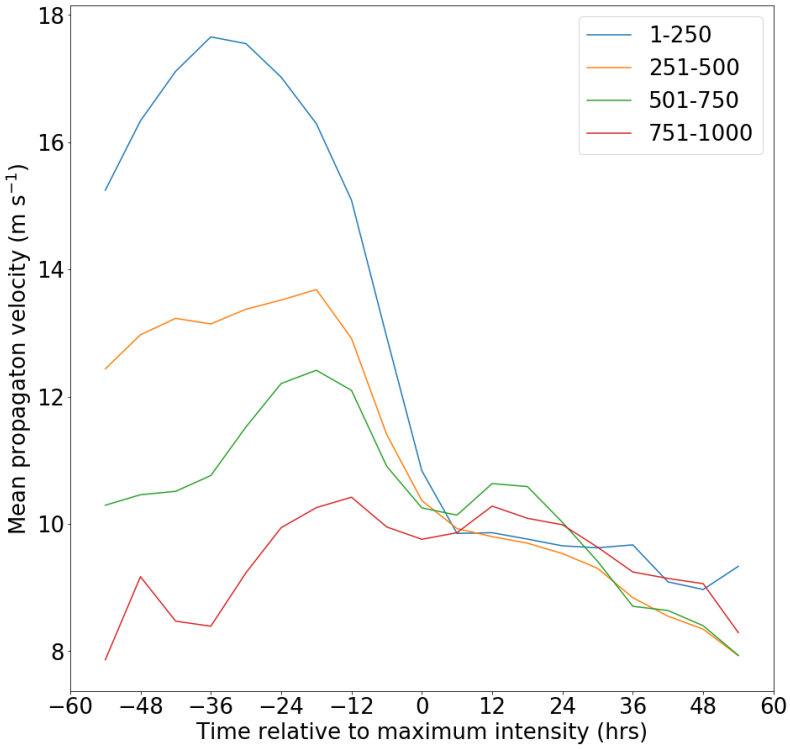

Figure 3.2: The mean propagation velocity of the cyclones in the intensity data-sets I_1 (1-250), I_2 (251-500), I_3 (501-750) and I_4 (751-1000) over time.

the weaker storms. This is consistent with the work of Hoskins and Hodges (2002) who found that cyclone tend to move quicker during their developing stages. It is also consistent with the work of (Owen et al., 2021) that suggested that more intense cyclones have a faster mean speed than weaker ones. It is useful to note that the spread of propagation velocities for the intensity data-sets at each time relative to maximum have not been investigated. Therefore, to fully understand the relationship between intensity and propagation velocity, further investigation is needed.

3.2 The feeder airstream in composite data

3.2.1 The feeder airstream in composite data with decreasing intensities

Using data-sets I_1 to I_4, composite data is created to ascertain the direction of moisture transport throughout the evolution of storms with decreasing intensities. The composite fields are calculated by finding the average of the fields in each data-set at T-24, T+0 and T+24 hours relative to maximum intensity (excluding any points that lie beneath the ground on the isentropic surfaces). The composite surface level and vertically integrated fields for I_1 to I_4 (top to bottom) are shown at T-24, T+0 and T+24 (left to right) in Figure 3.3.

As the mean sea level pressure is related to the intensity of the storms, the mean sea level pressure centres of the data-set I_1 are the lowest. As the data-sets decrease in intensity the mean sea level pressure centre increases. From T-24 to T+0, the mean sea level pressure centre in all data-sets gets deeper (decreases) as the storms reach maximum intensity. From T+0 to T+24 the mean sea level pressure increases again, signifying that the cyclones have entered their decay phase.

The IVT also decreases as the intensity of the storms in each data-set decreases. Using 250 kg m^{-1} s^{-1} as the threshold to define an atmospheric river, there are only atmospheric rivers associated with data-set I_1 at T-24, T+0 and T+24 (figures 2.1a, b and c) and I_2 at T-24 and T+0 (figures 2.1d and e). The IVT is on average higher in data-set I_1 in comparison to I_2. The IVT centroid decreases and moves anticlockwise from the south to the east of the cyclone centre as the storms evolve. The centroid in data-set I_1 at T+24 is also further away from the cyclone centre than at T-24 and T+24.

To analyse the ascending and descending flows in the vicinity of fronts, the Earth-relative winds, specific humidity and pressure on a 285 K isentrope are shown

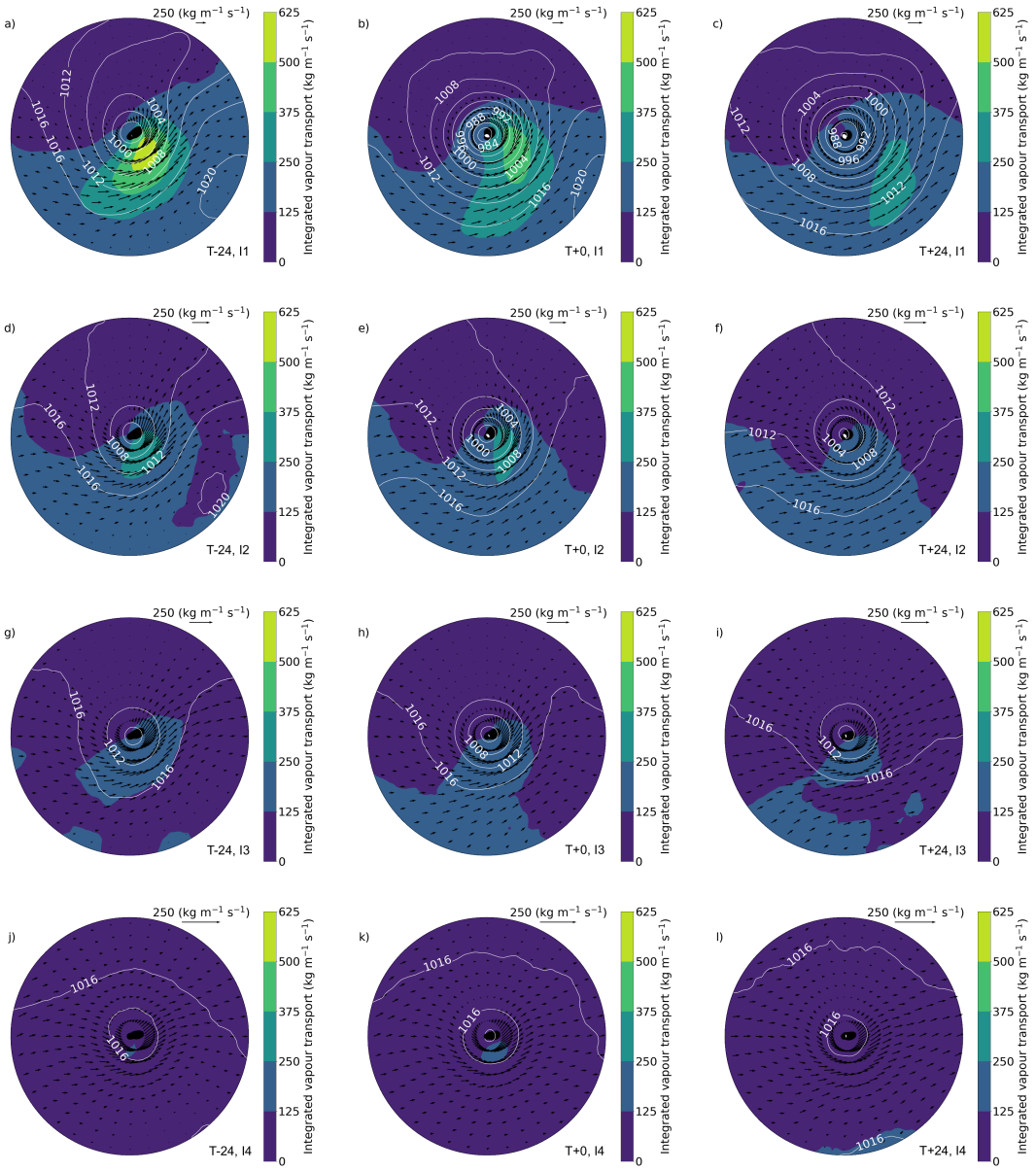

Figure 3.3: The composite data for mean sea level pressure (hPa, white contours), and IVT (kg m^{-1} s^{-1}, filled contours and vectors) for each data-set I_1 to I_4 (top to bottom) at T-24, T+0 and T+24 hours relative to maximum intensity (left to right).

in Figure 3.4 for I_1 to I_4 (top to bottom) at T-24, T+0 and T+24 hours relative to maximum intensity (left to right). The 285 K isentrope slopes in the vertical as show by the isobars. The steepest slopes (shown by the largest pressure gradient) are often co-located with the position of a cyclone's cold and warm fronts and the strength of the pressure gradient along the isentrope gives an indication of how strong the

front is. High values of specific humidity can give an indication of where the warm sector of a cyclone is if they are located at lower-levels and in between the strong pressure gradients created by the fronts. The fronts can be seen in the I_1 data-set (figure 3.4a) where the pressure gradient increases between 650 and 950 hPa.

The strongest fronts are seen in the I_1 data-set (figures 3.4a, b and c) as the pressure gradient along the isentrope is largest in this data-set. As the data-sets decrease in intensity, the pressure gradient also decreases. The pressure gradient also decreases from T-24 to T+24 (i.e. as the cyclones reach maximum intensity and begin to decay) in data-sets I_1 to I_3 but remains constant in I_4. The orientation of the isobars (for example the 850 hPa isobar) close to and south of the cyclone centres in the I_1 data-set at T-24, T+0 and T+24 suggest that the cold front moves eastwards as the cyclone develops (consistent with the occlusion process and frontal fracture). This can also been seen in the I_2 data-set for T-24 (figure 3.4d) and T+0 (figure 3.4d) using the 800 hPa isobar.

In all data-sets at T-24, T+0 and T+24, the lines of constant specific humidity follow the shape of the isobars and an area of higher specific humidity typically lies in between the largest pressure gradient along the isentrope for data-sets I_1 to I_3. This suggests that these areas of higher specific humidity give an indication of where the warm sectors in the cyclones are. The specific humidity near the surface is highest in the I_1 data-set and decreases as the storms in the data-sets become weaker. The specific humidity near the surface also decreases as the storms evolve, except for data-set I_4 (3.4d). This could be because the storms in the I_4 move equatorwards as they evolve.

The Earth-relative winds in each data-set flow from west to east across the domain, descending down the isentrope on the west side of the cyclone centre, wrapping around the cyclone centre and then ascending on the east side. They are strongest in the I_1 data-set (as shown by the vector scale in Figure 3.4) and decrease as the

intensity of each data-set decreases. For data-sets I_1, the Earth-relative winds are slightly quicker at maximum intensity than they are at T-24 and T+24.

The strength and location of the pressure gradient, specific humidity and Earth-relative winds shown in Figure 3.4 suggest that these characteristics are related to the IVT seen in Figure 3.3. An atmospheric river is only present in the data-sets that contain the more intense storms (I_1 and I_2) with stronger Earth-relative winds, larger specific humidity near the surface and a larger pressure gradient along the isentrope. This suggests that the strength of an atmospheric river is linked to the strength of the fronts as well as the availability of low-level moisture and strength of the Earth-relative winds. Furthermore, the position of the IVT centroid moves ahead of the strong pressure gradient to the west of the cyclone centre and coincides with the region of higher specific humidity south of the cyclone centre. This suggests that the atmospheric rivers are located ahead of the cold fronts in the warm sectors of the cyclones, and that the position of the atmospheric rivers are linked to the motion of the cold fronts.

To assess the direction of moisture transport with respect to the cyclone centre, the composite cyclone-relative moisture flux and the Jacobian determinant of the linearised moisture flux (hereafter referred to as the determinant) on a 285 K isentrope are analysed. These are shown in Figure 3.5 for I_1 to I_4 (top to bottom) at T-24, T+0 and T+24 (left to right). The cyclone-relative moisture flux is calculated by subtracting the cyclone propagation velocity from the Earth-relative wind field, and by multiplying by the specific humidity. As the specific humidity tends to be larger at lower-levels, the moisture flux is also larger at lower-levels. The determinant analyses the gradient of the flow around each grid point in two directions and is used in the identification algorithm to identify a region associated with the feeder airstream. If an area of negative determinant coincides with a minimum in the cyclone-relative moisture flux, then a region associated with the feeder airstream

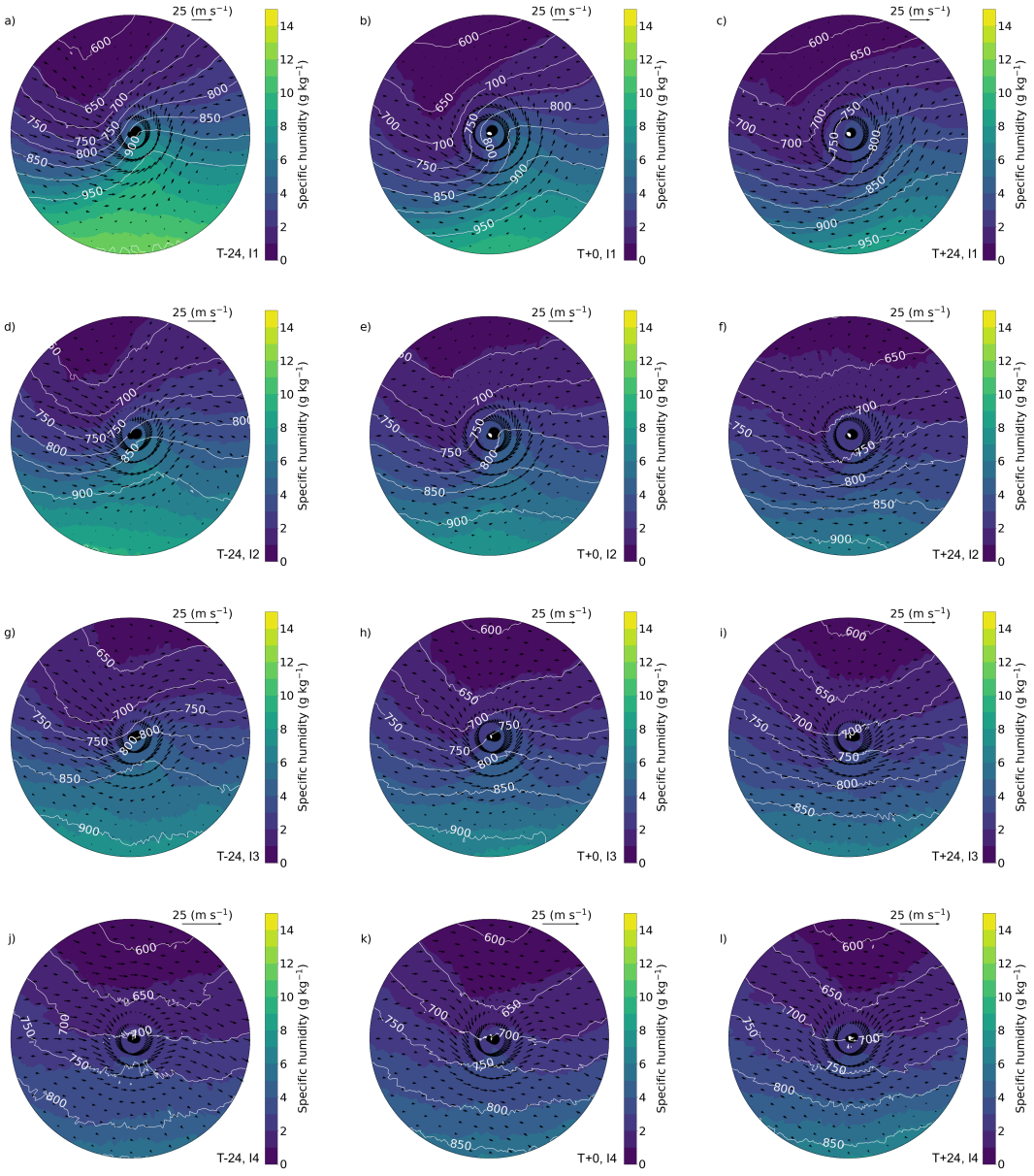

Figure 3.4: The composite data for pressure (hPa, white contours), specific humidity (g kg^{-1}, filled contours) and the Earth-relative winds (m s^{-1}, vectors) on the 285 K isentrope for each data-set I_1 to I_4 (top to bottom) at T-24, T+0 and T+24 hours relative to maximum intensity (left to right).

is identified.

In all data-sets at T-24, T+0 and at T+24, there is a low-level cyclone-relative moisture flux travelling from east to west across the domain. This moisture flux, splits into two branches, one of which ascends along the isentrope, and the other remains at low levels. For example, at T+0 hours for the I_1 data-set (figure 3.5b),

there is a flow approaching from the east, which is located below 900 hPa. One branch of this flow ascends up to 700 hPa and then turns cyclonically around the cyclone centre. The other branch continues towards the south west of the domain, remaining below 900 hPa. This is consistent with the feeder airstream, and suggests that there is a feeder airstream present in all data-sets at T-24, T+0 and at T+24. In data-set I_1, the saddle point associated with the feeder airstream moves ahead of the 800 hPa isobar within an area of higher specific humidity and moves further from the cyclone centre from T-24 to T+24 (figures 3.5a, b and c) suggesting that the movement of the feeder airstream saddle-point is related to the movement of the cold front and that the feeder airstream lies within the warm sector. Therefore, the location of the feeder airstream is related to the location of the atmospheric river. The minimum associated with the saddle point created by the feeder airstream either coincides with, or lies to the south west, of the centroid of the atmospheric river.

Whilst the direction of moisture flux across the domain at low-levels is the same, the magnitude varies in each data-set and varies with the time relative to maximum intensity, and the largest moisture flux is seen in data-set I_1 at T-24 hours relative to maximum intensity. The magnitude of the moisture flux decreases as the intensity decreases in each data-set. It also decreases from T-24 to T+24 in all data-set, except in data-set I_4 (figures 3.5j, k and l) where the magnitude of the moisture flux does not change during the storms evolution. This suggests that the strength of the low-level cyclone-relative moisture flux (i.e. the feeder airstream) is larger when the storms are more intense, and during the developing stages of the storm.

As shown in Figure 3.3, there is no identified atmospheric river in data-sets I_2 at T+24 hours and, in I_3 and I_4 at T-24, T+0 and T+24 as the moisture flux south of the cyclone centre is below 250 km m^{-1} s^{-1}. This shows that the strength of the feeder airstream is related to the strength (or existence using the 250 km m^{-1} s^{-1} threshold) of the atmospheric river. These results suggest that the presence of the

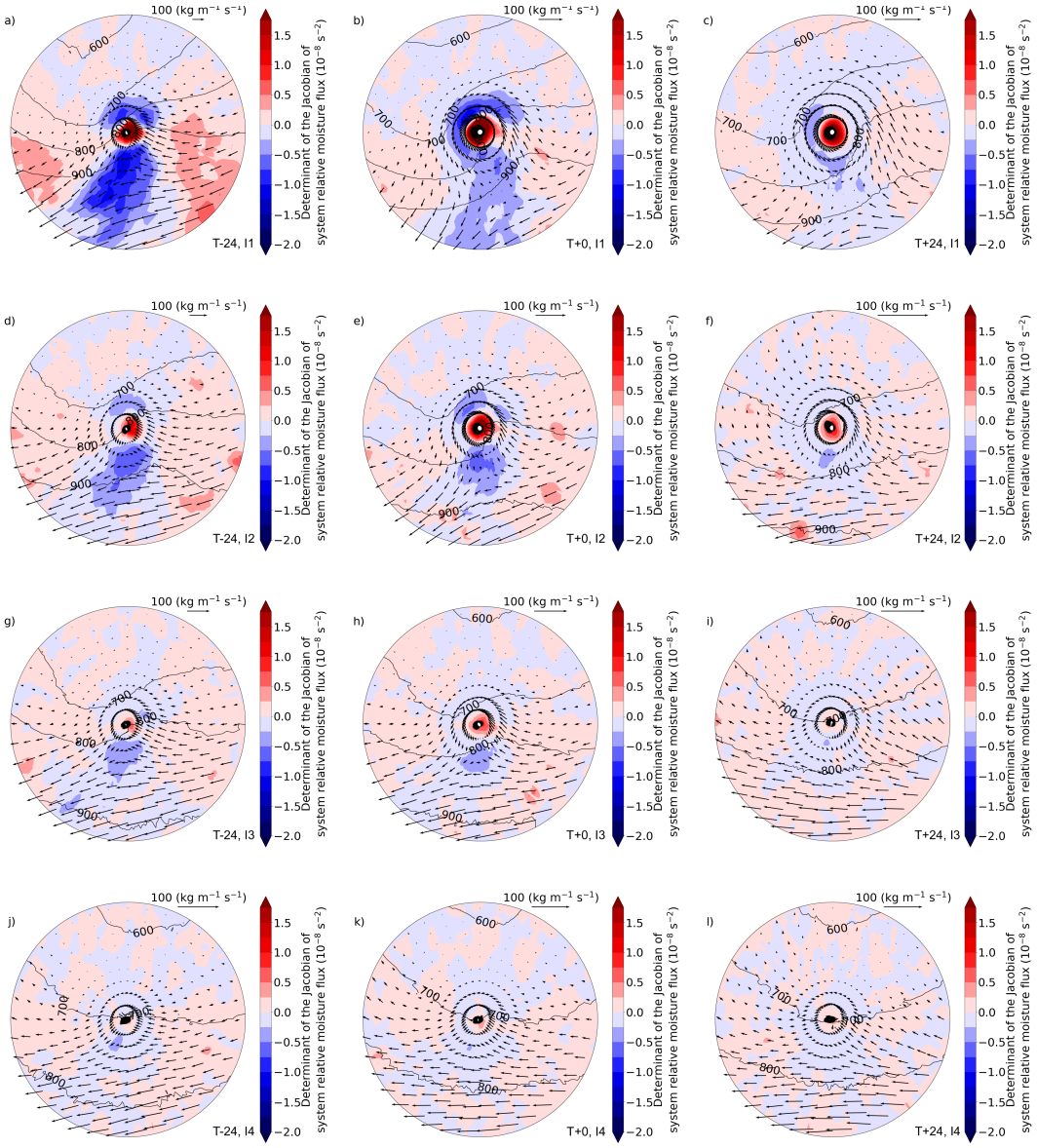

Figure 3.5: The composite data for pressure (hPa, black contours), the Jacobian determinant of the linearised moisture flux (10^{-8} s^{-1}, filled contours) and the cyclone-relative moisture flux (kg m^{-1} s^{-1}, vectors) on the 285 K isentrope for each data-set I_1 to I_4 (top to bottom) at T-24, T+0 and T+24 hours relative to maximum intensity (left to right).

feeder airstream, and therefore the direction of moisture transport, is not affected by the intensity of the cyclone, or the stage of the cyclone life-cycle. However, the strength of the feeder airstream, and therefore the strength of the atmospheric river, is affected by the intensity of the cyclone and the stage of the cyclone life-cycle.

Nevertheless, this could be a result of the seeder-feeder and atmospheric river features becoming less aligned spatially. The track densities of data-sets I_1 to I_4 (not shown in this text) show that the majority of the tracks in data-set I_1 reside in the North Atlantic storm track and therefore, the storms tend to propagate in the same direction. However, as the data-sets decrease in intensity, the tracks become more spread out over the midlatitude northern hemisphere rather than just in the North Atlantic storm track. This could have an effect on the location of the feeder airstream and atmospheric river relative to the centre of the cyclone as the polar stereographic data is not rotated. Therefore, it would be beneficial to conduct an investigation into the properties of each intensity data-set.

3.2.2 The feeder airstream in composite data with decreasing propagation velocities

To investigate the direction and magnitude of moisture transport via the feeder airstream in relation to the propagation velocity of a cyclone, the composite surface, vertically integrated and isentropic fields are analysed for data-sets U_1 to U_4 and the results are shown in Figure 3.6. The fact the more intense cyclones on average propagate faster (as shown in Figure 3.2) is reflected by the central mean sea level pressure in data-sets U_1 to U_4 (figures 3.6a, d, g and j) which increases as the propagation velocity decreases. Furthermore, the presence of an atmospheric river is also dependant on the storms propagation velocity as the only data-set with IVT greater than 250 km m^{-1} s^{-1} is U_1. The IVT generally decreases as the propagation velocities of the storms decrease in the data-sets. The pressure gradient along the isentrope, specific humidity close to the surface and Earth-relative winds (figures 3.6b, e, h and k) also decrease as the propagation velocities of the storms decrease in the data-sets.

The direction of moisture flux is still from east to west across the domain in

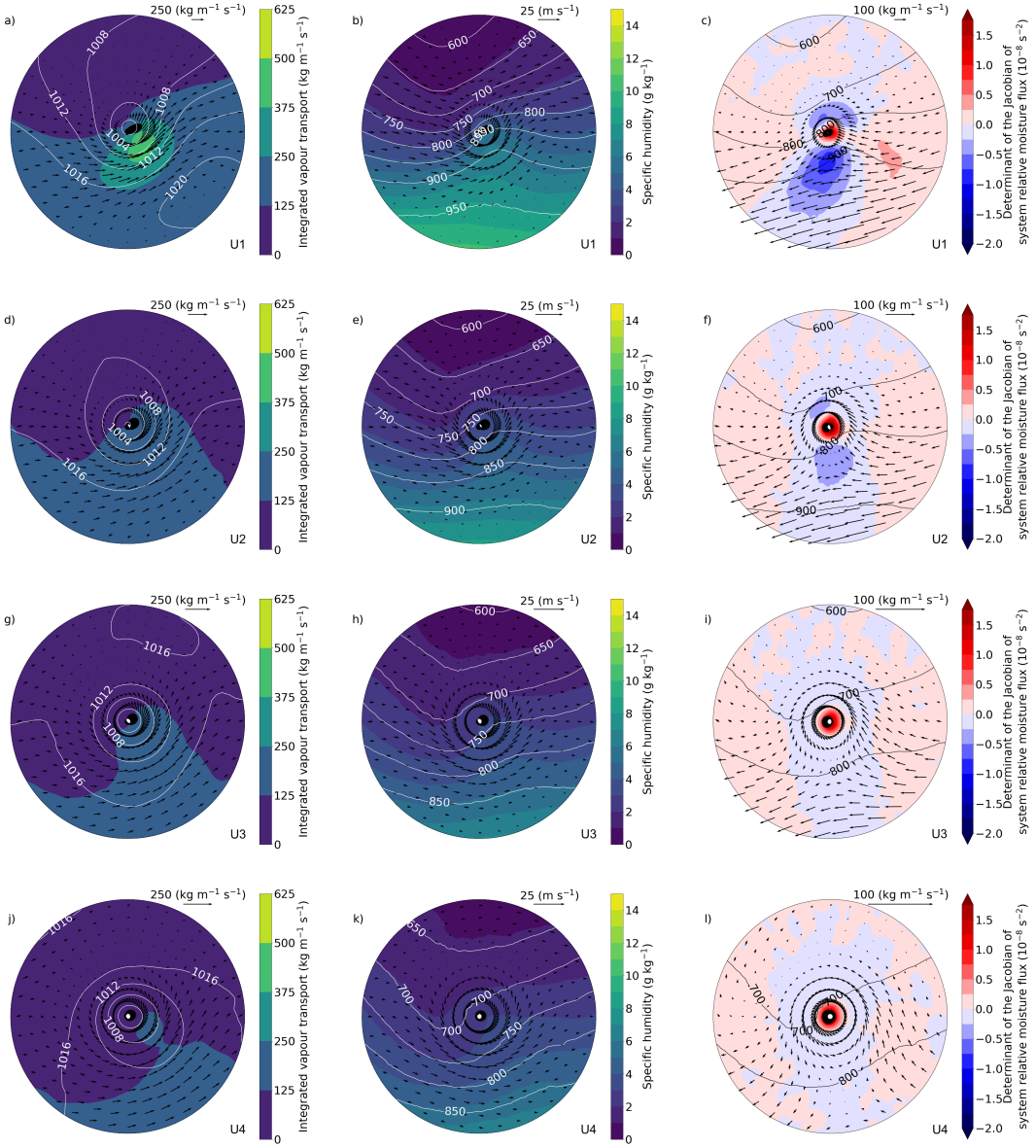

Figure 3.6: The composite data for mean sea level pressure (hPa, white contours), and IVT (kg m^{-1} s^{-1}, filled contours and vectors) for each data-set U_1 to U_4 (a, d, g, j). The composite data for pressure (hPa, white contours), specific humidity (g kg^{-1}, filled contours) and the Earth-relative winds (m s^{-1}, vectors) on the 285 K isentrope for each data-set U_1 to U_4 (b, e, h, k). The composite data for pressure (hPa, black contours), the Jacobian determinant of the linearised moisture flux (10^{-8} s^{-1}, filled contours) and the cyclone-relative moisture flux (kg m^{-1} s^{-1}, vectors) on the 285 K isentrope for each data-set U_1 to U_4 (a, d, g, j).

all data-sets, and the magnitude of the moisture flux decreases as the propagation velocity decreases (figures 3.6c, f, i and l). The atmospheric river and the saddle point associated with the feeder airstream in U_1 lies ahead of the stronger pressure gradient along the isentrope where there is higher specific humidity. This indicates that they both lie ahead of the cold front in the warm sector of the cyclone. This suggests that the presence of the feeder airstream is not determined by the propagation velocity, but the strength of the feeder airstream and the atmospheric river are. However, to understand this relationship further an investigation into the data-sets themselves is needed.

3.3 The identification algorithm

3.3.1 Introduction

As the compositing method relies on taking an average over the fields, it is difficult to ascertain how likely a feeder airstream is to occur in each data-set. It is also difficult to ascertain whether the decrease in strength of the moisture flux and IVT associated with the feeder airstream and atmospheric river is a result of these features not coinciding spatially, or whether there is a connection to intensity and propagation velocity. If the cold fronts in each cyclone do not align (perhaps because the cyclones are propagating in different directions or because the cyclone has undergone occlusion rather than frontal fracture), then the feeder airstreams and atmospheric rivers are unlikely to align either. Therefore there will be a reduction in the composite cyclone-relative moisture flux and the IVT. To overcome this, the algorithm of Cuckow et al. (2022) is adapted to identify the region associated with the saddle point created by the feeder airstream in each storm on a polar stereographic grid. This is applied to all of the data-sets (I_1 to I_4 and U_1 to U_4). By using this method, the likelihood of a feeder airstream saddle point occurring in each grid

box of the domain for each data-set can be studied.

The identification algorithm of Cuckow et al. (2022) searches for regions associated with the feeder airstream in the low-level cyclone-relative moisture flux. These regions are associated with saddle points in the cyclone-relative moisture flux field. To identify these saddle points in the moisture flux at low-levels, an absolute threshold in pressure and a relative threshold specific humidity are used to isolate a low-level region of moisture flux on an isentrope. A watershed algorithm is then used to search for regions associated with minima in this region of moisture flux. The watershed algorithm is an image segmentation tool that uses a threshold value in moisture flux to define a region associated with minima in the moisture flux field. The larger the moisture flux percentile, the larger the identified region around the minima in the moisture flux is. To limit the number of minima found, the image is first smoothed using a disk radius. At each grid point, the mean value of the field that resides within the disk is found. Therefore, the larger the disk radius, the more the image is smoothed. If the region associated with a minimum in the moisture flux coincides with an area of negative determinant, they are associated with a saddle point and therefore the feeder airstream. A list of the steps the algorithm takes are as follows.

1. Select an isentrope.

2. If all of the isentrope is above 700 hPa, move onto the next isentrope.

3. Mask points in the cyclone-relative moisture flux and the determinant above 700 hPa to select low-level flow on the isentrope.

4. Mask any points in the cyclone-relative moisture flux and the determinant that coincide with a specific humidity below the 70^{th} percentile in the region that is left unmasked by the pressure threshold. This is done to select moist airflows.

5. Mask any points in cyclone-relative moisture flux and the determinant that lie

below the surface

6. Move onto the next isentrope if more than 90 % of the domain is masked above 700 hPa.

7. Move onto the next isentrope if more than 90 % of the domain is masked above the 70$^{\text{th}}$ percentile in specific humidity

8. If more than 25 % of the domain is masked because it is below the surface, move onto the next isentrope.

9. Using the unmasked cyclone-relative moisture flux on the isentrope, search for minima below the 10 $^{\text{th}}$ percentile in the remaining cyclone-relative moisture flux using the watershed algorithm using a disk radius of 1 grid box.

10. If no minima are found, then no region associated with the feeder airstream is found. Move onto the next isentrope.

11. If minima are found, check whether they coincide with an area of negative determinant.

12. If there is more than one region associated with a saddle point in the cyclone-relative moisture flux, find the one with the largest area.

This algorithm is applied to all storms, at T-60 to T+60 hours relative to maximum intensity in 6 hourly intervals on the 265, 275, 285, 300, 310 and 320 K isentropes. A feeder airstream might be identified over multiple isentropic surfaces as the vertical extent of the feeder airstream is not isolated to one isentropic level (found through the analysis of storm Bronagh, not shown). Therefore, to ensure that one feeder airstream is identified per storm, only one isentropic surface is used in the results. Each isentropic surface is checked to see whether a feeder airstream is identified and added to the results accordingly. This process starts on the 285 K level as this has been shown to be an appropriate level for the analysis of the feeder

airstream through the analysis of the composite data. If this surface is unsuitable (for example, if this isentrope is too high in the atmosphere to identify low-level airflows), then the results on the 275 K level are used. If this surface is also unsuitable for use with the algorithm (for example if the isentrope is too low because they are located further north or intersect the ground), then the results on the 300 K isentrope are used. This process is repeated for the 265, 310 and then 320 K levels. Following this method, it is found that for some storms there are no suitable isentropes for the identification of the feeder airstream as they are either too high or too low in the atmosphere. These storms are therefore not included in the final results. As there are still more than approximately 150 storms in each data-set at T-24 and T+24, it is deemed that these times are suitable for the investigation into the likelihood of a feeder airstream saddle point occurring in the domain.

3.3.2 Development

To develop this algorithm and to choose the threshold values, the 45 most intense storms are used. The identification algorithm is run using a variety of pressure, specific humidity, disk radius, system relative moisture flux thresholds or percentiles and the fields analysed. By analysing the location of the identified regions, it is found that a pressure threshold of 700 hPa and a 70 % threshold in specific humidity in the region below 700 hPa is the most successful at identifying the low-level moist airflow associated with the feeder airstream. Using a pressure and specific humidity threshold higher than 700 hPa or 70 % resulted in the feeder airstream being identified too low in the domain as too much of the domain was masked. On the other hand, if the thresholds lower than 700 hPa or 70 % are used, regions associated with saddle points to the north-east of the cyclone centre are identified. These are not associated with the feeder airstream as they are not low-level moist air-flows.

To ascertain the best moisture flux percentile and disk radius to use when search-

ing for minima using the watershed algorithm, the hit rates for each storm with storm numbers between 1 and 50 (45 storms) at T-24 hours relative to maximum intensity are calculated. The hit rate is the fraction of observed regions associated with the feeder airstream that are correctly identified and is calculated using equation 3.1. In this equation a is the number of correctly identified regions and c is the number cyclones with a feeder airstream that are not identified. The closer to 1 that the hit rate is, the better the algorithm is at correctly identifying the feeder airstream.

$$HR = \frac{a}{a+c} \tag{3.1}$$

The false alarm rate can also be calculated using a similar approach. It is the fraction of storms without a feeder airstream that are identified correctly. The false alarm rate is (I_1 and I_2) shown in equation 3.2 where b is the number of storms without a feeder airstream that were identified as having a region associated with the feeder airstream (false alarm) and d is the number of storms that do not have a feeder airstream that were correctly identified. The closer to 0, the better the algorithm is at correctly identifying storms that do not have a feeder airstream.

$$FAR = \frac{b}{b+d} \tag{3.2}$$

To ascertain which cyclones have a feeder airstream, the fields are analysed manually (by the author). Any storm that has a minimum in moisture flux that lies at low-levels, corresponding with cyclone-relative winds that travels across the domain from east to west with an anticyclonic turning branch, is deemed to have a feeder airstream (note that the fields are analysed on the 285 K isentrope after any data points that intersect the ground are removed). Any storm that has cyclone-relative winds approach the cyclone centre from any other direction is deemed to not have a feeder airstream. An example of a storm that has and does not have a feeder airstream is shown in Figures 3.7a and b. An example of when the presence of

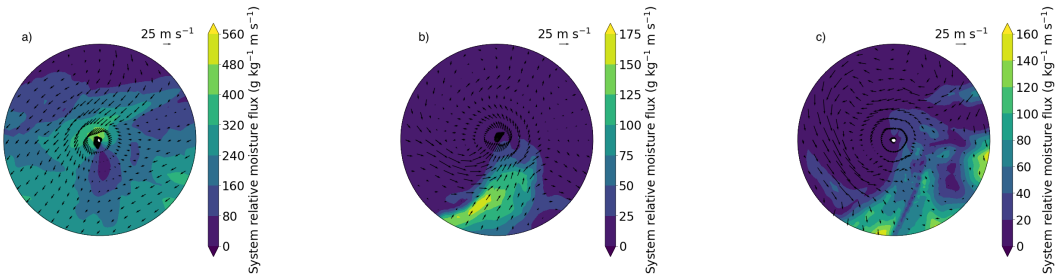

Figure 3.7: Example of a storm with a feeder airstream (a), without a feeder airstream (b) and a storm where the presence of the feeder airstream is ambiguous (c) determined using the cyclone-relative moisture flux (kg m^{-1} s^{-1}, filled contours) and cyclone-relative winds (m s^{-1}, vectors).

the feeder airstream is ambiguous is shown in Figure 3.7c. In this case, it is deemed that there is a feeder airstream, as the flow has an anticyclonic turning branch that lies ahead of a minimum in cyclone-relative moisture flux.

By manually identifying the feeder airstream in each storm, the percentage of storms with a saddle point could be found. It is found that 96 % of storms had a feeder airstream. As only 2 out of the 45 storms analysed do not have a feeder airstream, the false alarm rates for this data-set is not analysed.

The identification algorithm is run with cyclone-relative moisture flux percentiles at 1, 5, 10 and 15 % and disk radii of 1, 2, 3 and 5 grid points using a pressure threshold of 700 hPa and a specific humidity percentile of 70 % on the 285 K isentrope. The hit rates for each run are shown in Figure 3.8. As shown in this Figure, the threshold values that resulted in the highest hit rates, and therefore more successfully identified the feeder airstream, is a cyclone-relative moisture flux percentile of 5 with a disk radius of 1, a cyclone-relative moisture flux percentile of 10 %, with a disk radius of 1 grid point or a cyclone-relative moisture flux percentile of 15 %, with a disk radius of 1 or 2 grid points. Therefore, a cyclone-relative moisture flux percentile of 10 %, with a disk radius of 1 grid point is used in this study.

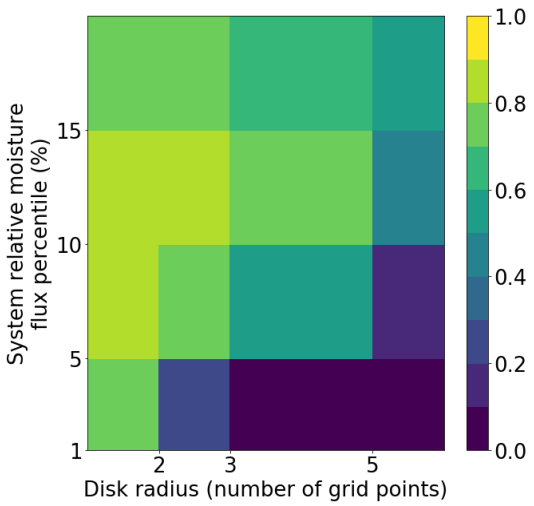

Figure 3.8: The hit rates in parameter space for the 45 most intense storms. Found using the fields that are analysed manually (by the author) and by running the identification algorithm with a pressure threshold of 700 hPa, a specific humidity percentile of 70 %, and cyclone-relative moisture flux percentiles of 1, 5, 10 and 15 % and disk radii of 1, 2, 3 and 5 grid points. Note, the numbers on the x and y axis correspond the the box to the right and above respectively.

3.3.3 Testing

To ensure that the identification algorithm works with weaker storms, not just the most intense ones, the hit rates and false alarm rates are calculated for storms with a storm number between 250 - 300, 500 - 550, 750 - 800 and 950 - 1000 at T-24 hours using a cyclone-relative moisture flux percentile of 10 %, a disk radius of 1, a pressure threshold of 700 hPa and a specific humidity percentile of 70 % on the 285 K isentrope. It is found that the percentage of storms that had a feeder airstream (identified manually) decreased with intensity. This suggests that the presence of the feeder airstream does depend on the intensity of the storm. However, it is also found that the hit rates for storms with a storm number between 250 - 300, 500 - 550, 750 - 800 and 950 - 1000 all had a value of 1. This is a result of the majority of the storms being identified as having a feeder airstream in each data-set regardless

of whether one was identified manually. This means that regions associated with saddle points that are not related to the feeder airstream are identified. Therefore, it is possible to identify a saddle point satisfying the criteria by chance elsewhere in the domain.

To overcome this, the probability density and probability background density of saddle points (rather than the region associated with the saddle points) are calculated for all data-sets (I_1 to I_4 and U_1 to U_4). To find the location of each saddle point, the mean radius and azimuth of each region associated with the saddle points are found. The density is calculated by counting the number of saddle points that lie in a grid box of the polar steriographic domain. The grid boxes are defined by dividing the domain into azimuths of 45 ° intervals and radial intervals of 2.17 °. Therefore the grid boxes will have different sizes depending on their radii. To account for this, the number of saddle points within a grid box is divided by the area of the grid box. As this study also uses data-sets of different sizes, the number of saddle points is also divided by the total number of storms in each data-set. The saddle calculation of the saddle point probability density in each grid box is shown in equation 3.3 where $\rho_{sp}^{r,\theta}$ is the saddle point probability density, $n^{r,\theta}$ is the number of saddle points in a grid box, $A^{r,\theta}$ is the area of the grid box, N_s^d is the number of storms or time-steps in the data-set, r refers to the radius and θ the azimuth of the grid box.

$$\rho_{sp}^{r,\theta} = \frac{n^{r,\theta}}{A^{r,\theta} N_s^d} \tag{3.3}$$

The background probability density is shown in equation 3.4 where n is the number of saddle points, A is the area of the whole domain and N_s^d is the number of storm time-steps in the data-set (calculated using all 12522 storm time-steps).

$$\rho_{bg} = \frac{n}{A N_s^d} \tag{3.4}$$

To calculate whether a grid box is more or less likely to contain a feeder airstream saddle point than the background (and how many times more likely that a feeder airstream saddle point is to occur relative to the background) in each grid box, the saddle point density is divided by the background density. This is shown in equation 3.5 where L is the likelihood ratio. If the likelihood ratio is greater than 1, then a feeder airstream is more likely to appear than the background in that grid box.

$$L^{r,\theta} = \frac{\rho_{sp}^{r,\theta}}{\rho_{bg}} \tag{3.5}$$

3.4 The likelihood of the feeder airstream occurring in the domain for storms with decreasing intensities

The likelihood of the feeder airstream saddle point occurring in the domain for I_1 to I_4 (top to bottom) are shown for T-24, T+0 and T+24 hours relative to maximum intensity (left to right) in Figure 3.9. A feeder airstream saddle point is more likely to occur than background for all data-sets at all times relative to maximum as the likelihood ratio is greater than 1 in the domain. The maximum likelihood in each domain for these data-sets coincides with the feeder airstreams identified in the composites. This demonstrates that the feeder airstream saddle points are successfully identified. Analysing the maximum likelihood in each domain, it can be seen that a feeder airstream is most likely to occur (30 times more likely than background) in the area directly south of the cyclone centre in the most intense storms (storms in the I_1 data-set) at T-24. As the intensity of the storms decrease, so does the maximum likelihood in each domain of a feeder airstream saddle point occurring south of the cyclone centres for data-sets I_1 to I_4 at T-24. Additionally, as the storms reach maximum intensity and begin their decay, the likelihood of a feeder airstream saddle point occurring also decreases.

It is unclear whether the decrease in the maximum likelihood in each domain is due to the decrease in intensity, the change in life-cycle, or whether it is due to the identified feeder airstream saddle points becoming less aligned. For example, in I_1 at T-24 (figure 3.9a), the area of increased likelihood of a feeder airstream saddle point occurring in the domain (where the likelihood ratio is greater than 1) is concentrated in the area south of the cyclone centre. This suggests that the feeder airstreams in the data-set are well aligned. However, as the storms reach maximum intensity and begin to decay (I_1 at T+0 and T+24, Figures 3.9b and c), the area of increased likelihood of a feeder airstream saddle point occurring in the domain becomes more spread out, suggesting that the feeder airstreams become less aligned at these times. This makes it difficult to ascertain whether the likelihood of a feeder airstream occurring in the domain or the strength of the moisture flux associated with the feeder airstream is related to the cyclone's life-cycle or not. A similar pattern is also shown as the storms decrease in intensity (e.g. Figures 3.9a, d, g to j). Therefore, it is also difficult to ascertain whether the likelihood of a feeder airstream occurring or whether the strength of the moisture flux associated with the feeder airstream is related to the intensity or not.

3.5 The likelihood of the feeder airstream occurring in the domain for storms with decreasing propagation velocities

The likelihood of a feeder airstream saddle point occurring in the domain for data-sets U_1 to U_4 are shown in Figure 3.10. By analysing the maximum likelihood in each domain, it can be seen that a feeder airstream is most likely to occur (21 times more likely than background) in the fastest moving storms (in the U_1 data-set) in comparison to slower moving ones. The maximum likelihood in each domain

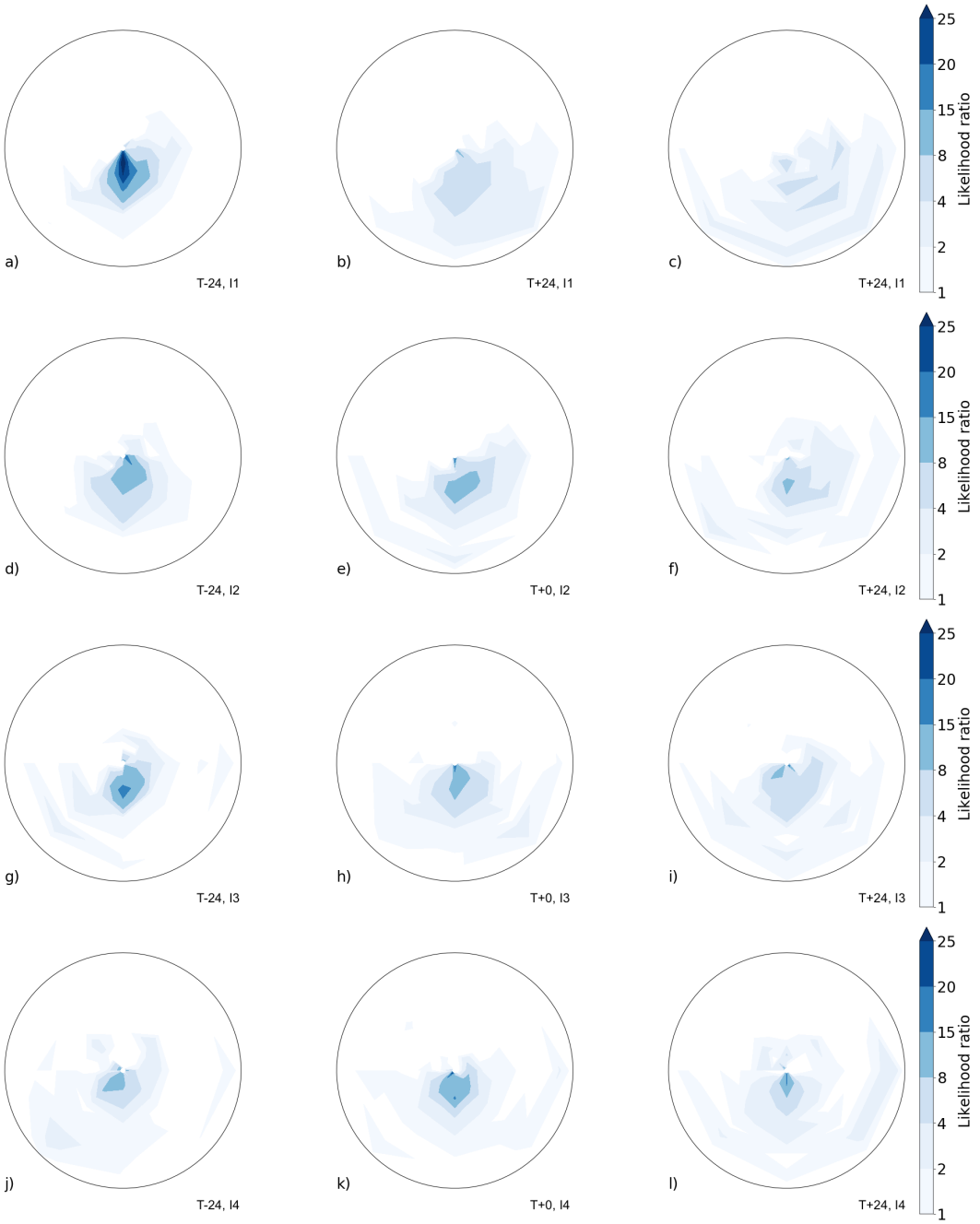

Figure 3.9: The likelihood of a feeder airstream saddle point occurring relative to background for data-sets I_1 to I_4 (top to bottom) at T-24, T+0 and T+24 hours relative to maximum intensity (left to right).

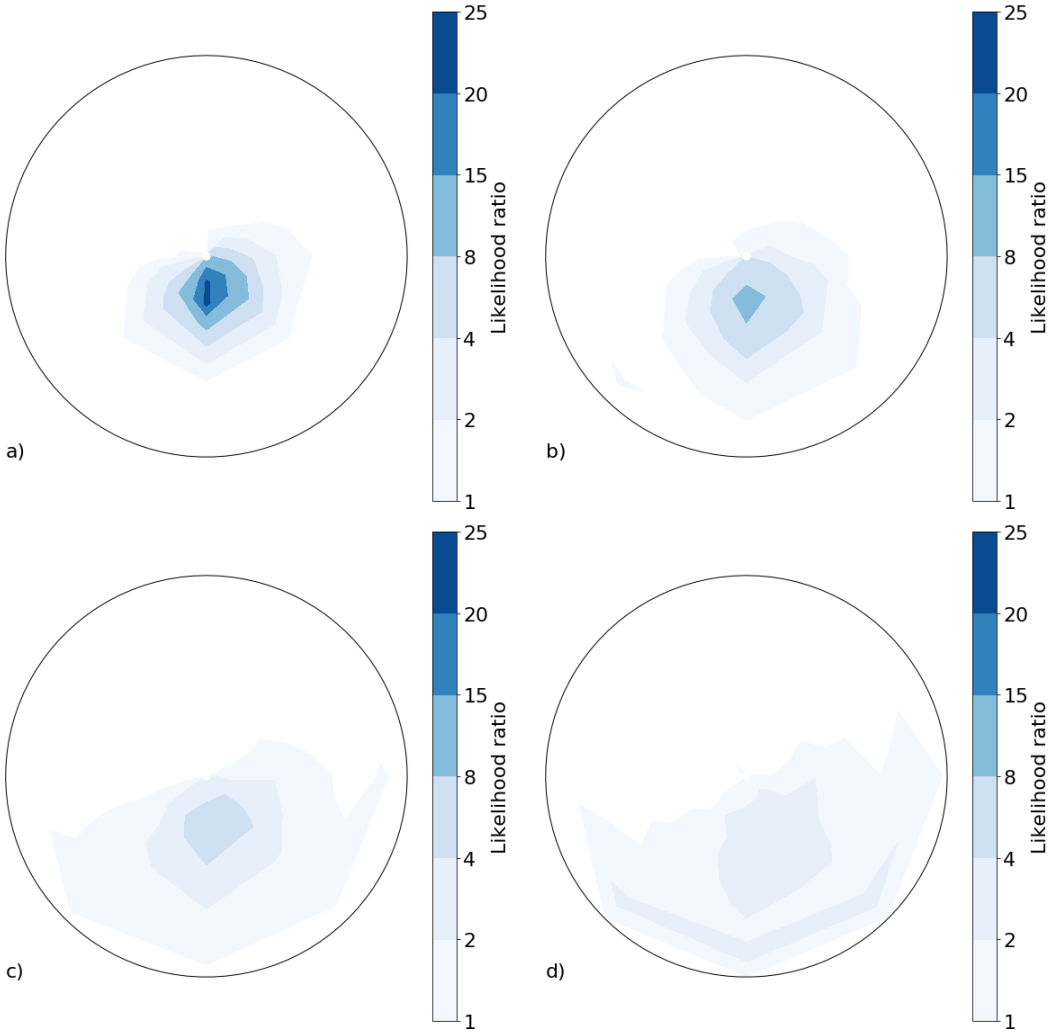

Figure 3.10: The likelihood of a feeder airstream saddle point occurring relative to background U_1 (a), U_2 (b), U_3 (c) and U_4 (d)

decreases as the propagation velocity decreases. However, similarly to the likelihood of a feeder airstream saddle point occurring in the intensity data-sets, the area of increased likelihood (where the likelihood ratio is greater than 1) becomes larger as the storms slow down. Therefore, it is difficult to ascertain whether the likelihood of a feeder airstream occurring or the strength of the moisture flux associated with the feeder airstream is related to the propagation velocity or not.

3.6 Conclusions

In this chapter, an investigation into the direction of moisture transport in midlatitude, northern hemisphere extratropical cyclones is conducted. This is done using data-sets that have intense, moderately intense, moderately weak and weak storms in them (I_1 to I_4). It is also done using data-sets that have fast, moderately fast, moderately slow and slow moving (in terms of propagation velocity) storms in them (U_1 to U_4). Firstly, the composite fields of each data-set is analysed to see whether a feeder airstream is present. Secondly, the identification diagnostic is applied to each storm at each time-step in the data-sets to ascertain when a feeder airstream is most likely to occur and whether this relies on the intensity, propagation velocity or life-cycle of the cyclone.

By analysing the composite data of the I_1 to I_4 data-sets, it is found that the presence of the feeder airstream, and therefore the direction of moisture transport, is not affected by the intensity of the cyclone, or the stage of the cyclone life-cycle. However, the strength of the feeder airstream, and therefore the strength of the atmospheric river, is affected by the intensity of the cyclone and the stage of the cyclone life-cycle. Similarly, through analysis of the composite data of the U_1 to U_4 data-sets, the presence of the feeder airstream is not determined by the propagation velocity, but the strength of the feeder airstream and the atmospheric river are. However, to understand these relationships further, an investigation into the data-sets themselves is needed (for example, to ascertain the spread of data in each data-set).

Through the application of the identification diagnostic to the data-sets, it is found that the likelihood of a feeder airstream occurring south of the cyclone centre decreases as the intensity and propagation velocity of the storm decreases. The likelihood also decreases as the storms reach maximum intensity and begin to decay. However, it is unclear whether the decrease in likelihood is due to the identified

feeder airstream saddle points becoming less aligned. This is because the the area of increased likelihood (where the likelihood ratio is greater than 1) becomes larger as the storms become less intense, decay and slow down.

The investigation into the composite data suggests that the majority of storms have a feeder airstream and therefore, transport moisture from the environment ahead of the cyclone. However, it is unclear precisely how many storms have a feeder airstream in each data-set. The likelihood ratios indicate that the data-sets with fast moving, intense developing storms will have more storms with a feeder airstream than the data-sets with slow moving, weak decaying storms. This suggests that moisture in the environment ahead of the cyclone plays an important role in the formation of precipitation. Particularly in fast moving, intense developing storms. Therefore, this work supports the findings of Dacre et al. (2019), Papritz et al. (2021) and the ERICA IOP 4 case study.

However, further investigation is needed to ascertain exactly how many of the storms have a feeder airstream and under what conditions this arises. Whilst this study shows that the propagation velocity and intensity have a part to play, there may be other factors that affect whether a feeder airstream is present. This would give further insight into the importance of moisture transport from ahead of the cyclone in the production of precipitation and the resulting impacts.

CHAPTER

FOUR

MECHANISMS CONTRIBUTING TO THE FORMATION OF PRECIPITATION OVER THE UK

While the previous two chapters focused on the synoptic scale moisture transport that leads to precipitation, precipitation can also be formed via micro-scale mechanisms. Therefore, the aim of this chapter is to investigate the synoptic scale and mirco-scale formation of precipitation by finding the relative contributions of rainfall produced via ascent in the warm conveyor belt (cyclone ascent) and by orographic enhancement (via orographic ascent and the seeder-feeder mechanism) to the precipitation produced by storm Bronagh. To do so, three experiments are run using the MetUM. By comparing the accumulated rainfall produced by each experiment over elevated orography in Wales, the amount that each process contributes to the overall rainfall is found.

4.1 Data

4.1.1 UKA4g limited area model

To ascertain the importance of each mechanism to the overall precipitation associated with storm Bronagh, the MetUM is used. The three experiments are conducted

using the atmosphere only configuration of the limited area numerical weather prediction model, the UKA4g. The UKA4g model uses the regional UKV configuration of the MetUM and is implemented using the MetUM code at version 11.1. The UKV and UKA4g models are high resolution atmospheric models that have a domain centered around the UK and are nested within the global model (approximately $(17\ \text{km})^2$ resolution). The resolution within the UKA4g model is 1.5 km x 1.5 km in the inner regions and 4 km x 4 km around the edges of the domain. The UKA4g domain lies between approximately 46 °N to 63 °N and 19 °W – 13 °E (Valiente et al., 2021). Using a high resolution model is beneficial as micro-scale processes can be simulated without the need of parameterisation. Furthermore, this model is convection permitting as the grid box spacing is 1.5 km. There are 70 hybrid height vertical coordinates with a model top at approximately 40 km (Lewis et al., 2019; Gentile et al., 2021a). The coordinate system is terrain following near the surface and becomes flat at approximately 30 km. The height of the terrain, or surface height, refers to the height of the orography above mean sea level. The model level height refers to the hybrid height coordinate system. The altitude refers to the height above sea level.

To investigate the precipitation associated with storm Bronagh, the UKA4g model is run with a lead time of 24 hours (start time of 0000 UTC 19 September 2018) and the large scale rain amount is investigated. This is the mass per meter squared of rainfall (produced by the large scale precipitation parameterisation scheme) that falls on the surface per time-step.

4.1.2 Large scale precipitation parameterisation scheme

To isolate each precipitation formation mechanism within the UKA4g model, the accretion and riming parameterisation schemes are modified. These are part of the large scale precipitation parameterisation scheme, often called the microphysics

scheme. This scheme is based on that developed by Wilson and Ballard (1999) and models the processes that result in a phase change from one form of water to another. This microphysics scheme is a one moment scheme that models the following hydrometer species: rain, liquid cloud, ice aggregates, ice crystals and graupel. It parameterises processes such as aggregation, riming, accretion and autoconversion and includes a sub grid-scale model for the vapour, liquid, ice and rain contents.

The accretion scheme converts cloud liquid water to rain and is the rate that liquid cloud is collected by rain as a result of collision and coalescence. The riming scheme is similar to the accretion scheme, however it converts cloud liquid water to ice rather than cloud liquid water to rain. Ice particles collide with, and collect cloud droplets which freeze on impact. The riming scheme only acts when the temperature is below the melting level (0 °C). Note, accretion can also act at temperatures below the melting level due to the presence of supercooled cloud droplets.

4.1.3 Representation of the micro-scale and synoptic scale formation of precipitation in the UKA4g model

It has been shown in Smith et al. (2015) that to accurately forecast mean rainfall patterns associated with orographic rain enhancement, a 1.5 km horizontal grid spacing (or smaller) is needed to resolve the orography. Therefore, to confirm that the UKA4g model aptly captures the rainfall associated with storm Bronagh, a comparison between the HadUK-Grid daily total rainfall amount (data interpolated from meteorological station data onto a uniform grid) from the Met Office and the accumulated rainfall from the UKA4g model is made. The accumulated rainfall from the UKA4g model is found using the large scale rain amount.

The comparison between the HadUK-Grid total rainfall amount and the accumulated rainfall produced by the UKA4g model is shown in Figure 4.1. In both data-sets, the rainfall is shown to have fallen over Wales, the Midlands and northern

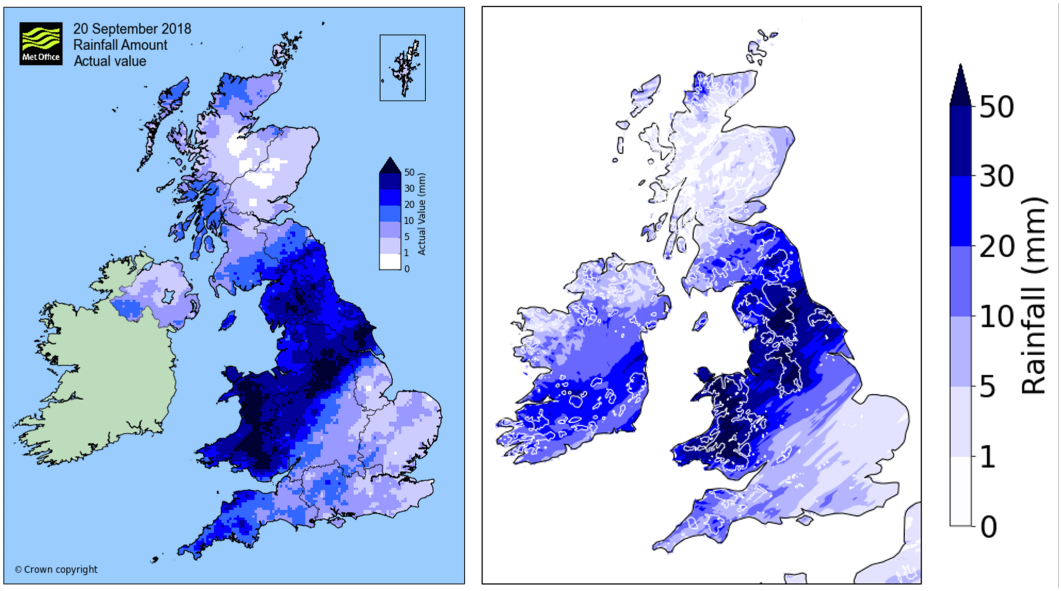

Figure 4.1: Total accumulated rainfall amount from 0900 UTC 20 to 0900 UTC 21 September 2018 for (a) HadUK-Grid (Contains public sector information licensed under the Open Government Licence v3.0), (b) UKA4g model.

England as the cyclone has tracked over the UK. The HadUK-Grid rainfall amount measured greater than 50 mm of rainfall over Wales and parts of England, where there is elevated orography. For example, over the Pennines, Yorkshire Dales and the Peak district. This is successfully captured by the UKA4g model as greater than 50 mm of rainfall is also produced in these areas. This suggests that the grid size used in the UKA4g model is small enough to resolve the orography enough to capture orographic rain enhancement. Note, as 1.5 km horizontal grid spacing is used, any convection associated with ascent in the warm conveyor belt and orographic ascent is included in the contributions to the overall precipitation.

To ensure that that the large scale features such as the atmospheric river, are captured by the UKA4g model, a comparison between the IVT produced by the ERA5 data-set and the UKA4g model is made. This is shown in Figure 4.2 where the IVT from the UKA4g model is on the left and the IVT from ERA5 on the right. As shown in this Figure, a filament of high IVT extends over England and the North

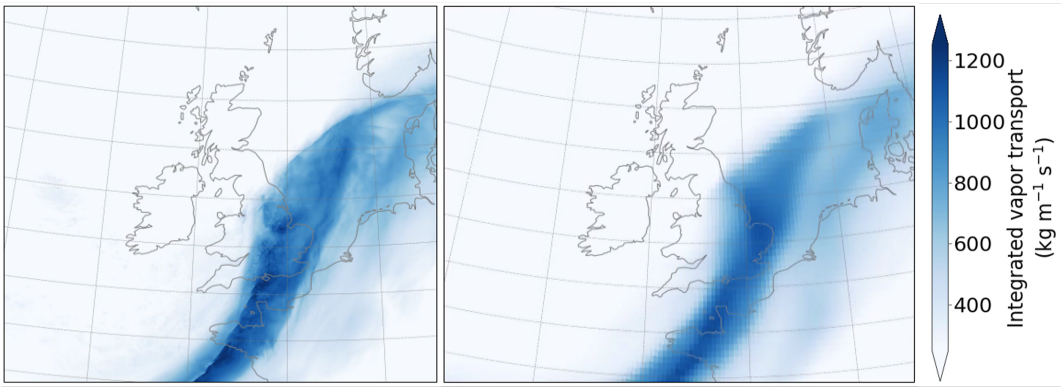

Figure 4.2: Vertically integrated vapour transport at 0000 UTC on 21 September 2018 produced by the UKA4g model in (a) and the ERA5 reanalysis data-set in (b).

Sea in both the ERA5 data-set and the UKA4g model. Whilst the UKA4g model captures more detail, the large scale features in the ERA5 data-set and the UKA4g model are well captured. Therefore, as both the small scale and large scale features are captured well by the UKA4g model, it is suitable for use in this study.

4.1.4 Storm Bronagh in the UKA4g model

To ascertain when the precipitation associated with this storm is produced, the hourly precipitation and mean sea level pressure is plotted at various stages of Bronagh's passage through the UKA4g domain (Figure 4.3). As shown in Figure 4.3a and b, Storm Bronagh intensified from 1008 hPa on 2100 UTC 20 September to 966 hPa on 1800 UTC on 22 September as it tracked Eastwards over the North Atlantic, over the UK and into the North Sea. At 0600 UTC 20 September Bronagh is centred over the North Atlantic on the left hand side of the UKA4g domain. At this time there is some rainfall associated with the frontal wave that Bronagh develops from. This rainfall is situated over the North Atlantic, Wales and England (Figure 4.3a). As the storm develops and tracks Eastwards over the UK, it brings further rainfall

to Wales and England until it tracks into the North sea (Figures 4.3b, c and d).

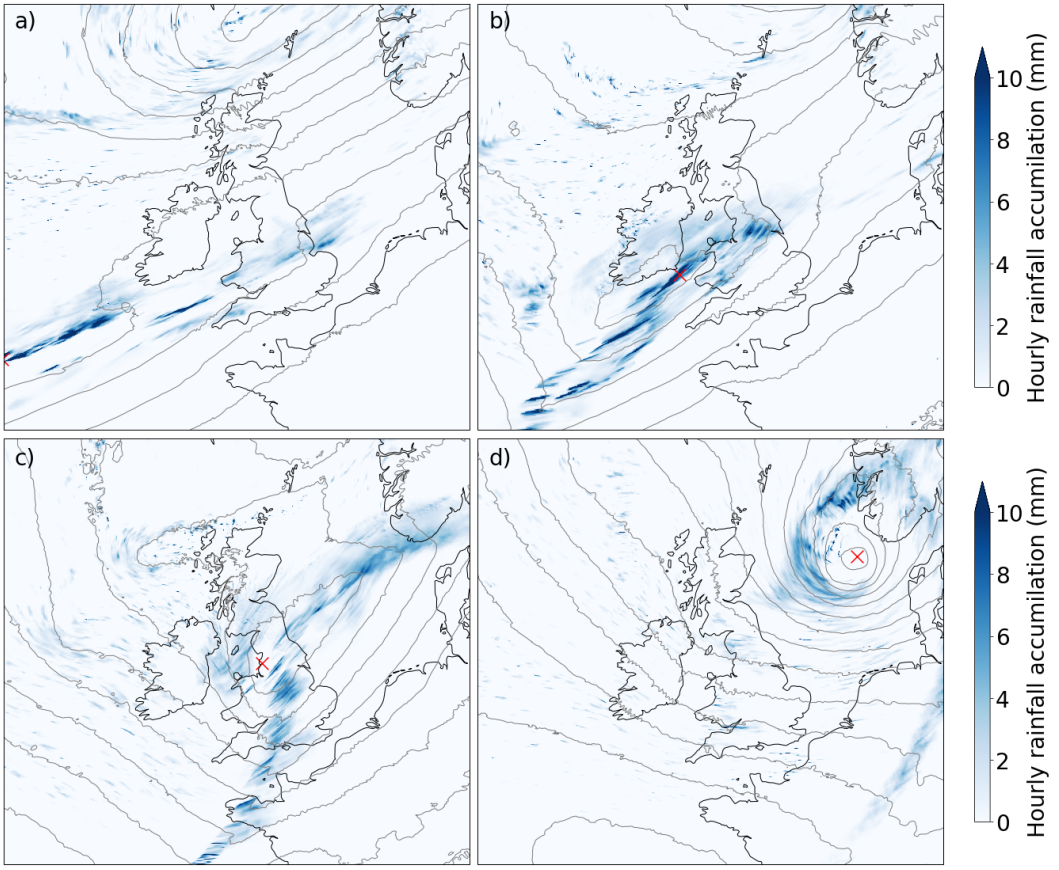

Figure 4.3: Mean sea level pressure at (a) 0600 UTC 20 September, (b) 1500 UTC 20 September, (c) 0000 UTC 21 September and (d) 1200 UTC 21 September, and the hourly accumulated rainfall between (a) 0500-0600 UTC 20 September, (b) 1400-1500 UTC 20 September, (c) 2300 UTC 20 September-0000 UTC 21 September and (d) 1100-1200 UTC 21 September produced by the UKA4g model with no alterations. The red cross marks the centre of the storm at each time-step.

4.2 Method

4.2.1 Experimental design

The three experiments used to calculate the contribution of each mechanism to the overall precipitation are outlined in table 4.1 and Figure 4.4. The first experiment (CTRL in table 4.1) is a control experiment in which all synoptic scale and

micro-scale mechanisms remain unchanged within the model domain. Therefore, in this experiment, precipitation formed via cyclone ascent (in the warm conveyor belt, along fronts, and the associated convection), orographic ascent (including enhancement via convection) and low-level accretion and riming (associated with the seeder-feeder mechanism) is produced. The mechanisms present in the CTRL experiment are illustrated in Figure 4.4a where there is cyclone related precipitation (smaller raindrops) falling through a low-level feeder cloud. This low-level cloud is produced via orographic ascent (shown by the black arrows labelled orographic ascent) and precipitation is enhanced via low-level accretion and riming in the feeder cloud located above the elevated orography (labelled seeder-feeder and shown via the larger raindrops). The mechanisms that are contributing to the overall precipitation produced by the CTRL experiment are shown in equation 4.1. In this equation E^{CTRL} denotes the accumulated rainfall produced by this experiment and, a_c, a_{oa} and a_{ar} denotes the accumulated rainfall formed via cyclone ascent, orographic ascent and low-level accretion and riming. As all three processes are present, the sum of a_c, a_{oa} and a_{ar} equals the total precipitation.

$$E^{CTRL} = a_c + a_{oa} + a_{ar} \tag{4.1}$$

The second set of experiments (NOACC1 to NOACC4 in table 4.1), involves turning the accretion and riming schemes off below various altitudes (height above mean sea level) where the surface height (height of surface above mean sea level) is greater than 200 m. This will limit accretion and riming in the feeder cloud and thus, limit the enhancement of precipitation via the seeder-feeder mechanism. This leaves the precipitation formed via cyclone related and orographic ascent as shown in 4.4b where the region in which accretion and riming is switched off is illustrated by the grey shaded box and the lack of enhancement of rainfall via accretion and riming is shown by the lack of larger raindrops. Only the feeder cloud is within

Table 4.1: Table outlining the experiments performed through the modification of orography, accretion and riming within the UKA4g model.

Experiment	**Orography**	**Accretion and riming schemes**	**Mechanisms present**
CTRL	Unmodified	Unmodified	Cyclone ascent, orographic ascent and the seeder-feeder mechanism
NOACC1, NOACC2, NOACC2.5, NOACC3, NOACC4, NOACC3$_{all}$	Unmodified	Off below an altitude of 1, 2, 2.5, 3 and 4 km where the surface height is greater than 200 m and, off below an altitude of 3km over the whole domain (NOACC3$_{all}$)	Cyclone and orographic ascent
FLAT	Flattened	Unmodified	Cyclone ascent

the shaded region leaving the accretion and riming on in the cyclone related cloud, over flat land and over the ocean. Experiment NOACC3$_{all}$, also listed in table 4.1, involves turning the accretion and riming schemes off below 3 km over the whole of the domain rather than just where the surface height is greater than 200 m. This experiment is included as an example of when changing the microphysics in the model alters the track of the storm. The rainfall produced by these experiments, as shown in equation 4.2 (where E^{NOACC} denotes the accumulated rainfall formed by this experiment), is the sum of a_c and a_{oa} only.

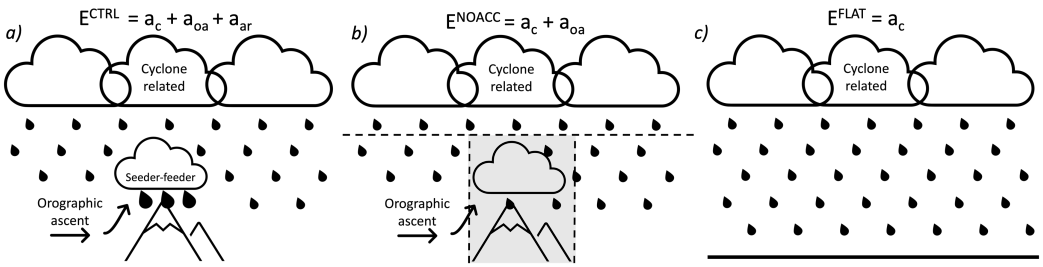

Figure 4.4: Schematics of the mechanisms present in each experiment conducted. (a) illustrates the precipitation produced by the CTRL experiment, (b) illustrates the precipitation produced by the NOACC experiment and (c) illustrates the precipitation produced by the FLAT experiment. In (b) the grey shading denotes the area where accretion and riming schemes are switched off, the horizontal dashed line represents the altitude that the schemes are switched off and the vertical dashed lines represents the surface height above which the schemes are switched off.

$$E^{NOACC} = a_c + a_{oa} \tag{4.2}$$

Whilst Figure 4.4b illustrates an ideal scenario, in reality, there is no clear separation between the low-level feeder cloud produced via orographic ascent and the seeder cloud produced via cyclone ascent. Therefore, the altitude that accretion and riming is switched off is varied.

The third experiment (FLAT in table 4.1), involves flattening the orography (setting the surface elevation to zero) in the model to stop the formation of cloud via orographic ascent. As this cloud does not form, there is also no enhancement of precipitation via the seeder-feeder mechanism in this experiment. Therefore, there is only precipitation formed via cyclone ascent. This is shown in Figure 4.4c, where there is only cyclone related rainfall (smaller raindrops) and flat orography (black line at the bottom). As only cyclone related precipitation is present in this experiment, the rainfall produced by this experiment is equal to a_c as shown in equation

4.3 where E^{FLAT} denotes the accumulated rainfall formed by this experiment. Note that in this experiment the accretion and riming schemes remain unchanged so that these processes can still occur to form precipitation in the cyclone cloud.

$$E^{FLAT} = a_c \tag{4.3}$$

The contribution of each mechanism to the overall precipitation is quantified using equations 4.4, 4.5 and 4.6. Equation 4.4 gives the contribution from cyclone related precipitation which comes from the FLAT experiment as no orography is present. The contribution from the orographic ascent is found by subtracting the accumulated rainfall in the FLAT experiment from the NOACC experiment. This is because the NOACC experiment has both cyclone and orographic ascent present, whereas the FLAT experiment has cyclone ascent only. The contribution from low-level accretion and riming is found by subtracting the accumulated rainfall from the NOACC experiment from the CTRL experiment (equation 4.6). The CTRL experiment has all three processes present, whereas the NOACC experiment has only cyclone and orographic ascent present. To ascertain how much of the precipitation is due to orographic enhancement (rainfall produced via orographic ascent, orographic convection and the seeder-feeder mechanism), the precipitation in the FLAT experiment is subtracted from the CTRL experiment as shown in equation 4.7.

$$a_c = E^{FLAT} \tag{4.4}$$

$$a_{oa} = E^{NOACC} - E^{FLAT} \tag{4.5}$$

$$a_{ar} = E^{CTRL} - E^{NOACC} \tag{4.6}$$

$$\begin{aligned} a_{oe} &= a_{oa} + a_{ar} \\ &= E^{CTRL} - E^{FLAT} \end{aligned} \tag{4.7}$$

4.2.2 Limiting changes to the cyclone dynamics

Changing the accretion and riming schemes, and flattening the orography can change the large scale dynamics of the storm. Therefore, to make a comparison between the experiments and quantify the contribution of each mechanism, the changes in large scale dynamics caused by altering the microphysics must be limited.

To ensure that changing the microphysics and flattening the orography within the UKA4g model did not change the track and intensity of the storm significantly, the track and intensity are analysed for each experiment. These are identified by finding the minimum in mean sea level pressure in 3-hourly increments for 45 hours starting at 0600 UTC 20 September 2018. This is done in the lower half of the domain (between approximately 46 N to 54.5 N) on the 20$^{\text{th}}$ September (up to 24 hours since 0000 UTC 20 September) and over the whole domain on the 21$^{\text{st}}$ (24 to 45 hours since 0000 UTC 20 September) so that the low pressure centre of the preceding storm (storm Ali) is not identified. The results are shown in Figures 4.5a and 4.5b for four experiments: CTRL, FLAT, NOACC3$_{all}$ and NOACC3. Figure 4.5a marks the track of the storm in each experiment found using the minimum mean sea level pressure. Figure 4.5b quantifies the changes in the minimum mean sea level pressure over time, therefore describing the evolution of the storm.

To investigate changes to the position of the track of the storm, the positions of the track in each experiment are examined over the North Atlantic as this is upstream of the orography in the domain. As shown in Figure 4.5a, the track of the storm in the NOACC3$_{all}$ experiment differs over the North Atlantic in comparison to the track in the CTRL, FLAT and NOACC3 experiments. The changes in the position of the track can be attributed to accretion and riming being switched off in the

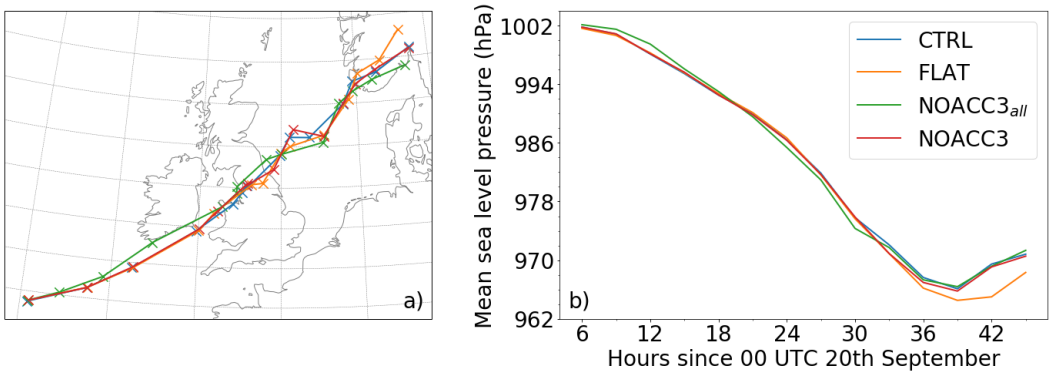

Figure 4.5: (a) Track of storm Bronagh produced by different experiments conducted using the UKA4g model. Marked by finding the minimum in 3 hourly mean sea level pressure. (b) Intensity of storm Bronagh calculated using hourly mean sea level pressure (hPa) for different experiments conducted using the UKA4g model.

cyclone related cloud as well as in any low-level cloud, altering the dynamics. If this is done over the whole domain, the dynamics will be altered further. Therefore, the accretion and riming schemes are only switched off below various low-level altitudes where the surface height is greater than 200 m.

To choose the surface height, the accumulated rainfall over a 48 hour period (from 0000 UTC 20 September to 0000 UTC 22 September) produced by orographic enhancement of rainfall, a_{oe}, is analysed. Using an accumulated rainfall over a longer period of time is advantageous as it highlights the precipitation produced via orographic enhancement. This is because the non-orographic variations in precipitation will be averaged out. This enhancement, and the accumulated rainfall produced by all three processes are shown in Figures 4.6 and 4.7. As shown in Figure 4.6, the accumulated rainfall from all three processes coincides with the track of the storm, which tracks eastwards over the UK. Over the North Atlantic and North Sea, the accumulated rainfall reaches values up to 100 mm over 48 hours. However, the accumulated rainfall of greater than 100 mm over the Pennines, Yorkshire Dales, the Peak district and over Scandinavia in Figure 4.7a indicate that the rainfall in these

areas is produced by the presence of elevated orography.

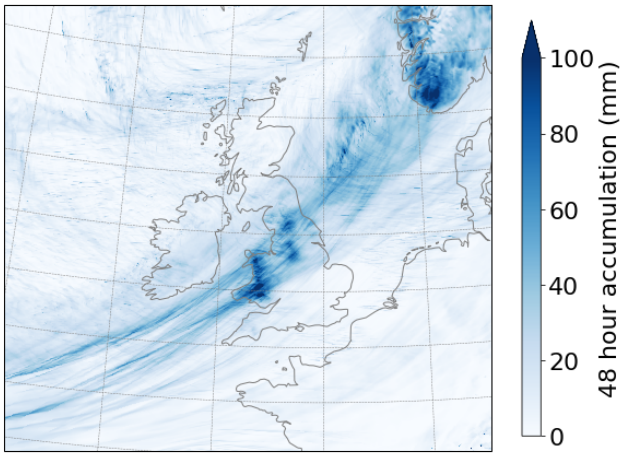

Figure 4.6: The accumulated rainfall over a 48 hour period in the UKA4g domain produced via all three processes: cyclone ascent, orographic ascent and the seeder-feeder mechanism.

This conclusion is supported by the results in Figures 4.7a and 4.7b which are produced using equation 4.7. Positive values in these Figures represent the rainfall produced by orographic enhancement and negative values represent areas where there is more rainfall produced by the FLAT experiment than the CTRL experiment. The positive values seen over Wales and England reside in the same locations where the surface height is greater than 200 m (shown by the black contour in Figure 4.7b) and therefore, depict the enhancement of rainfall over orography. Therefore, the accretion and riming schemes are switched off where the surface height is greater than 200 m. This in turn limits changes to the track of the storm over the North Atlantic, as shown in Figure 4.5b where the track of the storm in the NOACC3 experiment is similar to that of the CTRL and FLAT experiments.

It is interesting to note that the enhancement of rainfall over Scandinavia, as shown in Figure 4.7a, is similar to that over Wales (approximately 50 mm) despite the surface height in this region being much larger (highest peak in Wales is Snowdon which is 1,085 m whereas the highest peak in Scandinavia is Galdhøpiggen which

is 2,469 m). This could be because Scandinavia is downstream of Wales, meaning that some of the moisture available to the cyclone has already been converted to precipitation. However, this depends on the moisture uptakes as the cyclone tracks over the North Sea as this will re-moisten the air to some extent. There are also negative values of accumulated rainfall over England downstream of Wales. This could be due to the fact that there is no rain shadow in the FLAT experiment as there is no surface elevation. Therefore, there is more moisture available to the cyclone downstream of where the elevated surface would be and therefore, more accumulated rainfall.

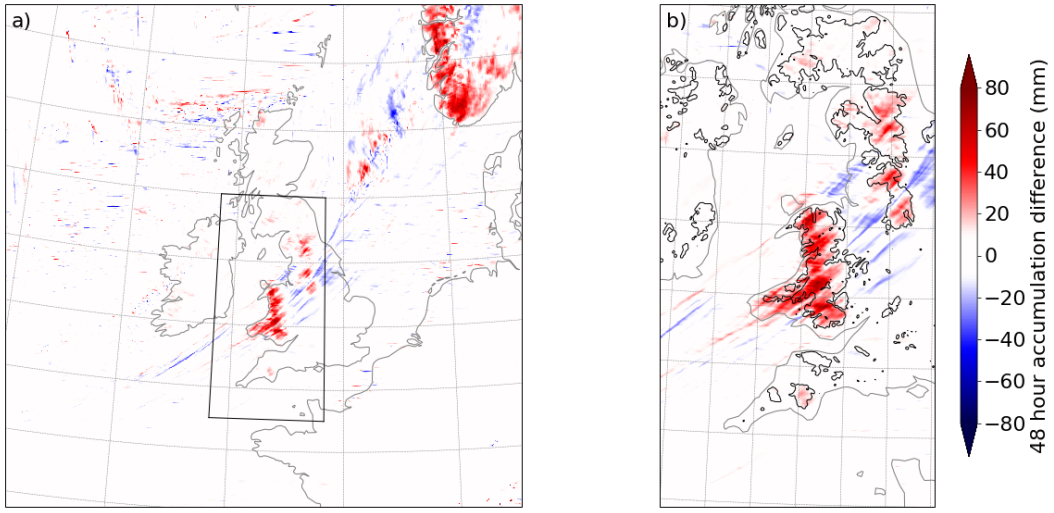

Figure 4.7: (a) The accumulated rainfall due to orographic enhancement over a 48 hour period in the UKA4g domain (17 °W to 9 °E and 46 °N to 61 °N) in (a) and in the domain outlined by the black box (17.6 °W to 9.74 °E and 44.5 °N to 62.2 °N) in (b). The black contour in (b) marks a surface height of 200 m.

When investigating the intensity of each storm, shown in Figure 4.5b, the largest difference in intensity is between the FLAT experiment and the CTRL experiment (approximately 5 hPa at 42 hours since 0000 UTC 20 September). As the largest difference is approximately 0.5 % (using 5 hPa and the FLAT experiment which is approx. 964 hPa at this time), the changes are not deemed important. Therefore, the

changes to the microphysics and the height of the orography does not significantly change the intensity of the storm.

To confirm that only the mechanisms are changed and not the overall dynamics of the storm, the accumulated rainfall over a 48 hour period over the whole domain is calculated for six experiments (CTRL, FLAT, NOACC2, NOACC2.5, NOACC3 and NOACC4). It is found that the difference in the accumulated rainfall between any two experiments is no more than 2.2 %.

4.2.3 Limiting accretion and riming in low-level orographic cloud

To ascertain the height of the low-level orographic cloud, and to choose suitable altitudes to turn off accretion and riming, the vertical distribution of ice and liquid water are examined where there is the enhancement of rainfall over elevated orography. These parameters are used to examine the position of the clouds as they describe the mean liquid water and mean ice content per grid-box (per kg of moist air). A cross section through Wales is taken at a constant latitude of 52.4 °N from 5 °W to 2 °E as this coincides with the enhanced rainfall shown in Figure 4.7b. The position of the cross section is shown in Figure 4.8a by the black line.

To highlight any low-level orographic cloud, the vertical distribution of ice and liquid water content produced by orographic enhancement is analysed. The ice and liquid water content is accumulated over a 48 hour period in the FLAT experiment and is subtracted from the ice and liquid water content accumulated over a 48 hour period produced by the CTRL experiment. Therefore, any positive values represent the cloud produced by orographic ascent and any negative values indicate where the liquid water content and ice water content is higher in the FLAT experiment than in the CTRL. The positive values are related to the cloud produced by orographic enhancement only as accretion and riming do not produce cloud droplets. This is shown in Figure 4.8b. To make a comparison to the height of any cyclone cloud,

the vertical distribution of ice and liquid water content produced by the cyclone is found using equation 4.4 and is shown in Figure 4.8c.

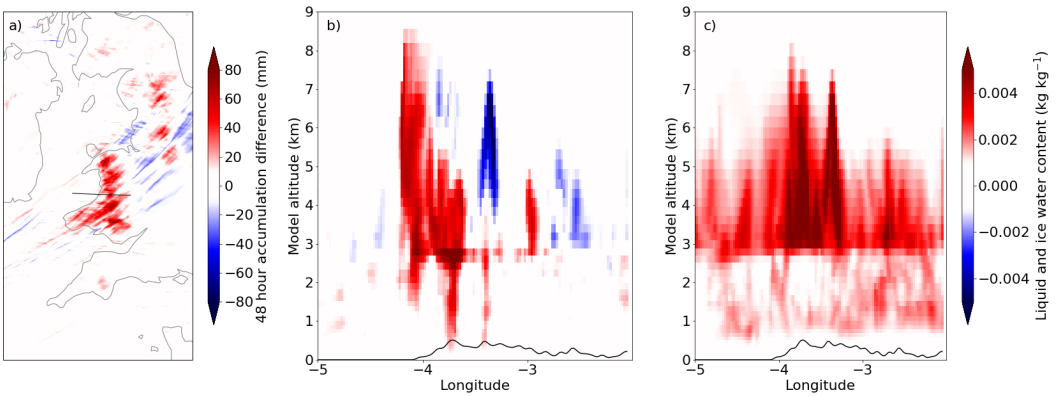

Figure 4.8: (a) The accumulated rainfall over a 48 hour period due to orographic enhancement shown over Wales and England, and the vertical distribution of the accumulated ice and liquid water content, q, over a 48 hour period due to (b) orographic enhancement and (c) cyclone-related ascent. This cross section is taken at the same location as in (b). The y-axis in b) and (c) represents the altitude above the local surface and the local surface (orography) is shown by the black line at the bottom of this Figure.

It can be seen above Wales (4.5 °W to 3.5 °W) in Figure 4.8b that there is an orographic enhancement of liquid water and ice related to orographic cloud (greater than approximately 0.002 kg kg^{-1}) extending from 0 to approximately 8 km above the surface. However, this overlaps with cloud produced by the cyclone, as shown in Figure 4.8c, where there is liquid water and ice extending from 1 to approximately 8 km above the surface in the same location. Therefore, it is difficult to separate the orographic cloud formed via orographic ascent and the cloud formed via the cyclone. This means that, particularly where the accretion and riming schemes are turned off at a higher altitude, the accretion and riming will be limited in cyclone cloud, as well as orographic cloud. Therefore, the contributions of low-level accretion and riming, including the seeder-feeder mechanism, are investigated rather than just

the seeder-feeder mechanism alone. As the cyclone related liquid water and ice are predominantly above approximately 3 km, the accretion and riming schemes are switched off below 1 km, 2 km, 2.5 km, 3 km and 4 km. This will mean that only a small portion of the cyclone related cloud will have accretion and riming switched off. Both the accretion and riming schemes are switched off, rather than just the accretion scheme, as there is riming below 4 km (found by plotting accretion and riming rates using the CTRL experiment).

4.3 Accumulated rainfall over Wales

To quantify how much each mechanism contributes to the overall precipitation, this study focuses on Wales, where the surface height is greater than 200 m (outlined in Figure 4.7b by the black contour over Wales). This is for two reasons, the first being that there is an enhancement of rainfall here as shown in Figure 4.7, and the second, is that it is on the west coast. Therefore, the rainfall produced via orographic ascent before reaching Wales is minimised because the storm tracks over the North Atlantic south of Ireland. This is shown in Figure 4.5a by the track of the storm in the CTRL, FLAT and NOACC3 experiments.

The 48 hour accumulated rainfall formed via each mechanism is shown in Figure 4.9. The contribution from all three mechanisms is shown in Figure 4.9a, from cyclone ascent in 4.9b, from orographic ascent in 4.9c and from low-level accretion and riming below 2 km where the surface height is greater than 200 m in 4.9d. The 48 hour accumulated rainfall is labelled 48 hour accumulated rainfall difference in this Figure as it the 48 hour accumulated rainfall in 4.9c and 4.9d are calculated by subtracting the rainfall produced by one experiment from another (using equations 4.5 and 4.6. The black contour represents a surface height of 200 m. The positive values in this Figure represent the contribution from each mechanism to the total precipitation. The negative values in Figure 4.9c) represent areas where there is

more accumulated rainfall in the FLAT experiment than the NOACC2 experiment. The negative values in Figure 4.9d, particularly the band of negative values along the right hand side of the the 200 m surface height contour over Wales, are produced when moist air passes into the region where the accretion and riming schemes are switched off (where the surface height is no longer greater than 200 m). When these schemes are switched off, there is more moisture available to produce rainfall downstream of orography which otherwise would have been converted to precipitation via accretion and riming. This moisture is not present in the CTRL experiment as the accretion and riming schemes are not modified. These negative values could therefore, be related to a rain shadow. This is because all the moisture available is converted to rainfall as it ascends over orography.

As shown in Figure 4.9a, where the surface height is greater than 200 m over Wales, there is an area of enhanced rainfall of over 80 mm over a 48 hour period. The accumulated rainfall produced by the cyclone is shown in Figure 4.9b where the accumulated rainfall reaches approximately 50 mm over the elevated area of Wales. As shown by Figure 4.9c, the contribution from orographic ascent to this precipitation is smaller, with values reaching a maximum of approximately 25 mm over some parts of the elevated orography. However, around the edges of the 200 m surface height contour, there are positive values reaching 50 mm. This suggests that the 200 m surface height might be too high to fully capture the contributions from low-level accretion and riming. However, it is concluded that the biggest enhancer of the rainfall produced by the cyclone is from low-level accretion and riming, as shown in Figure 4.9d, where the rainfall over Wales reaches approximately 50 mm in the region where the surface height is greater than 200 m.

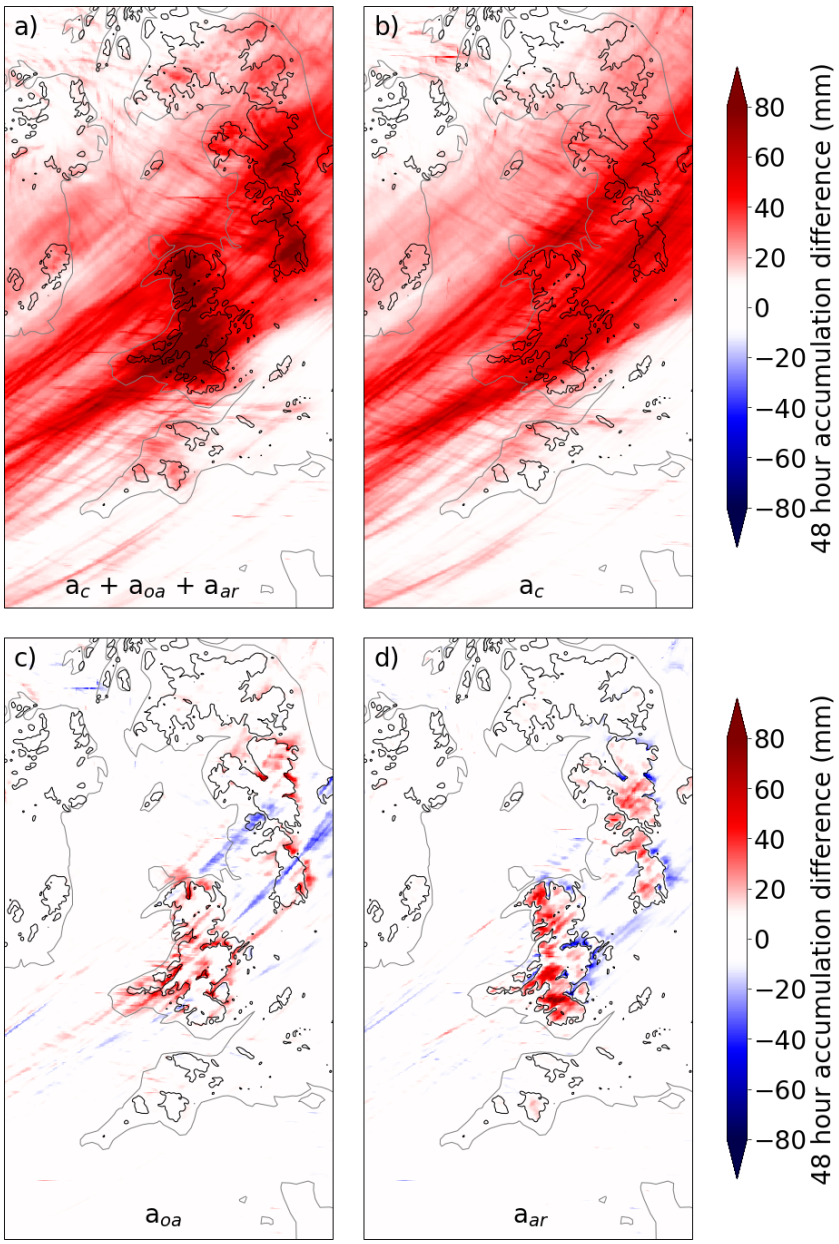

Figure 4.9: The accumulated rainfall over a 48 hour period (0000 UTC 20 September 2018 to 0000 UTC 22 September 2018) from (a) cyclone ascent, orographic ascent and accretion and riming (a_c, a_{oa} and a_{ar}) produced by the CTRL experiment, (b) cyclone ascent (a_c) produced by the FLAT experiment, (c) from orographic ascent (a_{oa}, calculated using the NOACC2 experiment and equation 4.5) and (d) from low-level accretion and riming (a_{ar}, calculated using the NOACC2 experiment and equation 4.6). The black contour represents a surface height of 200 m.

4.4 Contribution from cyclone ascent and orographic enhancement to the overall precipitation over Wales

To quantify how much each mechanism contributes to the overall precipitation, the accumulated rainfall is calculated over a 43 hour period where the surface height is greater than 200 m in Wales. A rectangular region (63 x 108 km) of the hourly accumulated rainfall over Wales (centered at (52.4 ° N, 3.7 ° W)) is taken. Subsequently, any data points that coincide with a surface elevation greater than 200 m within this rectangle are added. This process is repeated from 0500 UTC on 20 September 2018 until 0000 UTC on 22 September 2018 in hourly increments. By using any data points that lie within the 200 m contour, the results will not be influenced by any rainfall produced downstream of the orography. A 43 hour period starting at 0500 UTC on 20 September 2018 rather than a 48 hour one starting at 0000 UTC on 20 September 2018 was chosen to limit the contribution of precipitation produced along a frontal wave which is situated over the UK from 0000 UTC to 0500 UTC on the 20 September 2018.

The results are shown in Figure 4.10a for the CTRL and FLAT experiments. As shown in this Figure for both experiments, the accumulated rainfall increases rapidly from 0500 UTC until approximately 1800 UTC on 20 September coinciding with the storm tracking over Wales. This includes the rainfall produced by the warm front before the cyclone reached the UK (Figure 4.3). The accumulated rainfall then increases at a slower rate which coincides with the storm moving across the UK into the North Sea. Finally, at approximately 42 hours after 0000 UTC (1800 UTC 21 September) the accumulated rainfall plateaus as the storm passes into Scandinavia. Even though the accumulated rainfall follows the same trend for each experiment, the values themselves differ. The CTRL experiment produces more rainfall than the FLAT experiment at each time-step as all three processes are present in the CTRL

experiment whereas only the rainfall produced by the cyclone contributes to the precipitation in the FLAT experiment.

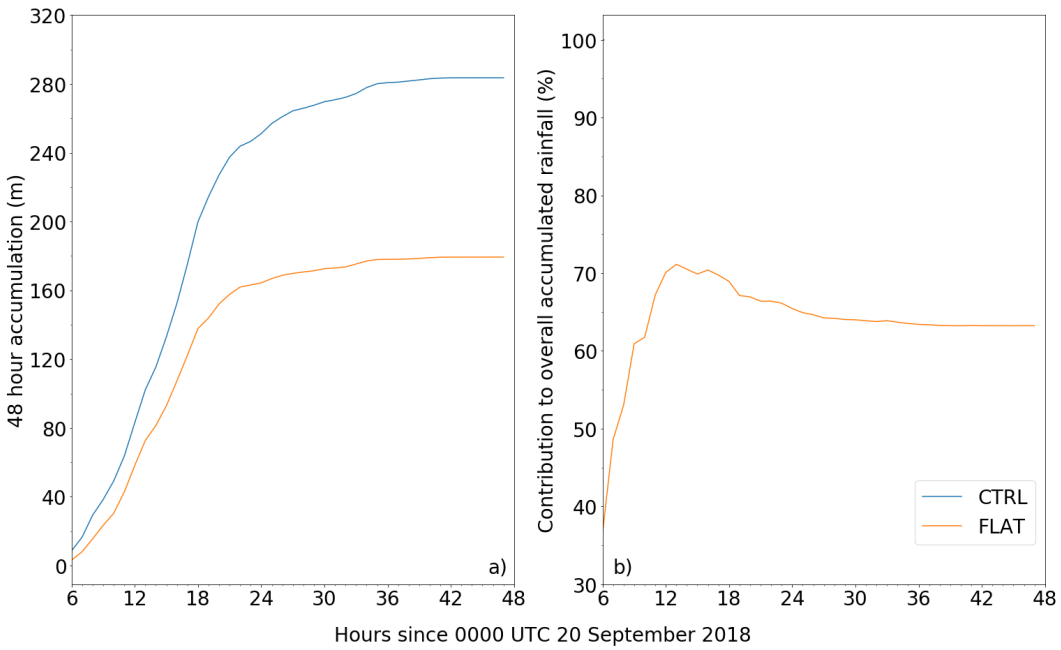

Figure 4.10: (a) The accumulated rainfall over time where there is elevated orography in Wales (any regions that have a surface height above 200 m in a 63 x 108 km rectangle centred at (52.4 ° N, 3.7 ° W)) from 0500 UTC 20 September 2018 to 0000 UTC 22 September 2018 calculated using the CTRL experiment and the FLAT experiment (b) The percentage contribution of the FLAT experiment to the overall precipitation over time. The overall precipitation is found using the CTRL experiment.

To quantify the contribution of each mechanism to the overall precipitation, the 43 hour accumulated rainfall from 0500 UTC 20 September to 0000 UTC 22 September produced by the FLAT experiment is converted to a percentage of the CTRL experiment. The CTRL experiment is used for the overall precipitation as all three processes are present and the results are shown in Figure 4.10b. The contribution from cyclone ascent increases from approximately 37 % to 66 % from 6 to 18 hours since 0000 UTC on 20 September. As the accumulated rainfall begins

to plateau, so does the percentage. At 48 hours since 0000 UTC on 20 September, the contribution from cyclone ascent is 63 %.

The conversion from the contribution to the overall precipitation by each experiment to the contribution from each mechanism is calculated following equations 4.4 and 4.7. This is done using the accumulated rainfall over a 43 hour period (from 0500 UTC 20 September to 0000 UTC 22 September) shown by the values on the right hand side of Figure 4.10b. It was found that 63 % of the rainfall associated with storm Bronagh was produced by cyclone ascent and 37 % produced via orographic enhancement. Therefore, the majority of the rainfall associated with the storm is produced by cyclone ascent (including convective processes).

4.5 Contribution from orographic ascent, accretion and riming to the overall precipitation over Wales

To ascertain what proportion of the orographically enhanced rainfall is due to orographic ascent and low-level accretion and riming (including the seeder-feeder mechanism), the accretion and riming schemes are switched off below 1, 2, 2.5, 3 and 4 km where the surface height is greater than 200 m. The percentage of the CTRL for each experiment is calculated using the same method described in the previous section and results are shown in Figure 4.11. In this Figure, the accumulated rainfall follows the same evolution in each experiment as the storm travels over the UK. However, the higher the altitude at which the accretion and riming schemes are switched off, the lower the accumulated rainfall that is produced in each NOACC experiment. This is because the higher the altitude, the more the droplet growth is limited in the cloud.

How much rainfall is produced by each mechanism is calculated using equations 4.4, 4.5 and 4.6 for each NOACC experiment with accretion and riming switched

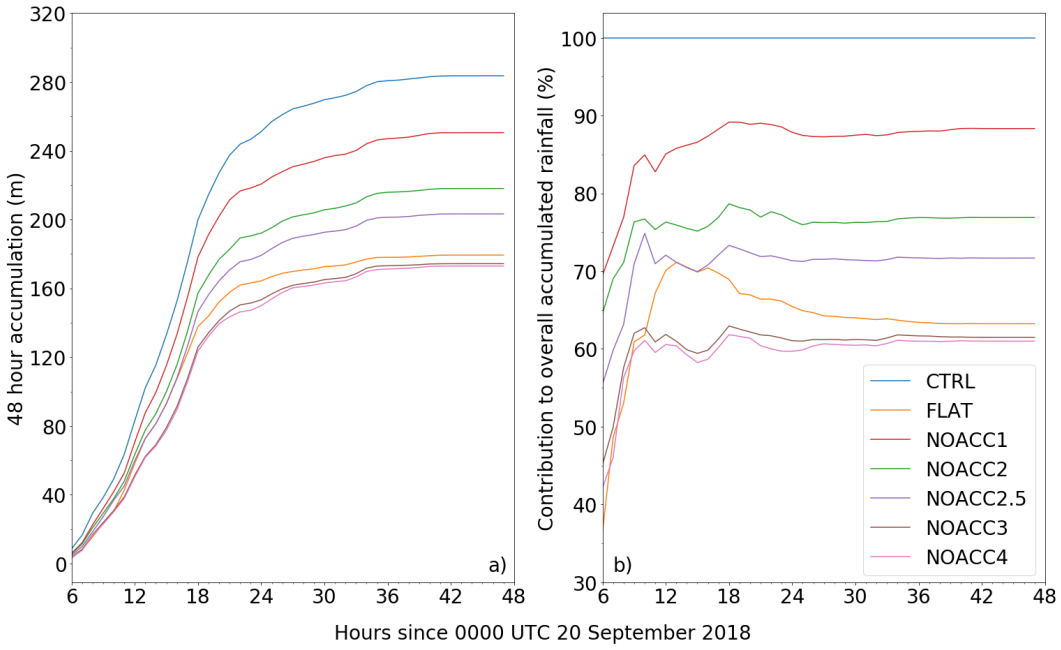

Figure 4.11: (a) The accumulated rainfall over time. (b) the percentage contribution of each experiment to the overall precipitation over time. These are calculated where there is elevated orography in Wales (any regions that have a surface height above 200 m in a 63 x 108 km rectangle centred at (52.4 ° N, 3.7 ° W) from 0500 UTC 20 September 2018 to 0000 UTC 22 September 2018 using the CTRL, FLAT, NOACC1, NOACC2, NOACC2.5, NOACC3 and NOACC4 experiments. The overall precipitation is found using the CTRL experiment.

off below different altitudes. The results are shown in Figure 4.12. In Figure 4.12a, the percentage that each mechanism contributes to the overall precipitation from 0500 UTC 20 September 2018 to 0000 UTC 22 September 2018 is shown. The colour of each line refers to each mechanism and the line-style represents the altitude at which the accretion and riming schemes are switched off. For example, the red dashed line labelled a_{oa1} refers to the rainfall produced via orographic ascent when the accretion and riming schemes are switched off at an altitude of 1 km. The shaded area shows how varying the altitude affects the percentage of the precipitation produced for each mechanism.

From 6 to approximately 24 hours after 0000 UTC on 20 September, the contribution from the overall precipitation changes for each mechanism. For cyclone ascent, the percentage of the total starts at approximately 36 % and increases to approximately 70 % 12 hours after 0000 UTC on 20 September. It then gradually decreases until it reaches a value of 63 % 48 hours after 0000 UTC on 20 September. This is shown in Figure 4.12b by the blue dot. This trend is reflected for the orographic enhancement, where the inverse is true. The percentage of the total starts at approximately 64 %, decreases to approximately 30 % 12 hours after 0000 UTC on 20 September. 48 hours after 0000 UTC on 20 September, 37 % of the overall rainfall is produced by orographic enhancement, as shown by the orange dot in Figure 4.12b. Therefore, the biggest contributor to the overall precipitation is cyclone ascent.

When analysing what proportion of the orographically enhanced rainfall is due to orographic ascent, and low-level accretion and riming (including the seeder-feeder mechanism), it can be seen that generally, accretion and riming provides a larger contribution to the overall precipitation than orographic ascent. As shown in Figure 4.12a, accretion and riming have a larger contribution to the overall rainfall than orographic ascent when the accretion and riming schemes are switched off between 2 and 4 km. When the schemes are turned off at 1 km, orographic ascent has a larger contribution than accretion and riming.

It is interesting to note that switching accretion and riming schemes off at 3 and 4 km results in a negative contribution from orographic ascent. This suggests that the accretion and riming schemes are being switched off at too high of an altitude thereby limiting the formation of rainfall in both the orographic and cyclone cloud. In this case, less rainfall is produced in the NOACC experiments than in the FLAT experiment. Therefore, when calculating the contribution from orographic ascent to the overall rainfall using equation 4.5, the result will be negative. This could

be related to the height of the cyclone related cloud as the majority of the cyclone cloud is above 3 km (see Figure 4.8).

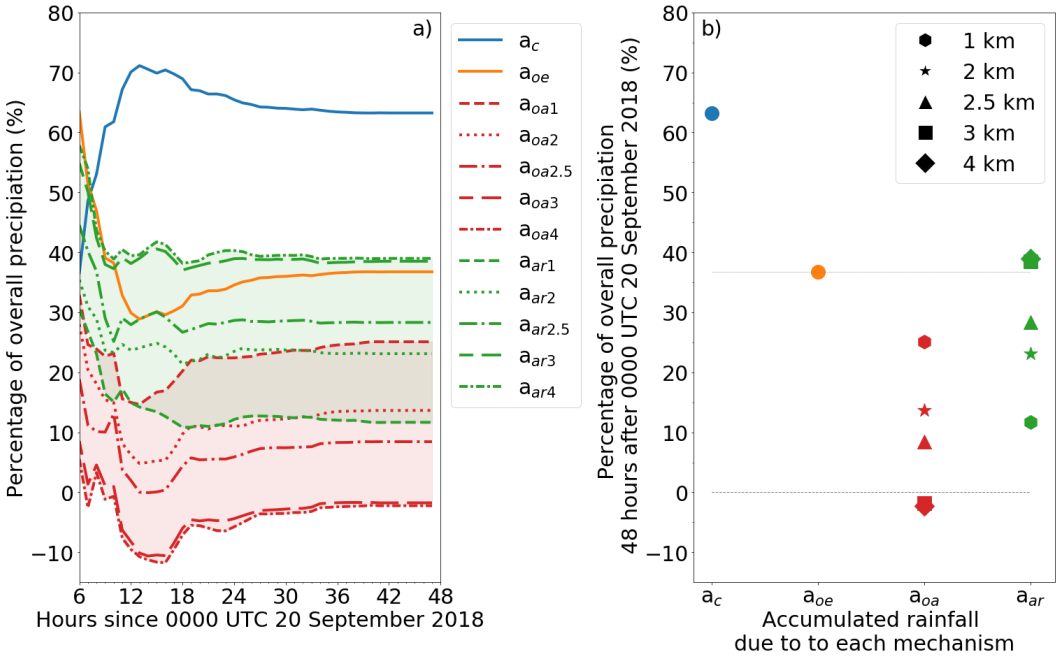

Figure 4.12: (a) The percentage of overall rainfall produced by each mechanism from 0500 UTC 20 September 2018 to 0000 UTC 22 September 2018. The colour of each line refers to each mechanism and the line-style represents the altitude at which the accretion and riming schemes are switched off. The shaded area shows the range of values obtained from varying the altitude that accretion and riming is switched off at. (b) Shows the percentage of overall rainfall produced by each mechanism 48 hours after 0000 UTC 20 September 2018. The colour of each marker matches the equivalent mechanism in (a) and the altitude that the accretion and riming schemes are switched off at are denoted by the marker shape. The grey dashed lines are located at zero and at 37 % depict the range that the percentage of rainfall for orographic ascent and accretion and riming should lie.

4.6 Conclusions

Through analysis of heavy precipitation associated with the case study storm Bronagh, it is found that 63 % of the rainfall associated with storm Bronagh was produced by cyclone ascent and 37 % produced via orographic enhancement. The 37 % produced by orographic enhancement can be split into two attributing factors, the precipitation formed via orographic ascent and the precipitation formed via accretion and riming (i.e. the seeder-feeder mechanism). By analysing the orographic enhancement further, it is found that generally, accretion and riming provides a larger contribution to the overall precipitation than orographic ascent. This suggests that when an extratropical cyclone and atmospheric river encounter orography in the UK, the majority of the heavy precipitation is produced by the cyclone and the rest is formed via accretion and riming (i.e. the seeder feeder mechanism). This could mean that the low-level moisture (for example, an atmospheric river) could play an important role in the enhancement of cyclone rainfall. These findings further support the link between land-falling atmospheric rivers, extratropical cyclones and production of heavy orographic precipitation.

Whilst these are interesting findings, it is useful to note that the work in this thesis is limited to a single case study. Therefore, further research is needed to understand whether this is always the case in the UK and and whether the contributions change in regions where there is much larger orography (in terms of height and width), for example, the Rockies. Furthermore, this study is carried out using a singular microphysics scheme and using a singular resolution. Therefore more studies are needed to ascertain the dependence of the results on the microphysics scheme and the resolution used.

CHAPTER

FIVE

CONCLUSIONS AND DISCUSSION

Extratropical cyclones and atmospheric rivers are linked to flooding (e.g. Hawcroft et al. (2012) and Lavers et al. (2011)). However, the direction of moisture transport, to the base of an extratropical cyclone's warm conveyor belt (where it rises to form precipitation) is unclear as both of these features are analysed in different frame-works (cyclone-relative or Earth-relative). Both extratropical cyclones and atmospheric rivers have been linked to precipitation extremes (e.g Pfahl and Wernli (2012) and Lavers et al. (2011)). Land-falling atmospheric rivers specifically have been shown to produce heavy rainfall along the west coast of the US over mountainous regions (e.g. Ralph et al. (2004)). However, the link between the synoptic scale flows and the micro-scale mechanisms that lead to precipitation is often not discussed in the literature. In the UK, where the hills are smaller in width than those in the US, it is unlikely that the forced ascent of moist air in an atmospheric river over orography (orographic ascent) will lead to heavy precipitation (Dore et al., 1992). It is more likely that heavy precipitation is formed via the interaction of cyclone related precipitation and the orographic ascent of moist air in an atmospheric river. The interaction occurs via the seeder-feeder mechanism and leads to the orographic enhancement of cyclone rainfall (Bader and Roach, 1977).

An atmospheric river is formed as a result of moisture flux convergence ahead of a cold front that is propagating through the atmosphere (Dacre et al., 2015). A cyclone-relative flow called the feeder airstream is responsible for supplying moisture to the base of the warm conveyor belt and for enhancing the poleward transport of moisture (Dacre et al., 2019). This rearward travelling feeder airstream transports moisture from the environment into which a cyclone is propagating towards the centre of the cyclone. The airstream splits into two branches ahead of the cyclones cold front. One branch turns anticyclonically to run parallel to the cold front and accelerates towards the base of the warm conveyor belt (active region). The other branch turns cyclonically to run parallel to the cold front and decelerates relative to the cyclone propagation (passive region). This moisture is therefore, left behind by the cyclone as it propagates, and marks the track of the cyclone. As the cyclone and cold front tend to move polewards as they propagate, the moisture that is left behind by the cyclone is still transported polewards, but at a slower rate than the cyclone.

It is hypothesised that the feeder airstream is present in cyclones that are propagating faster than the moisture flux in the atmospheric river, resulting in the transport of moisture to the base of the warm conveyor belt from ahead of the cyclone. Cyclones propagate faster during their intensification stage and more intense cyclones may propagate faster than weak ones (Owen et al., 2021; Hoskins and Hodges, 2002). To understand the direction of moisture transport to the base of a warm conveyor belt and to understand the link between synoptic scale flows and micro-scale mechanisms in the production of heavy orographic rainfall, three research objectives are addressed in this thesis.

1. Can the feeder airstream be objectively identified using an identification algorithm in a case study, storm Bronagh?

2. Which midlatitude northern hemisphere cyclones are more likely to a feeder

airstream and thus transport moisture to the warm conveyor belt from the environment the cyclone is propagating into? Does the likely-hood of a feeder airstream occurring depend on the intensity, propagation velocity or the life-cyclone stage of the cyclone?

3. What proportion of the rainfall associated with the aforementioned case study is produced by the cyclone, the forced ascent of air over orography or via the seeder-feeder mechanism when the case study passes over the UK?

To investigate whether the intensity, the propagation velocity or the stage of the cyclones life-cycle determines whether moisture is transported from the environment ahead of the cyclone centre to the base of the warm conveyor belt, the presence of a feeder airstream is investigated using a case study (storm Bronagh) and in northern hemisphere extratropical cyclones. Furthermore, to link synoptic scale mechanisms such as the feeder airstream and atmospheric rivers to the micro-scale mechanisms that lead to precipitation in the UK, storm Bronagh is analysed using the MetUM. By modifying the height of the orography, and accretion and riming in the model, the portion of the rainfall produced in the UK can be attributed to cyclone ascent, orographic ascent or the seeder-feeder mechanism. It is hypothesised that the seeder-feeder mechanism will contribute to a larger portion of the precipitation than orographic ascent as this has been shown to be important for the production of rainfall in the UK (Lean and Browning, 2013).

This thesis advances the understanding of the direction of moisture transport within extratropical cyclones and atmospheric rivers as the feeder airstream is investigated in northern hemisphere extratropical cyclones, not just in intense North Atlantic cyclones (as done in Dacre et al. (2019) and Papritz et al. (2021)). The understanding of the direction of moisture transport is further advanced in this thesis as the link between moisture transport and a cyclone's intensity, propagation velocity and life-cycle is also investigated. This has not been done in previous studies.

Additionally, the understanding of the link between the synoptic scale and micro-scale mechanisms in the production of orographic precipitation in the UK has also been advanced. This is because this thesis investigates a case study where the passage of an atmospheric river and extratropical cyclone over the UK led to flooding. This has also not been done in previous studies.

5.1 The presence of the feeder airstream in extratropical cyclones

The case study, storm Bronagh tracked eastwards across the North Atlantic, the UK, the North Sea, Scandinavia and the Norwegian Sea in late September 2018. The storm is centered over the UK at 0000 UTC 21 September 2018 and led to flooding in Wales and England. This storm reached its maximum intensity of 8.97×10^{-5} s^{-1} (relative vorticity) on 1800 UTC on 22 September 2018 over the Norwegian Sea, meaning that the storm passed over the UK while in its developing stage. An atmospheric river associated with storm Bronagh is identified ahead of the cyclone's cold front in the warm sector, using a threshold value in IVT of 250 kg m^{-1} s^{-1}. This atmospheric river is present throughout the evolution of the storm. This supports the work of Dacre et al. (2015).

The identification algorithm, developed using storm Bronagh, identifies regions associated with saddle points in the cyclone-relative moisture flux field (cyclone-relative winds multiplied by specific humidity). The saddle points are created by the feeder airstream and the dry intrusion splitting into two branches at the cold front. If a saddle point is located in the low-level moisture flux, and coincides with an area of negative determinant, then a feeder airstream is present. This suggests that moisture is transported to the warm conveyor belt from the environment ahead of the cyclone. A region associated feeder airstream is identified during the developing stages of the

storm (from 1200 UTC 20 September to 1500 UTC 21 September) indicating that moisture is transported from ahead of the cyclone to the base of the warm conveyor belt during this time. Therefore, a feeder airstream can be objectively identified using an identification algorithm in a case study, storm Bronagh.

The region associated with the feeder airstream lies ahead of the cold front within the atmospheric river, demonstrating that the feeder airstream partitions an atmospheric river into two regions, one which accelerates towards the base of the warm conveyor belt, supporting the work of Dacre et al. (2019). It is also supported by the work of Xu et al. (2022) who found that warm conveyor belt inflow is typically characterized by strong moisture flux convergence and a band of high water vapour transport that supplies moisture to the base of the warm conveyor belt. It is found that the feeder airstream is only present when the propagation velocity of the cyclone is greater than 11.8 m s^{-1}.

To investigate the direction of moisture transport and the relationship to the intensity of the storm, propagation velocity, and to further investigate the relationship to the evolution of the storm, 1000 storms are randomly sampled from the extended winter period in the extratropical northern hemisphere from 1979 - 2019. These storms are then organised into data-sets depending on their maximum intensity or propagation velocity. Four data-sets are created with intense to weak storm tracks (labelled I_1, I_2, I_3 and I_4 with I_1 containing the strongest storms) and four are created with fast to slowly propagating cyclones (labelled U_1, U_2, U_3 and U_4 with U_1 containing the fastest storms). Composite data is created for storms at 24 hours prior to maximum intensity (T-24), at maximum intensity (T+0) and 24 hours post maximum intensity (T+24) using the data-sets with storm tracks ordered by intensity. Composite data is also created for the storm time-steps which are ordered by propagation velocity.

It is found that all composite storms have a feeder airstream regardless of their

intensity, propagation velocity or time relative to maximum intensity. The composite feeder airstream coincides with the warm sector of the cyclones (as shown by the composite specific humidity data and composite isobars) and moves as the cold front and warm sector of the cyclone move. Furthermore, the minimum associated with the saddle point created by the composite feeder airstream either coincides with, or lies to the south west, of the centroid of the composite atmospheric river at T-24, T+0 and T+24 for I_1 and for I_2 at T-24 and T+0. This suggests that the atmospheric river is partitioned into active and passive regions by the feeder airstream and that the feeder airstream enhances the poleward transport of moisture via the atmospheric rivers. These results, and the findings using the case study, supports the work of Dacre et al. (2015, 2019) and is consistent with the work of Houze et al. (1976), Hoskins and West (1979), Carlson (1980) and Mcbean and Stewart (1991) who found that the warm conveyor belt originates to the east of the cyclone centre and by the work of Boutle et al. (2011) who found that moisture is transported to the base of the warm conveyor belt from ahead of the cyclone using an idealised model.

Even though the composite data shows that all cyclones have a feeder airstream, it is also found that the strength of the moisture flux related to the feeder airstream decreases as the intensity and propagation velocity of the storms decrease. Furthermore, it also decreases as the cyclones reach maximum intensity and begin to decay. This is supported by the fact that atmospheric rivers are only present in the composite I_1 data at T-24, T+0 and T+24, the composite I_2 data at T-24, T+0 and the composite U_1 data. However, because composite data is formed as a result of taking an average over all the storms in the data-set, it is unclear how likely a feeder airstream is to occur in the domain and whether the strength of the moisture flux associated with the feeder airstream (and IVT in atmospheric rivers) decreases because the cold fronts in each storm are not co-located. This would mean that

the high filaments of IVT in the atmospheric rivers and the moisture fluxes relating to the feeder airstream are also not co-located which could lower the composite IVT and moisture flux. To ascertain the likelihood of a feeder airstream saddle point occurring relative to the background, the identification algorithm is applied to each storm in each data-set. Using the results, the probability density of saddle points and background probability density of saddle points are used to calculate the likelihood ratio. This is the likelihood of a feeder airstream saddle point occurring relative to the background.

It is found that a feeder airstream saddle point is more likely to occur than background in all I data-sets at all times relative to maximum intensity and for all U data-sets. This region coincides with the feeder airstreams found in the composite data supporting these findings. A feeder airstream saddle point is most likely to occur (30 times more likely than background, found using the maximum likelihood in the domain) south of the cyclone centre in more intense storms (storms in the I_1 data-set) during the developing stage (at T-24). A feeder airstream saddle point is also more likely to occur (21 times more likely than background, found using the maximum likelihood in the domain) in the fastest moving storms (in the U_1 data-set) in comparison to slower moving ones. The fact that the maximum likelihood in the domain is higher for the most intense storms rather than the fastest storms suggests that the intensity of the cyclone has more of an effect on the presence of the feeder airstream than the propagation velocity.

The higher maximum likelihood of a feeder airstream occurring in fast moving, developing, intense storms would support the findings of the case study as storm Bronagh would fall into both the I_1 and U_1 data-sets. This is because storm Bronagh had a maximum intensity of 8.97×10^{-5} s^{-1} and a feeder airstream is only identified when the storm is moving quicker than 11.8 m s^{-1} (which occurs during the intensification phase). The fact that it is more likely that a feeder airstream

will occur in intense developing storms would also support the work of Papritz et al. (2021) who found that a north easterly flow transported moisture to the warm sector of a cyclone. However, whilst the maximum likelihood in the domain suggests that the likelihood of the feeder airstream saddle point occurring decreases with intensity, propagation velocity and in the later stages of a cyclone's life-cycle (at maximum and during decay), the area where the likelihood greater than 1 covers in the domain suggests that this might not be the case. This is because this area increases with a decrease in intensity, propagation velocity and the later the life-cycle (at maximum and during decay) of the cyclone, suggesting that the feeder airstreams saddle points become less aligned. Therefore, it is difficult to draw conclusions about the likelihood of a feeder airstream saddle point occurring, and the strength of the moisture flux associated with the feeder airstream in relation to the intensity, propagation velocity and life-cycle of a cyclone.

Future work could involve rotating the cyclones before taking a 20 $^{\circ}$ cut out around the cyclone centre. This would mean that features such as the cold fronts are more likely to align at all stages of the cyclone's evolution making it easier to draw conclusions from the composite data and from the likelihood of a feeder airstream saddle point occurring in the domain in relation to the background. Similarly, the propagation velocity of the cold front could be used to calculate the cold frontal-relative flows rather than the cyclone-relative flows. This would mean that the feeder airstreams would be more aligned as they lie ahead of the cold front (Dacre et al., 2019). Using these methods, the identification algorithm could also be used to investigate the movement of the feeder airstream saddle point relative to the cold fronts.

5.2 The contribution of synoptic scale and micro-scale mechanisms to the production of rainfall in the UK

To ascertain how much of the rainfall produced by storm Bronagh can be attributed to cyclone ascent, orographic ascent and the seeder-feeder mechanism, modifications to the height of the orography, and the accretion and riming micro-physical processes are made in the MetUM. The orography in the domain is flattened to remove any rainfall produced via the orographic enhancement of rainfall (orographic ascent, the seeder-feeder mechanism and convection). To remove any rainfall produced by the seeder-feeder mechanism, the accretion and riming microphysics schemes are switched off below 1, 2, 2.5, 3 and 4 km above the surface where the height of the surface (above mean sea level) is greater than 200 m. The schemes are only switched off over the surface height of 200 m as this is where the low-level orographic cloud is located. The height that the schemes are switched off at varied because it is difficult to separate the orographic cloud from the cyclone cloud.

The accumulated rainfall over a 43 hour period where the surface height is greater than 200 m in Wales produced by the MetUM after each modification is calculated and compared to the accumulated rainfall over a 43 hour period produced by the control simulation. By doing so, a percentage contribution of each mechanism to the control is found. It is found that 63 % of the precipitation is produced via cyclone ascent and 37 % is produced by the orographic enhancement of the rainfall produced via cyclone ascent. When looking at the contributions of orographic ascent and the seeder-feeder to the orographically enhanced rainfall, it is found that generally accretion and riming (related to the seeder-feeder mechanism) have a larger contribution to the orographic rainfall than orographic ascent. This suggests that heavy precipitation in the UK is formed by cyclone related precipitation falling through low-level cloud formed via the forced ascent of air in an atmospheric river (which is

associated with the feeder airstream). The findings of Kropač et al. (2021) support these conclusions as they found that large amounts of rain fell during the passage of an atmospheric river and cold front over the Southern Alps of New Zealand as a result of the seeder-feeder mechanism. It also supports the findings of Browning et al. (1974) and Lean and Browning (2013) who found that in the UK, orographic ascent of low-level moist air can lead to the enhancement of precipitation falling from preexisting storms via the seeder-feeder mechanism.

Future work could involve varying the height and width of the orography to ascertain whether this has any affect on the contribution from orographic ascent. It is hypothesised that if the height and width of the orography increases, the contribution from orographic ascent will also increase. Furthermore, the availability of low-level moisture at the base of the hills could be modified to see whether this has an effect on the contribution from the seeder-feeder mechanism or the orographic ascent of air. This is because the degree of rainfall enhancement within the feeder cloud depends on the strength of the low-level winds, the humidity and temperature of the low-level air and the intensity of precipitation falling from the seeder cloud (Hill et al., 1981; Smith et al., 2010; Lean and Browning, 2013). It is hypothesised that the larger the moisture availability at the base of the hill, the larger the enhancement of rainfall via the seeder-feeder mechanism.

5.3 Concluding remarks

The investigations carried out in this thesis have highlighted the importance of understanding the moisture transport associated with extratropical cyclones and atmospheric rivers. Particularly when an atmospheric river and extratropical cyclone encounters orography in the UK. By understanding this moisture transport, the resulting impacts of heavy precipitation can be further understood. This is particularly important as the intensity of rainfall associated with extratropical cyclones

and the intensity of atmospheric river events are expected to increase as the climate changes and there is an increase in atmospheric moisture (Allan et al., 2020).

Whilst the investigations conducted in this thesis advance the understanding of the direction of moisture transport in atmospheric rivers and extratropical cyclones, there are still numerous unanswered questions that have arisen from the investigations. For example, what determines how much of the moisture within the feeder airstream propagates into the active region and how much is left as a snail trail in the passive region? Is this effected by the orientation of the feeder airstream respective to the cold front, the propagation and orientation of the cold front respective to the cyclone centre, the cyclone propagation velocity and, or, other factors? How do these factors effect the intensity of the atmospheric river? Are there cases where no moisture is left as a snail trail in the passive region? Are there cases where the feeder airstream is far from a cyclone centre? If so, how do these cases effect the formation of subsequent cyclones and atmospheric rivers and the resulting impacts? How does the location of the feeder airstream within an atmospheric river relate to centroids in TCWV and IVT? Does this have any implications for atmospheric river detection? These numerous questions highlight the exciting possibilities for future research into atmospheric rivers and extratropical cyclones.

BIBLIOGRAPHY

Adusumilli, S., Borsa, A. A., Fish, M. A., McMillan, H. K. and Silverii, F. (2019) A Decade of Water Storage Changes Across the Contiguous United States From GPS and Satellite Gravity. *Geophysical Research Letters*, **46**, 13006–13015.

Allan, R. P., Barlow, M., Byrne, M. P., Cherchi, A., Douville, H., Fowler, H. J., Gan, T. Y., Pendergrass, A. G., Rosenfeld, D., Swann, A. L. S., Wilcox, L. J. and Zolina, O. (2020) Advances in understanding large-scale responses of the water cycle to climate change. *Annals of the New York Academy of Sciences*, **1472**, 49–75.

Allan, R. P., Lavers, D. A. and Champion, A. J. (2016) Diagnosing links between atmospheric moisture and extreme daily precipitation over the UK. *International Journal of Climatology*, **36**, 3191–3206.

Allan, R. P. and Soden, B. J. (2008) Atmospheric warming and the amplification of precipitation extremes. *Science*, **321**, 1481–1484.

AMS (2023a) Atmospheric river. *American Meteorology Society, Glossary of Meteorology.*

— (2023b) Low-level jet. *American Meteorology Society, Glossary of Meteorology.*

— (2023c) Rain shadow. *American Meteorology Society, Glossary of Meteorology.*

Bader, M. J. and Roach, W. T. (1977) Orographic rainfall in warm sectors of depressions. *Quarterly Journal of the Royal Meteorological Society*, **103**, 269–280.

Bjerknes, J. (1919) On the structure of moving cyclones. *Monthly Weather Review*, **47**, 95–99.

Boutle, I. A., Belcher, S. E. and Plant, R. S. (2011) Moisture transport in midlatitude cyclones. *Quarterly Journal of the Royal Meteorological Society*, **137**, 360–373.

Browning, K. (1971) Radar measurements of air motion near fronts. *Weather*, **26**, 320–340.

Browning, K. and Harrold, T. (1970) Air motion and precipitation growth at a cold front. *Quarterly Journal of the Royal Meteorological Society*, **96**, 369–389.

Browning, K. A., Hill, F. F. and Pardoe, C. W. (1974) Structure and mechanism of precipitation and the effect of orography in a wintertime warm sector. *Quarterly Journal of the Royal Meteorological Society*, **100**, 309–330.

Browning, K. A. and Mason, J. S. (1980) Air motion and precipitation growth in frontal systems. *pure and applied geophysics*, **119**, 577–593.

Browning, K. A. and Roberts, N. M. (1994) Structure of a frontal cyclone. *Quarterly Journal of the Royal Meteorological Society*, **120**, 1535–1557.

Carlson, T. N. (1980) Airflow Through Midlatitude Cyclones and the Comma Cloud Pattern. *Monthly Weather Review*, **108**, 1498–1509.

Champion, A. J., Allan, R. P. and Lavers, D. A. (2015) Atmospheric rivers do not explain UK summer extreme rainfall. *Journal of Geophysical Research: Atmospheres*, **120**, 6731–6741.

Collins English Dictionary (2005) Definition of saddle point. [Cited 14 March 2022. Most material © 2005, 1997, 1991 by Penguin Random House LLC. Modified

entries © 2019 by Penguin Random House LLC and HarperCollins Publishers Ltd. Word origin [1920–25]].

Collow, A. B. M., Shields, C. A., Guan, B., Kim, S., Lora, J. M., McClenny, E. E., Nardi, K., Payne, A., Reid, K., Shearer, E. J., Tomé, R., Wille, J. D., Ramos, A. M., Gorodetskaya, I. V., Leung, L. R., O'Brien, T. A., Ralph, F. M., Rutz, J., Ullrich, P. A. and Wehner, M. (2022) An Overview of ARTMIP's Tier 2 Reanalysis Intercomparison: Uncertainty in the Detection of Atmospheric Rivers and Their Associated Precipitation. *Journal of Geophysical Research: Atmospheres*, **127**.

Cuckow, S., Dacre, H. F. and Martínez-Alvarado, O. (2022) Moisture transport contributing to precipitation at the centre of storm Bronagh. *Weather*, **77**, 196–201.

Dacre, H. F., Clark, P. A., Martinez-Alvarado, O., Stringer, M. A. and Lavers, D. A. (2015) How Do Atmospheric Rivers Form? *Bulletin of the American Meteorological Society*, **96**, 1243–1255.

Dacre, H. F., Martínez-Alvarado, O. and Mbengue, C. O. (2019) Linking Atmospheric Rivers and Warm Conveyor Belt Airflows. *Journal of Hydrometeorology*, **20**, 1183–1196.

Dore, A. J., Choularton, T. W., Brown, R. and Blackall, R. M. (1992) Orographic rainfall enhancement in the mountains of the Lake District and Snowdonia. *Atmospheric Environment. Part A. General Topics*, **26**, 357–371.

Drazin, P. G. (1992) *Nonlinear Systems*. Cambridge Texts in Applied Mathematics. Cambridge University Press.

Gentile, E., Barlow, J., Edwards, J., Lewis, H. and Gray, S. (2021a) The Impact of Atmosphere-Ocean-Wave Coupling on the Near-Surface Wind Speed in Forecasts of Extratropical Cyclones. *Boundary-Layer Meteorology*, **180**.

Gentile, E. S., Gray, S. L., Barlow, J. F., Lewis, H. W. and Edwards, J. M. (2021b) The impact of atmosphere–ocean–wave coupling on the near-surface wind speed in forecasts of extratropical cyclones. *Bound.-Lay. Meteorol.*, **180**, 105–129.

Gimeno, L., Nieto, R., Vázquez, M. and Lavers, D. A. (2014) Atmospheric rivers: A mini-review. *Frontiers in Earth Science*, **2**, 2.

Gimeno-Sotelo, L. and Gimeno, L. (2023) Where does the link between atmospheric moisture transport and extreme precipitation matter? *Weather and Climate Extremes*, **39**, 100536.

Guan, B. and Waliser, D. E. (2015) Detection of atmospheric rivers: Evaluation and application of an algorithm for global studies. *Journal of Geophysical Research: Atmospheres*, **120**, 12514–12535.

— (2019) Tracking atmospheric rivers globally: Spatial distributions and temporal evolution of life cycle characteristics. *Journal of Geophysical Research: Atmospheres*, **124**, 12523–12552.

Guan, B., Waliser, D. E. and Ralph, F. M. (2023) Global Application of the Atmospheric River Scale. *Journal of Geophysical Research: Atmospheres*, **128**, e2022JD037180.

Guo, Y., Shinoda, T., Guan, B., Waliser, D. E. and Chang, E. K. M. (2020) Statistical Relationship between Atmospheric Rivers and Extratropical Cyclones and Anticyclones. *Journal of Climate*, **33**, 7817–7834.

Hart, N. C., Gray, S. L. and Clark, P. A. (2015) Detection of coherent airstreams using cluster analysis: Application to an extratropical cyclone. *Monthly Weather Review*, **143**, 3518–3531.

Hawcroft, M. K., Shaffrey, L. C., Hodges, K. I. and Dacre, H. F. (2012) How much

Northern Hemisphere precipitation is associated with extratropical cyclones? *Geophysical Research Letters*, **39**.

Hersbach, H., Bell, B., Berrisford, P., Hirahara, S., Horányi, A., Muñoz-Sabater, J., Nicolas, J., Peubey, C., Radu, R., Schepers, D., Simmons, A., Soci, C., Abdalla, S., Abellan, X., Balsamo, G., Bechtold, P., Biavati, G., Bidlot, J., Bonavita, M., De Chiara, G., Dahlgren, P., Dee, D., Diamantakis, M., Dragani, R., Flemming, J., Forbes, R., Fuentes, M., Geer, A., Haimberger, L., Healy, S., Hogan, R. J., Hólm, E., Janisková, M., Keeley, S., Laloyaux, P., Lopez, P., Lupu, C., Radnoti, G., de Rosnay, P., Rozum, I., Vamborg, F., Villaume, S. and Thépaut, J.-N. (2020) The ERA5 global reanalysis. *Quarterly Journal of the Royal Meteorological Society*, **146**, 1999–2049.

Hill, F. F., Browning, K. A. and Bader, M. J. (1981) Radar and raingauge observations of orographic rain over south wales. *Quarterly Journal of the Royal Meteorological Society*, **107**, 643–670.

Hodges, K. I. (1994) A general method for tracking analysis and its application to meteorological data. *Monthly Weather Review*, **122**, 2573 – 2586.

— (1995) Feature Tracking on the Unit Sphere. *Monthly Weather Review*, **123**, 3458–3465.

— (1999) Adaptive constraints for feature tracking. *Monthly Weather Review*, **127**, 1362 – 1373.

Hoskins, B. J. and Hodges, K. I. (2002) New Perspectives on the Northern Hemisphere Winter Storm Tracks. *Journal of the Atmospheric Sciences*, **59**, 1041–1061.

Hoskins, B. J. and West, N. V. (1979) Baroclinic Waves and Frontogenesis. Part II: Uniform Potential Vorticity Jet Flows-Cold and Warm Fronts. *Journal of Atmospheric Sciences*, **36**, 1663–1680.

Houze, R. A., Locatelli, J. D. and Hobbs, P. V. (1976) Dynamics and Cloud Microphysies of the Rainbands in an Occluded Frontal System. *Journal of Atmospheric Sciences*, **33**, 1921–1936.

Kingston, D. G., Lavers, D. A. and Hannah, D. M. (2016) Floods in the Southern Alps of New Zealand: the importance of atmospheric rivers. *Hydrological Processes*, **30**, 5063–5070.

Kropač, E., Mölg, T., Cullen, N. J., Collier, E., Pickler, C. and Turton, J. V. (2021) A Detailed, Multi-Scale Assessment of an Atmospheric River Event and Its Impact on Extreme Glacier Melt in the Southern Alps of New Zealand. *Journal of Geophysical Research: Atmospheres*, **126**.

Lamjiri, M. A., Dettinger, M. D., Ralph, F. M. and Guan, B. (2017) Hourly storm characteristics along the U.S. West Coast: Role of atmospheric rivers in extreme precipitation. *Geophysical Research Letters*, **44**, 7020–7028.

Lavers, D. A., Allan, R. P., Villarini, G., Lloyd-Hughes, B., Brayshaw, D. J. and Wade, A. J. (2013) Future changes in atmospheric rivers and their implications for winter flooding in britain. *Environmental Research Letters, Volume 8, Number 3*.

Lavers, D. A., Allan, R. P., Wood, E. F., Villarini, G., Brayshaw, D. J. and Wade, A. J. (2011) Winter floods in Britain are connected to atmospheric rivers. *Geophysical Research Letters*, **38**, 1–8.

Lavers, D. A., Villarini, G., Allan, R. P., Wood, E. F. and Wade, A. J. (2012) The detection of atmospheric rivers in atmospheric reanalyses and their links to British winter floods and the large-scale climatic circulation. *Journal of Geophysical Research: Atmospheres*, **117**.

Lean, H. W. and Browning, K. A. (2013) Quantification of the importance of wind

drift to the surface distribution of orographic rain on the occasion of the extreme Cockermouth flood in Cumbria. *Quarterly Journal of the Royal Meteorological Society*, **139**, 1342–1353.

Lewis, H., Sanchez, J., Arnold, A., Fallmann, J., Saulter, A., Graham, J., Bush, M., Siddorn, J., Palmer, T., Lock, A., Edwards, J., Bricheno, L., la Torre, A. and Clark, J. (2019) The UKC3 regional coupled environmental prediction system. *Geoscientific Model Development*, **12**, 2357–2400.

Little, K., Kingston, D. G., Cullen, N. J. and Gibson, P. B. (2019) The Role of Atmospheric Rivers for Extreme Ablation and Snowfall Events in the Southern Alps of New Zealand. *Geophysical Research Letters*, **46**, 2761–2771.

Ludwig, P., Pinto, J. G., Reyers, M. and Gray, S. L. (2014) The role of anomalous SST and surface fluxes over the southeastern North Atlantic in the explosive development of windstorm Xynthia. *Quarterly Journal of the Royal Meteorological Society*, **140**, 1729–1741.

Madonna, E., Wernli, H., Joos, H. and Martius, O. (2014) Warm Conveyor Belts in the ERA-Interim Dataset (1979–2010). Part I: Climatology and Potential Vorticity Evolution. *Journal of Climate*, **27**, 3–26.

Martínez-Alvarado, O., Joos, H., Chagnon, J., Boettcher, M., Gray, S. L., Plant, R. S., Methven, J. and Wernli, H. (2014) The dichotomous structure of the warm conveyor belt. *Quarterly Journal of the Royal Meteorological Society*, **140**, 1809–1824.

Mattingly, K. S., Mote, T. L. and Fettweis, X. (2018) Atmospheric River Impacts on Greenland Ice Sheet Surface Mass Balance. *Journal of Geophysical Research: Atmospheres*, **123**, 8538–8560.

Mcbean, G. A. and Stewart, R. E. (1991) Structure of a Frontal System over the Northeast Pacific Ocean. *Monthly Weather Review*, **119**, 997–1013.

Met Office (2018) Strong winds and heavy rain from storms ali and bronagh. URL: `https://www.metoffice.gov.uk/binaries/content/assets/metofficegovuk/pdf/weather/learn-about/uk-past-events/interesting/2018/strong-winds-and-heavy-rain-from-storms-ali-and-bronagh---met-office.pdf`. [Accessed 25 November 2021].

Michel, C., Sorteberg, A., Eckhardt, S., Weijenborg, C., Stohl, A. and Cassiani, M. (2021) Characterization of the atmospheric environment during extreme precipitation events associated with atmospheric rivers in Norway - Seasonal and regional aspects. *Weather and Climate Extremes*, **34**, 100370.

Moore, B. J., Neiman, P. J., Ralph, F. M. and Barthold, F. E. (2012) Physical Processes Associated with Heavy Flooding Rainfall in Nashville, Tennessee, and Vicinity during 1–2 May 2010: The Role of an Atmospheric River and Mesoscale Convective Systems. *Monthly Weather Review*, **140**, 358–378.

Najman, L. and Schmitt, M. (1994) Watershed of a continuous function. *Mathematical Morphology and its Applications to Signal Processing*, **38**, 99–112.

Neiman, P., Schick, L., Ralph, F., Hughes, M. and Wick, G. (2011) Flooding in western washington: The connection to atmospheric rivers. *Journal of Hydrometeorology*, **12**, 1337–1358.

Neu, U., Akperov, M. G., Bellenbaum, N., Benestad, R., Blender, R., Caballero, R., Cocozza, A., Dacre, H. F., Feng, Y., Fraedrich, K., Grieger, J., Gulev, S., Hanley, J., Hewson, T., Inatsu, M., Keay, K., Kew, S. F., Kindem, I., Leckebusch, G. C., Liberato, M. L. R., Lionello, P., Mokhov, I. I., Pinto, J. G., Raible, C. C., Reale,

M., Rudeva, I., Schuster, M., Simmonds, I., Sinclair, M., Sprenger, M., Tilinina, N. D., Trigo, I. F., Ulbrich, S., Ulbrich, U., Wang, X. L. and Wernli, H. (2013) Imilast: A community effort to intercompare extratropical cyclone detection and tracking algorithms:. *Bulletin of the American Meteorological Society*, **94**, 529 – 547.

Newell, R. E., Newell, N. E., Zhu, Y. and Scott, C. (1992) Tropospheric rivers?–A pilot study. *Geophysical Research Letters*, **19**, 2401–2404.

NOAA (2023) URL: `https://www.nnvl.noaa.gov/view/#TRUE`.

Nugent, A., DeCou, D., Russell, S. and Karamperidou, C. (2019) *Atmospheric Processes and Phenomena*. ATMO 200: Atmospheric Processes and Phenomenon course at the University of Hawai'i at Mānoa.

Oltmanns, M. et al. (2019) Interactive comment on "increased greenland melt triggered by large-scale, year-round precipitation events" by marilena oltmanns et al.

Owen, L. E., Catto, J. L., Stephenson, D. B. and Dunstone, N. J. (2021) Compound precipitation and wind extremes over Europe and their relationship to extratropical cyclones. *Weather and Climate Extremes*, **33**, 100342.

Palmén, E. (1931) Die Beziehung zwischen troposphärischen und stratosphärischen Temperatur- und Luftdruckschwankungen.

Papritz, L., Aemisegger, F. and Wernli, H. (2021) Sources and transport pathways of precipitating waters in cold-season deep north atlantic cyclones. *J. Atmos. Sci.*, **78**, 3349–3368.

Pérez-Muñuzuri, V., Eiras-Barca, J. and Garaboa-Paz, D. (2018) Tagging moisture sources with Lagrangian and inertial tracers: application to intense atmospheric river events. *Earth System Dynamics*, **9**, 785–795.

Pfahl, S., Madonna, E., Boettcher, M., Joos, H. and Wernli, H. (2014) Warm Conveyor Belts in the ERA-Interim Dataset (1979–2010). Part II: Moisture Origin and Relevance for Precipitation. *Journal of Climate*, **27**, 27–40.

Pfahl, S. and Wernli, H. (2012) Quantifying the relevance of cyclones for precipitation extremes. *Journal of Climate*, **25**, 6770–6780.

Ralph, F. M. and Dettinger, M. D. (2011) Storms, floods, and the science of atmospheric rivers. *Eos, Transactions American Geophysical Union*, **92**, 265–266.

Ralph, F. M., Dettinger, M. D., Cairns, M. M., Galarneau, T. J. and Eylander, J. (2018) Defining "atmospheric river": How the Glossary of Meteorology helped resolve a debate. *Bulletin of the American Meteorological Society*, **99**, 837–839.

Ralph, F. M., Iacobellis, S. F., Neiman, P. J., Cordeira, J. M., Spackman, J. R., Waliser, D. E., Wick, G. A., White, A. B. and Fairall, C. (2017) Dropsonde Observations of Total Integrated Water Vapor Transport within North Pacific Atmospheric Rivers. *Journal of Hydrometeorology*, **18**, 2577–2596.

Ralph, F. M., Neiman, P. J. and Wick, G. A. (2004) Satellite and CALJET Aircraft Observations of Atmospheric Rivers over the Eastern North Pacific Ocean during the Winter of 1997/98. *Monthly Weather Review*, **132**, 1721–1745.

Ralph, F. M., Neiman, P. J., Wick, G. A., Gutman, S. I., Dettinger, M. D., Cayan, D. R. and White, A. B. (2006) Flooding on California's Russian River: Role of atmospheric rivers. *Geophysical Research Letters*, **33**, 3–7.

Ramos, A. M., Trigo, R. M., Liberato, M. L. R. and Tomé, R. (2015) Daily Precipitation Extreme Events in the Iberian Peninsula and Its Association with Atmospheric Rivers. *Journal of Hydrometeorology*, **16**, 579–597.

Reed, R. J., Stoelinga, M. T. and Kuo, Y.-H. (1992) A Model-aided Study of the Origin and Evolution of the Anomalously High Potential vorticity in the Inner

Region of a Rapidly Deepening Marine Cyclone. *Monthly Weather Review*, **120**, 893–913.

Reid, K. J., King, A. D., Lane, T. P. and Hudson, D. (2022) Tropical, Subtropical, and Extratropical Atmospheric Rivers in the Australian Region. *Journal of Climate*, **35**, 2697–2708.

Reid, K. J., King, A. D., Lane, T. P. and Short, E. (2020) The sensitivity of atmospheric river identification to integrated water vapor transport threshold, resolution, and regridding method. *Journal of Geophysical Research: Atmospheres*, **125**.

Reid, K. J., Rosier, S. M., Harrington, L. J., King, A. D. and Lane, T. P. (2021) Extreme rainfall in New Zealand and its association with Atmospheric Rivers. *Environmental Research Letters*, **16**, 44012.

Rutz, J. J., James Steenburgh, W. and Martin Ralph, F. (2014) Climatological characteristics of atmospheric rivers and their inland penetration over the western united states. *Monthly Weather Review*, **142**, 905–921.

Rutz, J. J., Shields, C. A., Lora, J. M., Payne, A. E., Guan, B., Ullrich, P., O'Brien, T., Leung, L. R., Ralph, F. M., Wehner, M., Brands, S., Collow, A., Goldenson, N., Gorodetskaya, I., Griffith, H., Kashinath, K., Kawzenuk, B., Krishnan, H., Kurlin, V., Lavers, D., Magnusdottir, G., Mahoney, K., McClenny, E., Muszynski, G., Nguyen, P. D., Prabhat, M., Qian, Y., Ramos, A. M., Sarangi, C., Sellars, S., Shulgina, T., Tome, R., Waliser, D., Walton, D., Wick, G., Wilson, A. M. and Viale, M. (2019) The Atmospheric River Tracking Method Intercomparison Project (ARTMIP): Quantifying Uncertainties in Atmospheric River Climatology. *Journal of Geophysical Research: Atmospheres*, **124**, 13777–13802.

Schultz, D. and Vaughan, G. (2011) Occluded Fronts and the Occlusion Process:

A Fresh Look at Conventional Wisdom. *Bulletin of the American Meteorological Society*, **92**.

Shapiro, M. A. and Keyser, D. (1990) *Fronts, Jet Streams and the Tropopause*, 167–191. Boston, MA: American Meteorological Society.

Shields, C. A., Rutz, J. J., Leung, L.-Y., Ralph, F. M., Wehner, M., Kawzenuk, B., Lora, J. M., McClenny, E., Osborne, T., Payne, A. E. et al. (2018) Atmospheric river tracking method intercomparison project (ARTMIP): project goals and experimental design. *Geosci. Model Dev.*, **11**, 2455–2474.

Smith, B., Yuter, S., Neiman, P. and Kingsmill, D. (2010) Water vapor fluxes and orographic precipitation over northern california associated with a landfalling atmospheric river. *Monthly Weather Review*, **138**, 74–100.

Smith, R. B. (1979) The influence of mountains on the atmosphere. vol. 21 of *Advances in Geophysics*, 87–230. Elsevier.

Smith, S., Vosper, S. and Field, P. (2015) Sensitivity of orographic precipitation enhancement to horizontal resolution in the operational Met Office Weather forecasts. *Meteorological Applications*, **22**, 14–24.

Sodemann, H. and Stohl, A. (2013) Moisture Origin and Meridional Transport in Atmospheric Rivers and Their Association with Multiple Cyclones. *Monthly Weather Review*, **141**, 2850–2868.

Sodemann, H., Wernli, H., Knippertz, P., Cordeira, J. M., Dominguez, F., Guan, B., Hu, H., Ralph, F. M. and Stohl, A. (2020) *Structure, process, and mechanism*, 15–43. Springer.

Valiente, N. G., Saulter, A., Edwards, J. M., Lewis, H. W., Castillo Sanchez, J. M., Bruciaferri, D., Bunney, C. and Siddorn, J. (2021) The Impact of Wave Model Source Terms and Coupling Strategies to Rapidly Developing Waves across the

North-West European Shelf during Extreme Events. *Journal of Marine Science and Engineering*, **9**.

Walker, E., Mitchell, D. and Seviour, W. (2020) The numerous approaches to tracking extratropical cyclones and the challenges they present. *Weather*, **75**, 336–341.

Wang, S., Ma, X., Xu, G., Zhou, S., Chang, P. and Wu, L. (2022) A Comparison between the Kuroshio Extension and Pineapple Express Atmospheric Rivers Affecting the West Coast of North America. *Journal of Climate*, **35**, 3905–3925.

Wernli, H. (1997) A lagrangian-based analysis of extratropical cyclones. II: A detailed case-study. *Quarterly Journal of the Royal Meteorological Society*, **123**, 1677–1706.

Wernli, H. and Davies, H. (1997) A lagrangian-based analysis of extratropical cyclones. i: The method and some applications. *Quarterly Journal of the Royal Meteorological Society*, **123**, 467 – 489.

Wille, J. D., Alexander, S. P., Amory, C., Baiman, R., Barthélemy, L., Bergstrom, D. M., Berne, A., Binder, H., Blanchet, J., Bozkurt, D., Bracegirdle, T. J., Casado, M., Choi, T., Clem, K. R., Codron, F., Datta, R., Battista, S. D., Favier, V., Francis, D., Fraser, A. D., Fourré, E., Garreaud, R. D., Genthon, C., Gorodetskaya, I. V., González-Herrero, S., Heinrich, V. J., Hubert, G., Joos, H., Kim, S.-J., King, J. C., Kittel, C., Landais, A., Lazzara, M., Leonard, G. H., Lieser, J. L., Maclennan, M., Mikolajczyk, D., Neff, P., Ollivier, I., Picard, G., Pohl, B., Ralph, F. M., Rowe, P., Schlosser, E., Shields, C. A., Smith, I. J., Sprenger, M., Trusel, L., Udy, D., Vance, T., Vignon, É., Walker, C., Wever, N. and Zou, X. (2024) The Extraordinary March 2022 East Antarctica "Heat" Wave. Part I: Observations and Meteorological Drivers. *Journal of Climate*, **37**, 757–778.

Wilson, D. R. and Ballard, S. P. (1999) A microphysically based precipitation scheme

for the UK meteorological office unified model. *Quarterly Journal of the Royal Meteorological Society*, **125**, 1607–1636.

Xu, G., Wang, L., Chang, P., Ma, X. and Wang, S. (2022) Improving the Understanding of Atmospheric River Water Vapor Transport Using a Three-Dimensional Straightened Composite Analysis. *Journal of Geophysical Research: Atmospheres*, **127**.

Young, M. V., Monk, G. A. and Browning, K. A. (1987) Interpretation of Satellite Imagery of A Rapidly Deepening Cyclone. *Quarterly Journal of the Royal Meteorological Society*, **113**, 1089–1115.

Zhu, Y. and Newell, R. E. (1994) Atmospheric rivers and bombs. *Geophysical Research Letters*, **21**, 1999–2002.

I acknowledge use of the Monsoon2 system, a collaborative facility supplied under the Joint Weather and Climate Research Programme, a strategic partnership between the Met Office and the Natural Environment Research Council.